



DISSERTATION

**Ballistic quantum transport
at high energies and high magnetic fields**

ausgeführt zum Zwecke der Erlangung des akademischen Grades
eines Doktors der technischen Wissenschaften

unter der Leitung von
O.Univ.-Prof. Dipl.-Phys. Dr. Joachim Burgdörfer
Institut für Theoretische Physik (136)

eingereicht an der Technischen Universität Wien
Fakultät für Technische Naturwissenschaften und Informatik

von
Dipl.-Ing. Stefan Rotter
Matrikelnummer: 9325482
Emil-Kralikg. 4/50
1050 Wien

Wien 21.1.04

Ort, Datum

Stefan Rotter

Unterschrift

*To the musicians of the TU orchestra,
without whom my time as a Ph.D. student
might have been somewhat shorter,
but certainly not as enjoyable as it was.*

Ballistischer Quantentransport bei hohen Energien und starken Magnetfeldern

Abstract in German - Deutsche Kurzfassung

Der Elektronentransport durch zweidimensionale ballistische Mikrostrukturen zeigt Quantenphänomene, die durch die Phasenkohärenz dieses Streuproblems bedingt sind. Es ist mittlerweile technisch machbar, Halbleiterstrukturen zu fertigen, deren Größe kleiner ist als die mittlere freie Weglänge. Dies ermöglicht das experimentelle Studium des Elektronentransports durch Leitfähigkeitsmessungen. Von besonderem Interesse ist dabei der Bereich von hoher Elektronenenergie und hohem Magnetfeld, das senkrecht auf die Ebene der Mikrostruktur angebracht wird. Der Übergang zu hohen Energien spielt in der Quantenmechanik deswegen eine ganz besondere Rolle, da man in diesem Fall eine Einmündung der Quantenphysik in die klassische Physik beobachten kann. Im Falle des hohen Magnetfelds ergeben sich bei kohärentem Transport eine Vielzahl von interessanten Phänomenen, wie z.B. der Quanten-Hall-Effekt.

Wie sich zeigt, stößt eine theoretische Beschreibung dieser Effekte mit konventionellen Methoden sehr bald an ihre Grenzen. Der Grund dafür ist der, dass diese Parameterbereiche bei den gängigen numerischen Verfahren zu schwer kontrollierbaren Instabilitäten führen oder eines nicht bewältigbaren Aufwandes an Rechenzeit bedürfen um Konvergenz zu erzielen. Es stellt daher eine große Herausforderung dar, verbesserte Methoden zu erarbeiten, die diese Probleme in den Griff bekommen und dadurch theoretische Vorhersagen in bisher nicht erreichbaren Gebieten des ballistischen Transports erlauben.

In dieser Arbeit wird ein Verfahren vorgestellt, das speziell für hohe Elektronenenergien und hohe Magnetfelder geeignet ist. Es handelt sich dabei um eine Erweiterung der *rekursiven Methode der Greenschen Funktionen*. In der bisherigen Form dieses numerischen Modells wird die Greensche Funktion (i.e. der Propagator) des Streuproblems durch rekursive Lösung eines Systems von gekoppelten "Gitterbändern" berechnet. In der vorliegenden Arbeit zeigen wir, dass die Effizienz dieser Herangehensweise massiv gesteigert wird, wenn man die Symmetrien der Streuge-

ometrie in die Berechnung der Greenschen Funktion miteinbezieht. Dies ist speziell dann möglich, wenn sich die Geometrie der zu berechnenden Mikrostruktur aus *separablen* Modulen zusammensetzen lässt. Diese "Gittermodule" können mit unserer Methode direkt berechnet werden und müssen nicht - so wie bisher - in eine Vielzahl von "Gitterbändern" zerlegt werden. Wir bezeichnen daher unser Verfahren als *modulare rekursive Methode der Greenschen Funktionen*.

Als erste Anwendung benutzen wir unser Verfahren zur Berechnung von Elektronentransport durch Strukturen mit regulärer bzw. chaotischer klassischer Dynamik. Wie wir durch Auswertung der Streuwellenfunktion und der Streumatrix zeigen können, ergeben sich - speziell für hohe Elektronenenergie - auch in der Quantenmechanik spezifische Unterschiede zwischen diesen beiden Klassen von Systemen. Im weiteren verwenden wir unsere Methode zur numerischen Berechnung von spezifischen Effekten in der ballistischen Transporttheorie. Dazu zählen in dieser Arbeit der Fano-Resonanzeffekt, Aharonov-Bohm-Oszillationen, der Quanten-Hall-Effekt, de Haas-van Alphen-Oszillationen, elektronisches Schrotrauschen und der Effekt der schwachen Lokalisierung. Unsere Berechnungen zum Fano-Resonanzeffekt führten auch zu einer experimentellen Realisierung an der Philipps-Universität in Marburg/Deutschland. Im Rahmen dieses Experiments konnten unsere Vorhersagen mit den an einem Mikrowellenbilliard gemessenen Daten verglichen werden. Dabei wurde eine erstaunlich genaue Übereinstimmung zwischen Theorie und Experiment erzielt, die unter anderem auf den Einbau von dissipativen Mechanismen in unsere Methode zurückzuführen ist.

Contents

1	Introduction	1
I	Method and first numerical results	5
2	Scattering theory	6
2.1	The standard recursive Green's function method	7
2.2	The modular recursive Green's function method	9
2.3	Non-Cartesian tight-binding grids	10
2.4	Inclusion of a magnetic field	12
2.5	Calculation of modules	14
2.5.1	Rectangular module	15
2.5.2	Circle and half-circle	16
2.5.3	Link module	18
2.5.4	Semi-infinite lead	21
2.6	Assembling all the modules	22
2.7	Transport coefficients	25
2.8	Scattering wave functions	28
2.9	Efficiency of the MRGM	28
3	Numerical results	30
3.1	Accuracy checks	30
3.2	Wavefunctions	31
II	Applications	35
4	Oscillations and resonances in transmission	36
4.1	Transport at high energies	36
4.2	Transport at high magnetic fields	38
4.3	Multi-channel interferences	41
4.4	Comparison with experiments	47
5	Fano resonances	49
5.1	Transport through a microwave cavity	49
5.2	Experiment and theory	51

6	Quantum Hall effect	59
6.1	The Hall voltage	60
6.2	Single edge state regime	62
6.3	Quantization in a Hall bar	64
6.4	Disorder potentials	65
7	De Haas-van Alphen oscillations	69
8	Shot noise	73
8.1	Shot noise suppression	74
8.2	Numerical results	77
8.3	Distribution of transmission eigenvalues	82
8.4	Tunable cavities	83
8.5	Future work	87
9	Weak localization	88
9.1	Numerical results and discussion	89
9.2	Future work	92
10	Summary	94
11	Outlook	96
	Bibliography	100
	Acknowledgements	108
	Curriculum vitae	109
	Publications	111

List of Acronyms

nD	n -dimensional
AB	Aharonov-Bohm
ABO	Aharonov-Bohm oscillation
a.u.	atomic units
dHvA	de Haas-van Alphen
MRGM	modular recursive Green's function method
RGM	recursive Green's function method
RMT	random matrix theory
WL	weak localization

Chapter 1

Introduction

Due to technical advances in semiconductor science, the fabrication of phase coherent scattering devices has recently become possible [1–5]. A major aim in ballistic transport theory is to simulate and stimulate experiments in this field with the help of accurate calculations. In spite of the conceptual simplicity of the problem, the numerical simulation of ballistic electron transport through quantum dots has remained a computational challenge. This is partly due to the fact, that many of the most interesting phenomena occur in a parameter regime of either high magnetic field B or high Fermi energy E_F . Under the influence of a high magnetic field, one can study the Quantum Hall effect [6], de Haas-van Alphen oscillations [7], the “Hofstadter butterfly” [8] and Aharonov-Bohm oscillations of transport coefficients [9]. In the high energy domain, it is mainly the transition from quantum to classical dynamics [10] and all related topics such as “quantum chaos” [11] and localization phenomena [12], on which particular interest is focused.

However interesting they may be, these parameter ranges are difficult to handle from a computational point of view. In the regime of high Fermi energy E_F the de Broglie-wavelength of the electrons, $\lambda_D = \sqrt{2E_F}$, is much smaller than the linear dimensions of the scattering device, $\lambda_D \ll D$. To properly describe the continuum limit of the transport process, a large number of basis functions is necessary. At some point, this requirement renders all the respective methods computationally unfeasible or numerically instable. The case of high magnetic fields is reached when the magnetic length, $l_B = \sqrt{c/B}$ (in a.u.), is considerably smaller than the system dimensions, $l_B \ll D$. Under these circumstances methods based on the expansion in plane or spherical waves become invalid since diamagnetic contributions are generally neglected [13]. Methods employing a discretization on a grid do not allow the flux per unit cell to exceed a certain maximum value and therefore suffer from the same computational unfeasibility as for high energies [14–16]. As a result, the theoretical models which are presently being employed reach their limits of applicability already below the semiclassical domain. It is therefore desirable to have a new approach at hand, which can bypass the limitations of conventional techniques. In this thesis we present such an approach and demonstrate that thereby very high energies and magnetic fields can be attained. The present work constitutes an extension of an idea previously introduced by Sols *et al.* [17] and consists of a modification

of the widely used *Recursive Green's Function Method* (RGM) [14–16, 18]. In the standard RGM the Green's function is propagated through the scattering region from one transverse strip to the next through repeated solutions of a matrix Dyson equation. We will show that the efficiency of this “conventional” discretization can be increased considerably by taking the symmetries of a scattering problem into account. Especially if the two-dimensional nonseparable open quantum dot can be built up out of simpler separable substructures (modules), one gains tremendously in computational speed by calculating the Green's functions for each of these modules individually. This idea is the essential ingredient of our method. It is put into practice by discretizing each individual module in a symmetry-adapted tight-binding grid which leads to a separability of the eigenfunctions and allows to appropriately incorporate the boundary conditions of the module. By this procedure also the Green's functions are set up faster than in the conventional way. As a consequence, it is possible to include a much higher number of grid points, which is the prerequisite for reaching shorter wavelengths and higher magnetic fields. We will demonstrate that, in order to take advantage of this approach, the condition of separability in the modules is not a strict one. Even if the geometry of a module can be “completed” or “folded” to a separable boundary, our method is applicable.

The efficiency of the MRGM is demonstrated by applying it to transport through a rectangular, circular and a stadium shaped quantum dot. These systems are known as prototype structures for regular and chaotic dynamics and have been studied thoroughly in the literature [1, 2, 10, 11]. Considerable attention has been dedicated to reach high energies [19–23] and high magnetic fields [22, 24–29]. Especially for the study of transport through open stadium billiards, several different methods have been employed [13, 21, 30–33]. In the following chapters we will present numerical results obtained by the MRGM which attain a parameter range, to our knowledge, not yet explored by other approaches. For small λ_D we investigate the localization of the scattering wavefunction near classical scattering trajectories. Characteristic differences in the dynamics of generically regular and chaotic systems will be highlighted. In the high-magnetic-field regime, which is governed by edge states, differences between the dynamics in different geometries gradually disappear.

The present thesis is divided into two parts. The first one is dedicated to the introduction of the MRGM and to a presentation of results on wavefunctions for the circle and stadium billiards. We further analyze the accuracy of the method. In the second part of the thesis the MRGM is applied to simulate specific ballistic quantum transport phenomena which have received much attention recently. Amongst these we will consider the *Aharonov-Bohm* [9] and the *Fano resonance effect* [34] in transport through mesoscopic systems, the *integer quantum Hall effect* [35], *de Haas-van Alphen oscillations* [36], the suppression of *shot noise* [37] and the *weak localization* effect [38] in transport through quantum dots. All of these phenomena have in common that for their numerical simulation a very efficient and accurate calculation scheme is required. Since with the MRGM we have such a tool at hand, we investigate these specific phenomena. As will be demonstrated, several new and partly unexpected findings could be uncovered. We will put them into the context of the present state of knowledge in the respective fields of research.

The first topic we address is the emergence of regular oscillations and isolated resonances in the transport coefficients of our scattering geometries. In the case of high magnetic fields we identify quasi-periodic Aharonov-Bohm oscillations which, at a critical magnetic field, break off and transport terminates entirely. In the regime where more than one edge state is excited in the dot, we find interference fluctuations which we analyze in terms of a multi-channel Fano interference model [39, 40]. The key to the understanding of the observed fluctuations is that inter-channel scattering between different edge states takes place only by diffractive scattering at the lead junctions.

To investigate Fano resonances experimentally we present a scattering set-up, meanwhile realized by Kuhl and Stöckmann in Marburg, Germany [41]. This device consists of a quasi two-dimensional (2D) metal cavity through which microwaves with variable frequency are transported. Due to the equivalence of the electromagnetic Helmholtz equation and the Schrödinger equation for the single free electron in two dimensions [11], these microwave experiments are formally equivalent to ballistic electron transport measurements. In such a way we manage to demonstrate experimentally the emergence of Fano resonances in ballistic transport through quantum dots. One of the specific features of our set-up is that individual resonances can be tuned and particular classes of resonances can be identified that display a distinct variation of their Fano parameter. Moreover, our experiment is the first quantum dot experiment we are aware of, in which the Fano lineshapes could be quantitatively accounted for by theory rather than just being fitted. To optimize the correspondence between the measured and the calculated data we further include a damping mechanism in the MRGM which accounts for the dissipated part of the microwave flux absorbed by the cavity walls.

In the field of the integer-quantum Hall effect, traces of the many-particle Hall quantization on a single-electron transport experiment are investigated. The high-field capability of the MRGM is essential for the performance of these calculations since only in the regime of high B -fields plateau values in the Hall voltage emerge [42]. We also consider the effect of de Haas-van Alphen oscillations which, in a closed quantum dot, are only observed under the condition that $l_B \lesssim D$.

Last, but not least, we focus our attention on the phenomenon of “shot noise” and the “weak localization effect”. The MRGM turns out to be very useful in this context since the evaluation of the transport coefficients at many different parameter values is required. This is because the predictions for both effects concern the average values of a statistical ensemble of data. Due to the efficiency of the MRGM we are capable of evaluating very large ensembles, which, in turn, allows for an excellent comparison between the predictions and the numerical results. In such a way we uncover that the sensitivity of shot noise to the regularity or chaoticity of the underlying classical dynamics involved in a transport process is much less pronounced than was expected [43, 44]. We also perform a numerical simulation of a recent experiment on shot noise [45], which was so far beyond the reach of standard numerical methods in ballistic transport theory [46]. In the context of the weak localization effect we verify the prediction that weak localization peaks in transport through circular billiards take on a triangular line shape. We further demonstrate that this line

shape turns into a Lorentzian form in case that a decohering mechanism suppresses the contributions from long electron trajectories.

Part I

Presentation of the method and first numerical results

Chapter 2

Scattering theory for ballistic microstructures

In this chapter we formulate the quantum scattering problem for conductance through microstructures. We assume inelastic scattering sources to be absent, for which reason the electron motion throughout the device region is ballistic. Inside the hard-wall boundary of the microstructure we assume a constant potential set to be equal zero in the following, while being infinitely high outside. Due to phase coherence the conductance through these devices is determined by the shape of the chosen confining potentials. Some of the boundary geometries considered here are depicted in Fig. 2.1. Note that these geometries represent prototype systems for regular and chaotic classical dynamics, respectively. Two semi-infinite waveguides of width d at different electrochemical potentials μ_L and μ_R are attached to the scattering geometries in different orientations. If not stated otherwise, the aperture of the leads is chosen to be very small, $d/D = d/\sqrt{A^{\text{dot}}} = 0.0935$, where $A^{\text{dot}} = 4 + \pi$ is the scaled area of the cavities studied and D is a characteristic linear dimension of the cavity. The energy at which the scattering process takes place is the Fermi energy $E_F = \hbar^2 k_F^2 / 2m_{\text{eff}}$. Furthermore a constant magnetic field B is assumed to be oriented perpendicular to the scattering plane.

In the asymptotic region, i.e. far away from the scattering domain, the electron propagates like in a perfect wave guide which we assume to be linear. The wave function can be factorized into a longitudinal, propagating part (plane wave motion) and a transverse part (standing wave). The latter is a simple sine wave in the field-free case and a combination of Kummer functions when the magnetic field is turned on [47, 48]. In our local coordinate system the longitudinal (transverse) direction in the i th lead is always denoted by x_i (y_i). The wavefunctions in the waveguides are thus always fixed to zero at $y_i = \pm d/2$. Atomic units ($\hbar = |e| = m_{\text{eff}} = 1$) will be used from now on, unless explicitly stated otherwise.

2.1 The standard recursive Green's function method

In order to highlight the technical difficulties in setting up the *modular* recursive Green's function technique (MRGM), we start by briefly reviewing the *standard* recursive Green's function method (RGM) for the case of zero magnetic field [14–16, 18]. This standard approach is widely used in various fields of computational physics and consists in a discretization of the scattering geometry on a Cartesian grid. Setting up a tight-binding (tb) Hamiltonian on this grid,

$$\hat{H}^{\text{tb}} = \sum_i \varepsilon_i |i\rangle\langle i| + \sum_{i,j} V_{i,j} |i\rangle\langle j|, \quad (2.1)$$

the hopping potentials $V_{i,j}$ and the site energies ε_i are chosen such that the Hamilton equation $\hat{H}^{\text{tb}}|\psi_m\rangle = E_m|\psi_m\rangle$ converges towards the continuum Schrödinger equation for many grid points,

$$-\frac{1}{2} \left(\frac{\partial^2}{\partial x^2} + \frac{\partial^2}{\partial y^2} \right) \psi_m = E_m \psi_m. \quad (2.2)$$

The hopping potentials are non-zero only for the nearest neighbour coupling of grid-points and result directly from a three point difference approximation of the kinetic energy term in the free-particle Hamiltonian (2.2),

$$\varepsilon_i = \frac{1}{\Delta x^2} + \frac{1}{\Delta y^2}, \quad V_{i,i\pm 1}^x = \frac{-1}{2\Delta x^2}, \quad V_{j,j\pm 1}^y = \frac{-1}{2\Delta y^2}. \quad (2.3)$$

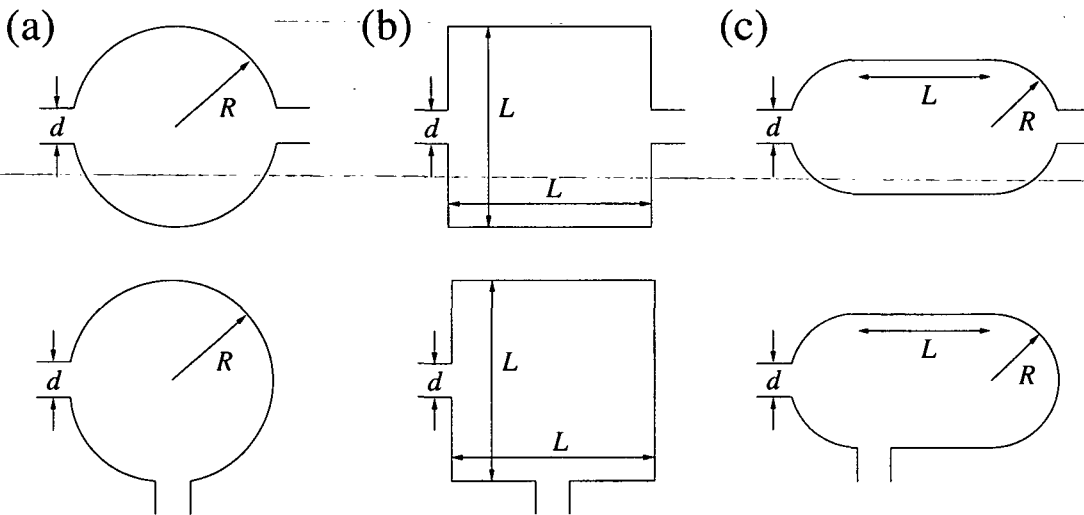


Figure 2.1: Quantum billiards investigated in this work: (a) circle, (b) rectangle and (c) stadium billiards each with parallel and perpendicular orientation of leads. Entrance and exit leads are chosen to have the same width. If not stated otherwise, the area of the billiards $A^{\text{dot}} = 4 + \pi$ and the lead with $d = 0.25$. The billiards (a) and (b) exhibit regular classical dynamics and the stadium billiard (c) shows chaotic behaviour.

With the help of the eigenvectors $|\psi_m\rangle$ and the eigenvalues E_m of the Hamiltonian \hat{H}^{tb} the Green's functions of one-dimensional tb strips are calculated, each of which takes the form

$$G^\pm(\mathbf{r}, \mathbf{r}', E) = \lim_{\epsilon \rightarrow \pm 0} \sum_m \frac{\langle \mathbf{r} | \psi_m \rangle \langle \psi_m | \mathbf{r}' \rangle}{E \pm i\epsilon - E_m}. \quad (2.4)$$

The different signs (\pm) denote the retarded and advanced Green's functions respectively. The eigenfunctions appearing in Eq. (2.4) are orthonormalized on each strip $\langle \psi_n | \psi_m \rangle = \delta_{mn}$. The disconnected transverse strips are placed next to each other such that their bottom and top ends follow the specific boundary conditions as accurately as possible (see Fig. 2.2). To connect all the strips with each other the Green's function is calculated by successively adding transverse strips through recursive solutions of a Dyson equation. The complete scattering structure can thus be assembled from the individual strips much like knotting a carpet.

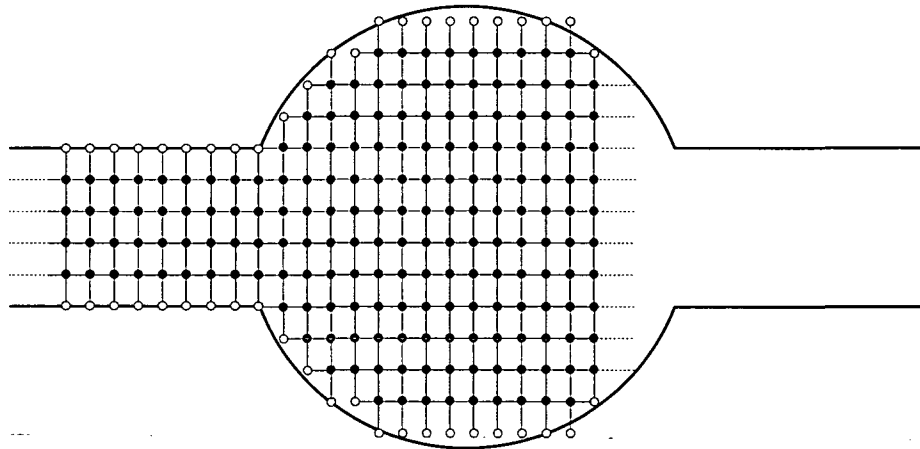


Figure 2.2: *Illustration of the discretization procedure employed in the standard RGM: Cartesian tight-binding strips are recursively connected to each other. The hard wall boundary conditions at the sites on the border of the transverse strips are represented by empty circles (accessible space by full circles). Smooth boundaries can only be inadequately approximated by the Cartesian grid.*

Mathematically speaking each recursion amounts to solving a matrix Dyson equation of the form

$$G = G^0 + G^0 \bar{V} G, \quad (2.5)$$

where G^0 and G denote the retarded Green's functions of the disconnected and the connected tb strips, respectively. The matrix \bar{V} denotes the hopping potential V multiplied by the size of the unit cell $\bar{V} = V \Delta_R$, which in a Cartesian grid is $\Delta_R = \Delta x \Delta y$. The number of necessary recursions [i.e. solutions of (2.5)] is equal to the number of transverse strips. The shorter the electron wavelength, the higher the number of recursions (i.e. number of matrix inversions). This requirement renders transport calculations for very small wavelengths eventually impractical.

Finally, the Green's functions for (a) the scattering region and for (b) the in- and outgoing leads are connected with each other. Note that the expressions for (b)

can be calculated analytically [49, 50]. Once the Green's function G^{tot} for the total scattering geometry is assembled, the transmission amplitudes t_{nm} from entrance lead mode m into exit lead mode n can be calculated by projecting G^{tot} onto the transverse wavefunctions in the leads $\chi_n(y_i)$,

$$t_{nm}(E_F) = -i\sqrt{k_{x_2,n}k_{x_1,m}} \int_{-d/2}^{d/2} dy_2 \int_{-d/2}^{d/2} dy_1 \chi_n^*(y_2) G^{\text{tot}}(y_2, y_1, E_F) \chi_m(y_1) \quad (2.6)$$

$$r_{nm}(E_F) = \delta_{nm} - i\sqrt{k_{x_1,n}k_{x_1,m}} \int_{-d/2}^{d/2} dy_1' \int_{-d/2}^{d/2} dy_1 \chi_n^*(y_1') G^{\text{tot}}(y_1', y_1, E_F) \chi_m(y_1), \quad (2.7)$$

where $k_{x_i,n}$ denotes the corresponding longitudinal wave numbers,

$$k_{x_i,n} = \sqrt{k_F^2 - \left(\frac{n\pi}{d}\right)^2}. \quad (2.8)$$

The indices n, m run over all possible transverse modes (sine waves), which are determined by the hard wall boundary conditions at $y = \pm d/2$. The wave numbers $k_{x_i,n}$ are real for $n\pi/d < k_F$ (open channel). For $n\pi/d > k_F$, we have a $k_{x_i,n}$ which is purely imaginary (closed channel). Current conservation is expressed through the unitarity of the S matrix, which consists of the transmission and reflection amplitudes,

$$\sum_{n=1}^M (|t_{nm}|^2 + |r_{nm}|^2) = 1. \quad (2.9)$$

The integer M denotes the number of open channels in the leads. According to the Landauer formula [51], the total conductance g through the quantum dot is given by

$$g = \frac{1}{\pi} \sum_{m,n=1}^M |t_{nm}|^2 = \frac{1}{\pi} T^{\text{tot}} \quad \text{with} \quad T^{\text{tot}} + R^{\text{tot}} = M. \quad (2.10)$$

2.2 The modular recursive Green's function method

To calculate the Green's function for an arbitrarily shaped scattering structure with the RGM can be a very time consuming procedure. This is because the number of large matrices which have to be inverted in the strip-by-strip recursion process can itself be very large. In addition, the RGM suffers from a slow convergence towards the continuum solution as a function of the grid density. This is in particular the case when the boundary does not have the same Cartesian shape the grid structure itself has, but is a smoothly varying curve which can only be crudely approximated by the tight-binding grid (as illustrated in Fig. 2.2).

The remedy which we propose to overcome such difficulties goes back to Sols *et al.* [17] and consists of an extension of the RGM. Starting point is the observation that many prototypical non-separable quantum dot geometries are built up out of simpler

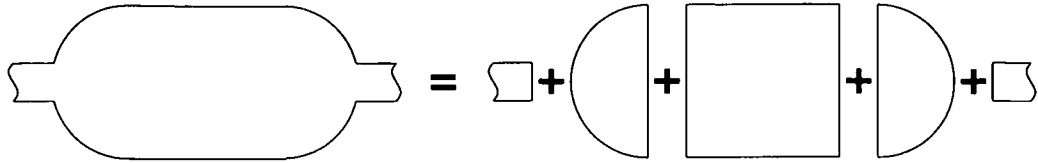


Figure 2.3: *Schematic illustration of the modular recursive Green's function method as applied to the stadium with opposite leads.*

separable structures. This is e.g. the case for all the scattering geometries displayed in Fig. 2.1: the circle, rectangle and stadium shaped quantum dot. These scattering devices can all be assembled from rectangular and spherical substructures, in the following referred to as modules. The example of a stadium billiard with parallel leads is illustrated in Fig. 2.3.

Because of the separability of the *continuum* Helmholtz equation in each of these modules, the wave function and hence the Green's function can be calculated either analytically or by one-dimensional quadrature essentially exactly. This statement remains true for the *discretized* Green's functions of these modules provided that a symmetry-adapted discretization is employed. For the spherical modules this requirement demands e.g. a discretization on a polar tb lattice as displayed in Fig. 2.4. For joining modules with each other we employ the technique of the RGM where the coupling between Green's functions is facilitated in terms of the corresponding hopping matrix elements of the tight-binding Hamiltonian. A matrix Dyson equation has to be solved only once at each junction between the modules. The complete scattering structure can thus be assembled from the individual modules much like a jigsaw puzzle. In comparison with the strip-by-strip recursion the number of necessary recursions is thereby drastically reduced. Furthermore the sections of the boundary with any other than a rectangular shape are optimally approximated by the symmetry adapted tight-binding grid of the corresponding module in contrast to the Cartesian grid used in the conventional RGM.

Our modular method can be applied to all geometries consisting of modules the boundaries of which follow the nodal lines of Cartesian, polar, elliptic, or hyperbolic coordinates. The most straightforward examples of Cartesian and polar grids will be illustrated in the following.

2.3 Non-Cartesian tight-binding grids

Starting point for any symmetry-adapted grid is the structure of its tight-binding Hamiltonian. For the case of a module with rectangular boundary the tb Hamiltonian and the corresponding hopping potentials of its Cartesian grid are identical to those of the RGM discussed above [see Eqs. (2.1,2.3)]. On a polar grid the discretization of the Schrödinger equation is somewhat more involved. This is because a straightforward approach to the discretization on a polar grid fails: A replacement of the derivatives in the polar coordinate representation of the free-particle

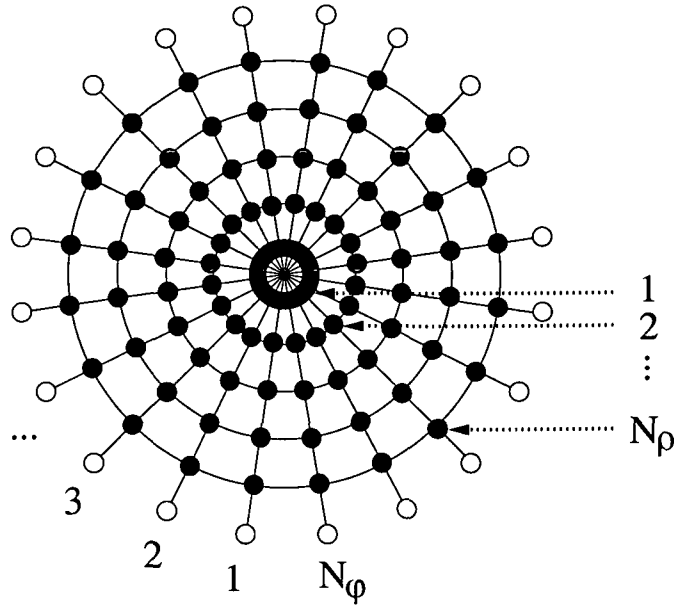


Figure 2.4: Polar discretization on a circular module with N_φ angular and N_ρ radial grid points.

Hamiltonian

$$-\frac{1}{2} \left[\frac{1}{\rho} \frac{\partial}{\partial \rho} \left(\rho \frac{\partial \psi}{\partial \rho} \right) + \frac{1}{\rho^2} \frac{\partial^2 \psi}{\partial \varphi^2} \right] \psi_m = E_m \psi_m \quad (2.11)$$

by finite difference operators leads to serious discretization errors especially around the origin ($\rho = 0$). To remedy this matter we derive the discretization formulæ based on a variational principle which involves the Lagrangian L and its density \mathcal{L} ,

$$L = \int d^2 \mathbf{x} \mathcal{L} = \int r dr \int d\varphi \mathcal{L} \quad (2.12)$$

$$\mathcal{L} = E \psi^* \psi - \frac{1}{2} \vec{\nabla} \psi^* \cdot \vec{\nabla} \psi - V \psi^* \psi. \quad (2.13)$$

In the continuum case the Schrödinger equation is obtained from the Lagrangian by applying the *functional derivative*,

$$\frac{\delta L}{\delta \psi^*} = -\vec{\nabla} \cdot \frac{\partial \mathcal{L}}{\partial \vec{\nabla} \psi^*} + \frac{\partial \mathcal{L}}{\partial \psi^*} = 0. \quad (2.14)$$

Let ψ depend on a parameter ξ . A small variation of ψ corresponds to a $\partial \psi / \partial \xi$ that is zero everywhere, except in a small region R , of volume Δ_R , around some point \mathbf{x} . In that sense, the functional derivative can be defined by the following limit,¹

$$\frac{\delta L}{\delta \psi^*} = \lim_{R \rightarrow 0^+} \frac{1}{\Delta_R} \frac{dL/d\xi}{d\psi^*/d\xi}. \quad (2.15)$$

¹For details check [52], chapter 9.

If we first discretize the Lagrangian and then solve Eq. (2.15) in a discrete way, we can be sure to obtain symmetric (or Hermitian) difference equations [53]. In the field-free case this discretization procedure takes the following form:

$$L = \int \rho d\rho \int d\varphi \left[E \psi^* \psi - \frac{1}{2} \left(\frac{\partial}{\partial \rho} \psi^* \frac{\partial}{\partial \rho} \psi + \frac{1}{\rho^2} \frac{\partial}{\partial \varphi} \psi^* \frac{\partial}{\partial \varphi} \psi \right) \right] \longrightarrow \quad (2.16)$$

$$L^{\text{dis}} = \sum_i \Delta \rho \sum_j \Delta \varphi \left[\rho_i E \psi_{i,j}^* \psi_{i,j} - \frac{1}{2} \left(\rho_{i-1/2} \frac{\psi_{i,j}^* - \psi_{i-1,j}^*}{\Delta \rho} \frac{\psi_{i,j} - \psi_{i-1,j}}{\Delta \rho} + \frac{1}{\rho_i} \frac{\psi_{i,j}^* - \psi_{i,j-1}^*}{\Delta \varphi} \frac{\psi_{i,j} - \psi_{i,j-1}}{\Delta \varphi} \right) \right] \quad (2.17)$$

In the discrete case Δ_R is the volume of the unit cell in the polar grid ($\Delta_R = \rho_i \Delta \rho \Delta \varphi$). The parameter that we vary is the wave function $\psi_{i,j}^*$ at the radial grid-point $\rho_i = |i - 1/2| \Delta \rho$ and the angular site $\varphi_j = j \Delta \varphi$. Note that we place the first grid point in radial direction at the position $\rho_1 = 0.5 \Delta \rho$, which is essential to properly discretize the center of the circular module. A straightforward discretization with gridpoints at $\rho_i = i \Delta \rho$ would lead to errors in the convergence towards the continuum solution around $\rho = 0$.

Approximating the functional derivative by

$$0 = \frac{\delta L}{\delta \psi^*} \approx \frac{1}{\rho_i \Delta \rho \Delta \varphi} \frac{dL^{\text{dis}}}{d\psi_{i,j}^*}, \quad (2.18)$$

leads us from Eq. (2.17) to the following Schrödinger equation

$$E \psi_{i,j} = -\frac{1}{2\rho_i \Delta \rho^2} (\rho_{i-1/2} \psi_{i-1,j} - 2\rho_i \psi_{i,j} + \rho_{i+1/2} \psi_{i+1,j}) - \frac{1}{2\rho_i^2 \Delta \varphi^2} (\psi_{i,j-1} - 2\psi_{i,j} + \psi_{i,j+1}). \quad (2.19)$$

Comparing Eq. (2.19) with the general form of a tight-binding Hamiltonian (2.1) we can directly read off the hopping matrix elements V_{ρ_i} (V_φ) for hopping from one site to its nearest neighbour in ρ (φ) direction,

$$\varepsilon_i = \frac{1}{\Delta \rho^2} + \frac{1}{\rho_i^2 \Delta \varphi^2}, \quad V_{\rho_i} = -\frac{1}{2\rho_i \Delta \rho^2} \rho_{i\pm 1/2}, \quad V_\varphi = -\frac{1}{2\rho_i^2 \Delta \varphi^2}. \quad (2.20)$$

The different signs (\pm) in Eq. (2.20) depend on whether we hop from ρ_i to $\rho_{i+1} \rightarrow (+)$ or to $\rho_{i-1} \rightarrow (-)$.

2.4 Inclusion of a magnetic field

In the previous section we illustrated how the separability of the continuum Schrödinger equation can be maintained also in its discretized form if the correct grid

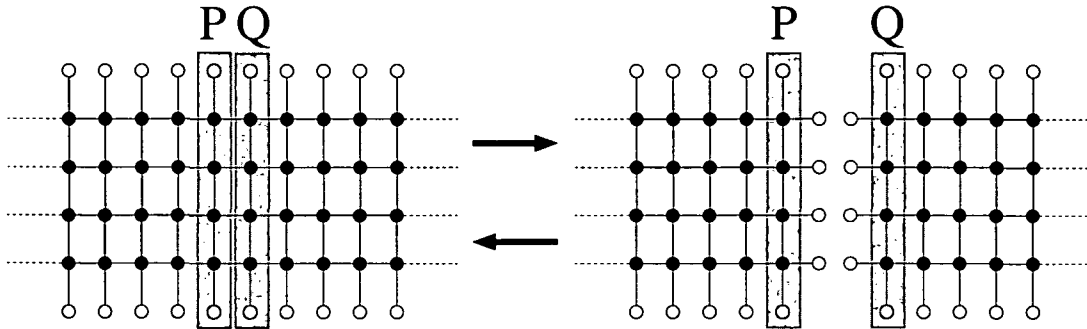


Figure 2.5: *Joining and disconnecting of modules by application of a Dyson equation for the example of two semi-infinite leads. The gray shaded areas P and Q are those grid slices at which the Green's functions are evaluated (see text).*

structure is employed. Since we also include a magnetic field in our method not only the specific form of the grid, but also the field gauge must be incorporated such that the separability persists within a given module.

The field $\mathbf{B} = (0, 0, B)$ enters the tb Hamiltonian (2.1) by means of a Peierls phase factor [18, 54],

$$V_{\mathbf{r},\mathbf{r}'} \longrightarrow V_{\mathbf{r},\mathbf{r}'} \cdot \exp \left[i/c \int_{\mathbf{r}}^{\mathbf{r}'} \mathbf{A}(\mathbf{x}) d\mathbf{x} \right], \quad (2.21)$$

with which the field-free hopping potential $V_{\mathbf{r},\mathbf{r}'}$ is multiplied. The vector potential $\mathbf{A}(\mathbf{r})$ satisfies $\nabla \times \mathbf{A}(\mathbf{r}) = \mathbf{B}$. The Peierls phase will, of course, in most cases destroy the separability of the eigenfunctions of \hat{H}^{tb} . The resulting difficulties can be, in part, circumvented by exploiting the gauge freedom of the vector potential, i.e.,

$$\mathbf{A} \rightarrow \mathbf{A}' = \mathbf{A} + \nabla \lambda, \quad (2.22)$$

where $\lambda(\mathbf{r})$ is a scalar function. By an appropriate choice of λ the wavefunction remains separable on a given symmetry adapted grid. Specifically, to preserve separability, we employ the Landau gauge for a Cartesian grid

$$\mathbf{A} = (-By, 0, 0), \quad (2.23a)$$

and the "symmetric" or circular gauge for a polar grid

$$\mathbf{A} = B/2(-y, x, 0) = \boldsymbol{\rho} \times \mathbf{B}/2. \quad (2.23b)$$

The scalar gauge potential generating the gauge transformation from (2.23a) to (2.23b) is $\lambda(x, y) = Bxy/2$.

A major complication results from the fact that in the presence of the magnetic field the separability on an unrestricted grid of a given symmetry does not imply the separability in the presence of boundary conditions of the same symmetry. We illustrate this problem with the help of one typical example, the *semi-infinite* quantum wire with lead width d (Fig. 2.5). We impose hard-wall boundary conditions $\psi(x, y = \pm d/2) = 0$ and consider first the *infinite* quantum wire along the x direction. Because of the Cartesian boundary conditions, the symmetry adapted gauge is

the Landau gauge $\mathbf{A} = -By\hat{\mathbf{x}}$. Consider, for notational simplicity, the Schrödinger equation in the continuum limit,

$$\begin{aligned} H\phi(y, x) &= \frac{1}{2} \left(\mathbf{p} + \frac{1}{c} \mathbf{A} \right)^2 \phi(x, y) = \\ &= \frac{1}{2} \left(-\frac{\partial^2}{\partial x^2} - \frac{\partial^2}{\partial y^2} - \frac{i2B}{c} y \frac{\partial}{\partial x} + \frac{B^2 y^2}{c^2} \right) \phi(x, y) = E_F \phi(x, y). \end{aligned} \quad (2.24)$$

Since the longitudinal momentum $p_x = -i\partial/\partial x$ commutes with H , the separability of the wavefunction persists in the presence of the magnetic field: $\phi(x, y) = f_k(x)\chi(y)$ with $f_k(x) = e^{ikx}$. If, however, one introduces an additional Cartesian boundary condition along the y -axis [i.e. $\psi(x=0, y) = 0$ for a semi-infinite lead] the situation changes. In the absence of the magnetic field, $B = 0$, the linear term in p_x vanishes and thus the choice $f(x) = \sin(kx)$ [i.e. a linear combination of $f_{\pm k}(x)$] satisfies the boundary condition and preserves the separability, even though p_x is no longer conserved in the semi-infinite lead. However, for $B \neq 0$ and the same boundary condition $\psi(x=0, y) = 0$, the term linear in B and p_x destroys the separability. The wavefunction takes now the general form

$$\phi(x, y) = \sum_m e^{ik_m x} \sum_n c_{mn} \chi_{mn}(y). \quad (2.25)$$

The breakdown of separability by the introduction of an additional boundary condition indicates that the Green's function of confined modules will be more complex than for extended systems for the same symmetry adapted grid and the same gauge. Therefore, the program of the modular method of building-up extended complex structures by "welding together" smaller modules of higher symmetry will be executed in reverse: non-separable confined modules will be generated by "cutting in pieces" larger separable modules. Confining boundary conditions will be introduced rather than removed by the matrix Dyson equation. In the example above, the *semi-infinite* quantum wire is generated by cutting the *infinite* wire at the line $x=0$, thereby imposing the additional boundary condition. Just as connecting modules, so is disconnecting a given module equivalent to the application of a matrix Dyson equation,

$$G^E = G^C + G^C \bar{V} G^E. \quad (2.26)$$

In this context G^E (G^C) is the Green's function of the extended (confined) module and \bar{V} is the hopping potential that connects the modules. Solving (2.26) *in reversed mode* (i.e. for G^C rather than for G^E) amounts to dissecting the larger module.

2.5 Calculation of modules

This section is dedicated to the evaluation of the Green's functions for those modules, which we need to assemble the circle, the rectangle, and the stadium billiard (see Fig. 2.1): the half-infinite lead, the rectangle, the circle, and the half-circle. The straightforward procedure to obtain module Green's functions is to work with their

spectral representation in the separable energy eigenstates of the modules $|E_m\rangle = |E_k\rangle \otimes |E_{k,n}\rangle$. With further simplification of Eq. (2.4) we have in this case,

$$G^\pm(\mathbf{r}, \mathbf{r}', B, E_F) = \lim_{\epsilon \rightarrow \pm 0} \sum_k \langle \alpha | E_k \rangle \langle E_k | \alpha' \rangle \sum_n \frac{\langle \beta | E_{kn} \rangle \langle E_{kn} | \beta' \rangle}{E_F \pm i\epsilon - E_{kn}}, \quad (2.27)$$

where (α, β) either stand for the coordinates (x, y) or (ϱ, φ) . The indices (k, n) represent the quantum numbers of the separable eigenfunctions $|E_k\rangle, |E_{k,m}\rangle$ associated with the degrees of freedom α and β respectively.

With the exception of the circular module, Eq. (2.27) can however not be used without further modifications. This is due to the non-separability for confined geometries as discussed above. Moreover the spectrum in open structures such as the semi-infinite lead is continuous rather than discrete. Unlike in the field-free case [49], the resulting integrals cannot be calculated analytically. As will be shown in the following, both problems can be overcome by applying the matrix Dyson equation in a non-standard way.

To connect modules of different grid structure additional *link modules* are required. In Fig. 2.8 we illustrate how for assembling a stadium billiard such a link module is plugged in between a half-circle and a rectangle. The key property of these link modules is their adaption to two grid symmetries [50, 55]. In such a way we avoid spurious reflections that would arise at the junction between different modules. The details for calculating the Green's functions for all the modules mentioned above are given in the following.

2.5.1 Rectangular module

For the semi-infinite wave guide the Dirichlet boundary condition for the confined structure of a rectangle with magnetic field is not separable, no matter which gauge is chosen. The separability can however be restored by imposing periodic boundary conditions on two opposing sides of the rectangle. Topologically, this corresponds to folding the rectangle to the surface of a cylinder (Fig. 2.6). In this case we connect the first (P) and the last (Q) transverse grid slice of a rectangular grid by a hopping potential $|V_{PQ}^x| = |V_{QP}^x| = \frac{-1}{2\Delta x^2}$. The Green's function of this "cylinder surface" (cs) will be denoted by G^{cs} in the following. The rectangle Green's function G^r will be obtained out of G^{cs} by a Dyson equation used here in "reversed" mode, i.e. for *disconnecting* tb grids. This method for calculating the rectangular module may seem like a detour, but it is numerically more efficient than a strip-by-strip recursion. For completeness we mention that an alternative way to calculate G^r was proposed in Ref. [56].

The Green's function for the cylinder surface G^{cs} can be constructed from separable eigenfunctions, $|E_m\rangle = |E_k^x\rangle \otimes |E_{kn}^y\rangle$, according to Eq. (2.27). Solving the tight-binding Schrödinger equation for the cylinder surface, we obtain for the longitudinal eigenstates

$$\langle x_j | E_k^x \rangle = (N_x \Delta x)^{-1/2} \exp(i2\pi k j / N_x), \quad (2.28)$$

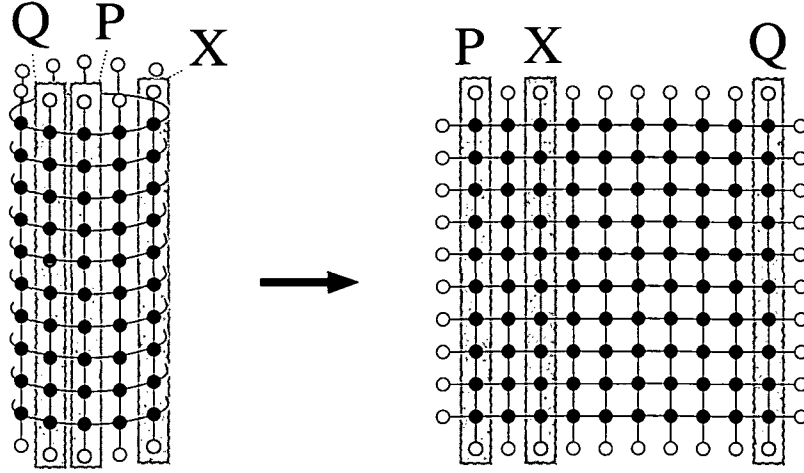


Figure 2.6: Applying a Dyson equation in “reversed mode” to construct Green’s functions for a rectangle out of a cylinder surface. By this procedure the periodic boundary conditions are transformed into hard wall boundary conditions. The gray shaded areas P , Q and X are those grid slices at which the Green’s functions are evaluated (see text).

which results in a tridiagonal, symmetric matrix-eigenproblem of size $N_y \times N_y$ for the transverse modes [57],

$$E_{kn} \langle y_l | E_{kn}^y \rangle = \frac{-1}{\Delta x^2} \left[\cos \left(\frac{2\pi k}{N_x} + \frac{B}{c} y_l \Delta x \right) - 1 \right] \times \langle y_l | E_{kn}^y \rangle - \frac{1}{2\Delta y^2} (\langle y_{l-1} | E_{kn}^y \rangle - 2\langle y_l | E_{kn}^y \rangle + \langle y_{l+1} | E_{kn}^y \rangle). \quad (2.29)$$

By “cutting the cylinder surface open” along a line of constant x , we obtain from G^{cs} the desired Green’s function G^{r} for the rectangle (Fig. 2.6). We demonstrate this for the rectangle Green’s function G_{PX}^{r} from the first transverse slice P to any other slice X . To determine G_{PX}^{r} we solve the following system of Dyson equations,

$$G_{PX}^{\text{r}} = G_{PX}^{\text{cs}} - G_{PQ}^{\text{r}} \bar{V}_{QP} G_{PX}^{\text{cs}} - G_{PP}^{\text{r}} \bar{V}_{PQ} G_{QX}^{\text{cs}} \quad (2.30)$$

$$G_{PQ}^{\text{cs}} = G_{PQ}^{\text{r}} + G_{PQ}^{\text{r}} \bar{V}_{QP} G_{PQ}^{\text{cs}} + G_{PP}^{\text{r}} \bar{V}_{PQ} G_{QQ}^{\text{cs}} \quad (2.31)$$

$$G_{PP}^{\text{cs}} = G_{PP}^{\text{r}} + G_{PQ}^{\text{r}} \bar{V}_{QP} G_{PP}^{\text{cs}} + G_{PP}^{\text{r}} \bar{V}_{PQ} G_{QP}^{\text{cs}}, \quad (2.32)$$

where the first line is the “reversed” Dyson equation. The three unknowns in the above equations are the Green’s functions connecting the slices (P, X) , (P, Q) and (P, P) , are: G_{PX}^{r} , G_{PQ}^{r} , G_{PP}^{r} . By solving these three equations, the unknowns can be uniquely determined.

2.5.2 Circle and half-circle

In symmetric gauge, $\mathbf{A} = B/2(-y, x, 0)$, the Dirichlet boundary value problem for the circle with magnetic field is separable, $|E_m\rangle = |E_k^\varphi\rangle \otimes |E_{kn}^g\rangle$. On a discrete tb

lattice this statement remains true, provided that a circular grid is employed (see section 2.3). With the eigenstates for the azimuthal degree of freedom,

$$\langle \varphi_j | E_k^\varphi \rangle = (N_\varphi \Delta\varphi)^{-1/2} \exp(i2\pi kj/N_\varphi), \quad (2.33)$$

and radial eigenstates,

$$g_{kn}(\varrho_i) = \sqrt{\varrho_i} \times \langle \varrho_i | E_{kn}^g \rangle, \quad (2.34)$$

the finite difference equation for the $g_{kn}(\varrho_i)$ results in a tridiagonal symmetric eigenproblem,

$$E_{kn} g_{kn}(\varrho_i) = -\frac{1}{\varrho_i^2 \Delta\varphi^2} \left[\cos \left(\frac{2k\pi}{N_\varphi} - \frac{\varrho_i^2 B \Delta\varphi}{2c} \right) - 1 \right] g_{kn}(\varrho_i) \quad (2.35)$$

$$-\frac{1}{2\Delta\varrho^2} \left[\frac{\varrho_{i-1/2}}{\sqrt{\varrho_{i-1}}\sqrt{\varrho_i}} g_{kn}(\varrho_{i-1}) - 2g_{kn}(\varrho_i) + \frac{\varrho_{i+1/2}}{\sqrt{\varrho_i}\sqrt{\varrho_{i+1}}} g_{kn}(\varrho_{i+1}) \right].$$

The Green's function for the circular module is then calculated by a straight-forward application of Eq. (2.27).

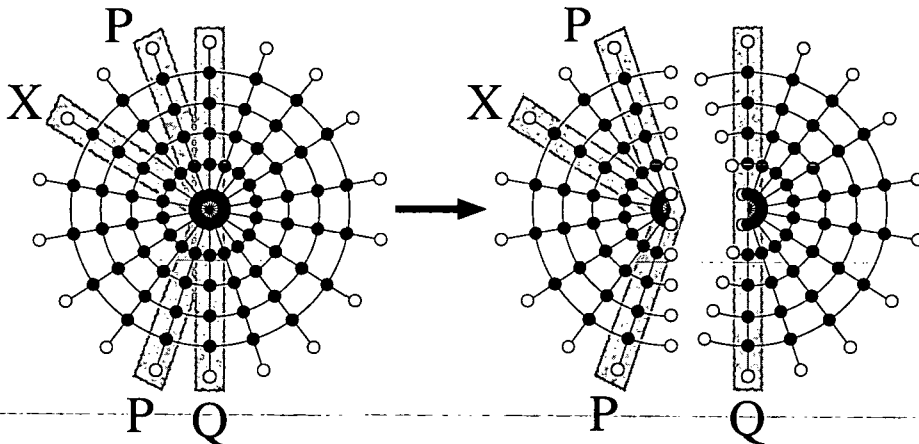


Figure 2.7: The Green's function for the half-circular module is obtained by splitting a circular module into two halves. For details see text.

For the Green's function of the half-circle we employ an analogous procedure as in the previous section: we dissect the circle Green's function into half-circles by means of a "reversed" Dyson equation. We demonstrate this by way of the example depicted in Fig. 2.7, where the "full circle" (fc) is split up into two "half-circles" (hc). The resulting two halves are almost identical, with the exception of the two additional radial grid slices, by which the right half-circle is larger. For assembling the stadium billiard we have to make sure that the tb grid of the half-circle module can be linked directly to a vertical grid (see Fig. 2.8). For this reason, only the left one of the two half-circles in Fig. 2.7 can be used for this purpose.

Consider as example the Green's function G_{PX}^{hc} describing the propagation from the grid slice P at the junction of the two half-circles to any radial grid slice X situated

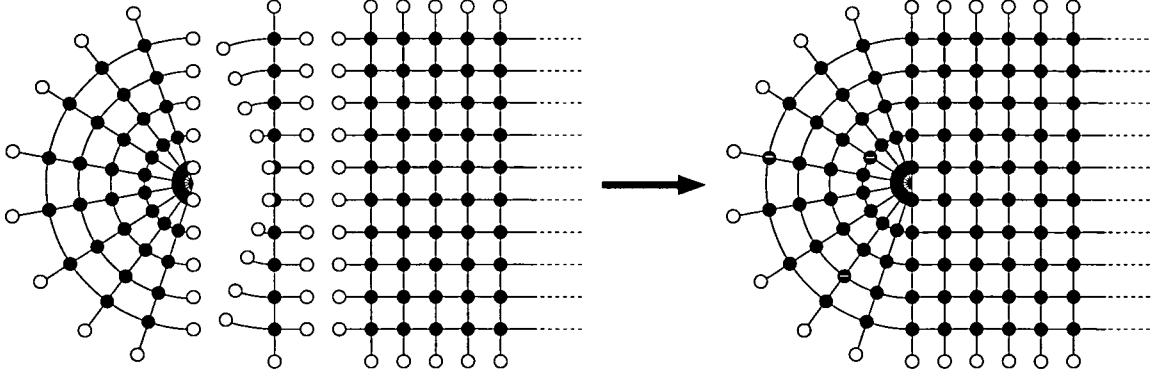


Figure 2.8: Applying a Dyson equation to construct Green's functions for a stadium billiard out of "modules". An additional link module is added to join the half-circle and the rectangle module.

on the "left half-circle" (see Fig. 2.7). G_{PX}^{hc} is determined by the following system of Dyson equations

$$G_{PX}^{\text{hc}} = G_{PX}^{\text{fc}} - G_{PP}^{\text{hc}} \bar{V}_{PQ} G_{QX}^{\text{fc}} \quad (2.36)$$

$$G_{PP}^{\text{fc}} = G_{PP}^{\text{hc}} + G_{PP}^{\text{hc}} \bar{V}_{PQ} G_{QP}^{\text{fc}} \quad (2.37)$$

which yields a unique solution for G_{PX}^{hc} .

2.5.3 Link module

When trying to connect a rectangular with a circular module (as required for assembling the stadium billiard) the problem occurs of how to link the two different grid structures with each other. To keep the tb Hamiltonian at the junction of the two modules Hermitian, the absolute value of the potential for hopping from one module to the other must be the same as for hopping in the opposite direction. This requirement is difficult to fulfill since V_φ is dependent on the radial position in the module and V_x is not. To overcome this problem we insert an additional link module at the junction between the rectangle and the half-circle (see Fig. 2.8 for a graphical illustration). These link modules are essentially one-dimensional tb strips the site energies of which contain contributions from both adjacent grid structures. In this sense the link module is half a polar wedge and half a Cartesian strip (see Fig. 2.9). This property is reflected in its Lagrangian from which we start out,

$$L = \int_0^R \varrho d\varrho \int_{\pm(\pi+\Delta\varphi)/2}^{\pm\pi/2} d\varphi \left[E \phi^* \phi - \frac{1}{2} \left(\frac{\partial}{\partial \varrho} \phi^* \frac{\partial}{\partial \varrho} \phi + \frac{1}{\varrho^2} \frac{\partial}{\partial \varphi} \phi^* \frac{\partial}{\partial \varphi} \phi \right) \right] \quad (2.38)$$

$$+ \int_{-R}^R dy \int_0^{\Delta x/2} dx \left[E \phi^* \phi - \frac{1}{2} \left(\frac{\partial}{\partial x} \phi^* \frac{\partial}{\partial x} \phi + \frac{\partial}{\partial y} \phi^* \frac{\partial}{\partial y} \phi \right) \right].$$

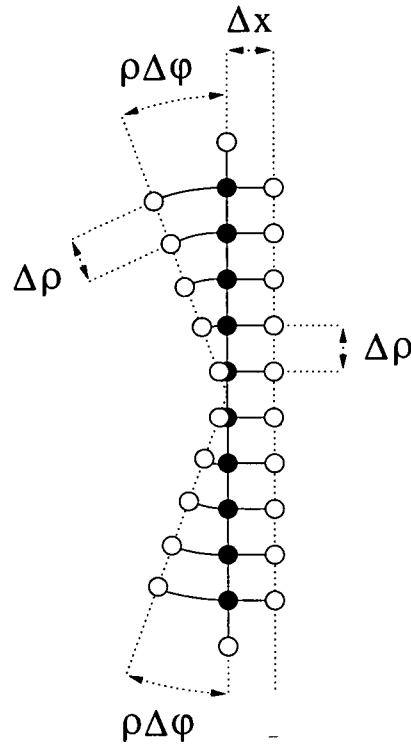


Figure 2.9: The link module for the connection between a half-circle and a rectangle, as required to assemble a stadium billiard.

We now discretize this equation on three neighbouring chains, one being of polar origin, the other Cartesian and in the middle we have a “hybrid” strip. On these chains we approximate the first derivatives of Eq. (2.38) after which the wave function is set to zero on the two outer chains. The resulting Lagrangian only contains elements of the wave function ϕ_i on the sites of the middle strip,

$$x = 0, \quad y_i = (i - 1/2)\Delta y \quad \longleftrightarrow \quad \varphi = \pm \frac{\pi}{2}, \quad \varrho_i = |i - 1/2|\Delta r. \quad (2.39)$$

With the identity $\Delta y = \Delta \varrho$ we have,

$$\begin{aligned} L^{\text{dis}} = & \frac{\Delta \varphi}{2} \sum_i \Delta \varrho \left[\varrho_i E \phi_i^* \phi_i - \frac{1}{2} \left(\varrho_{i-1/2} \frac{\phi_i^* - \phi_{i-1}^*}{\Delta \varrho} \frac{\phi_i - \phi_{i-1}}{\Delta \varrho} + \frac{1}{\varrho_i} \frac{\phi_i^* \phi_i}{\Delta \varphi^2} \right) \right] \\ & + \frac{\Delta x}{2} \sum_i \Delta \varrho \left[E \phi_i^* \phi_i - \frac{1}{2} \left(\frac{\phi_i^* - \phi_{i-1}^*}{\Delta \varrho} \frac{\phi_i - \phi_{i-1}}{\Delta \varrho} + \frac{\phi_i^* \phi_i}{\Delta y^2} \right) \right]. \end{aligned} \quad (2.40)$$

For approximating the functional derivative of the Lagrangian on the grid, we employ Eq. (2.15) and insert for Δ_R the volume of the unit cell on the middle strip of the link module $\Delta_R = \Delta \varrho (\varrho_i \Delta \varphi + \Delta x)/2$. We then obtain

$$0 = \frac{\delta L}{\delta \phi^*} \approx \frac{2}{\Delta \varrho (\varrho_i \Delta \varphi + \Delta x)} \frac{dL^{\text{dis}}}{d\phi_i^*}. \quad (2.41)$$

Evaluating the above equation yields the eigen-equation of the tb Hamiltonian,

$$\begin{aligned}
E \frac{\Delta \varrho}{2} (\varrho_i \Delta \varphi + \Delta x) \phi_i = & \phi_i \left[\frac{\Delta \varrho \Delta \varphi}{2} \left(\frac{\varrho_i}{\Delta \varrho^2} + \frac{1}{\varrho_i \Delta \varphi^2} \right) + \frac{\Delta \varrho \Delta x}{2} \left(\frac{1}{\Delta y^2} + \frac{1}{\Delta x^2} \right) \right] \\
& - \frac{1}{2} \phi_{i+1} \left[\frac{\Delta \varrho \Delta \varphi}{2} \left(\frac{\varrho_{i+1/2}}{\Delta \varrho^2} \right) + \frac{\Delta \varrho \Delta x}{2} \left(\frac{1}{\Delta y^2} \right) \right] \\
& - \frac{1}{2} \phi_{i-1} \left[\frac{\Delta \varrho \Delta \varphi}{2} \left(\frac{\varrho_{i-1/2}}{\Delta \varrho^2} \right) + \frac{\Delta \varrho \Delta x}{2} \left(\frac{1}{\Delta y^2} \right) \right].
\end{aligned} \tag{2.42}$$

For a link module attached on a half-circle we have $i \in [-N_\varrho + 1, N_\varrho]$ and a wave-function which is zero on the boundary,

$$\phi_{-N_\varrho} = \phi_{N_\varrho+1} = 0. \tag{2.43}$$

Writing Eq. (2.42) in matrix notation results in a generalized eigenproblem of the form $\hat{A} |\phi\rangle = E \hat{B} |\phi\rangle$. The matrix \hat{A} is symmetric and \hat{B} is a diagonal matrix with elements

$$B_{ii} = \frac{\Delta \varrho}{2} (\varrho_i \Delta \varphi + \Delta x), \quad i \in \{-N_\varrho + 1, \dots, N_\varrho\}. \tag{2.44}$$

The generalized eigenvectors of \hat{A} are orthonormalized according to $\langle \phi | \hat{B} | \phi \rangle = \mathbb{1}$. This condition eventually yields the appropriate orthonormalization condition for the eigenstates in the double wedge,

$$\delta_{m,m'} = \sum_{i=-N_\varrho+1}^{N_\varrho} \phi_{[m],i} \phi_{[m'],i} \frac{\Delta \varrho}{2} (\varrho_i \Delta \varphi + \Delta x). \tag{2.45}$$

We note parenthetically that we could have derived the above scalar product also just based on the argument that each site in the link module has to be weighted with the corresponding size of its unit cell.

The Green's function for the link module G^{lm} is assembled from the eigenfunctions of the tb Hamiltonian in Eq. (2.42) by the help of Eq. (2.27). To link G^{lm} to the semi-circle Green's function, the hopping potential for the polar grid is used,

$$\bar{V}_\varphi = -\frac{1}{2} \frac{1}{\varrho_i^2 \Delta \varphi^2} \varrho_i \Delta \varrho \Delta \varphi. \tag{2.46}$$

To assemble a stadium billiard, the semi-circle with the link module attached to it is then connected to the rectangle Green's function G^{r} with

$$\bar{V}_x = -\frac{1}{2 \Delta x^2} \Delta x \Delta y. \tag{2.47}$$

As will be shown below, the magnetic field dependence of the link module can be easily incorporated by multiplying G^{lm} with a corresponding gauge phase factor [see Eq. (2.55)]. Due to the "1D nature" of G^{lm} , problems with the breaking of separability by the magnetic field do not occur here.

2.5.4 Semi-infinite lead

Because of its continuous spectrum, the Green's function for the semi-infinite lead poses an additional challenge beyond that of the non-separability of the wavefunction discussed above. We therefore apply one further "trick" to bypass this problem. Our approach is based on the observation that adding a slice to a semi-infinite quantum wire leaves this wire (up to irrelevant phases) invariant (see Fig. 2.10).

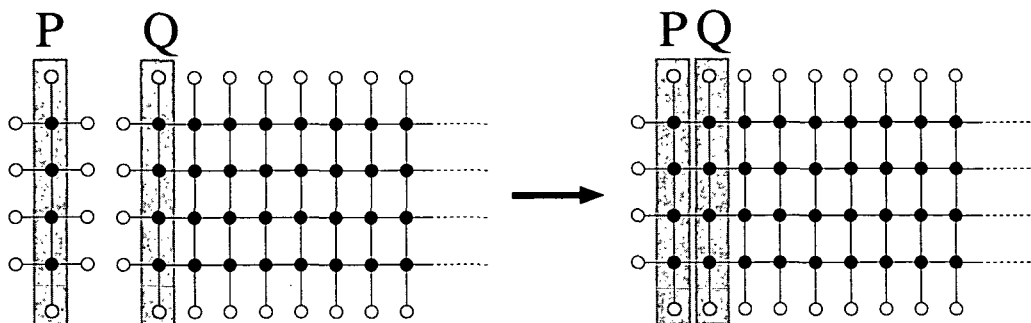


Figure 2.10: Applying a Dyson equation to construct Green's functions for a semi-infinite lead. Joining a transverse slice with a semi-infinite lead leaves the Green's function of the lead invariant.

We assume a semi-infinite lead with $x \in [\Delta x, \infty)$ and hard-wall boundary conditions at $x = \Delta x$ and $y = \pm d/2$. To this object we add a slice consisting of just one transverse chain of tb grid points which we place at $x = 0$. The system of Green's functions for the propagation from the transverse chain at $x = 0$ (P) back to itself (P) or to the first transverse slice of the semi-infinite lead (Q) at Δx reads

$$G_{PP} = G_{PP}^0 + G_{PP}^0 \bar{V}_{PQ} G_{QP}, \quad (2.48)$$

$$G_{QP} = G_{QQ}^0 \bar{V}_{QP} G_{PP}. \quad (2.49)$$

Each multiplication involves a matrix product with a dimension equal to the number of transverse grid points. The key point is now that the system of Eqs. (2.48,2.49) can be closed through the invariance condition (Fig. 2.10) for the semi-infinite lead, i.e. $G_{PP} = G_{QQ}^0$. In Landau gauge $\mathbf{A} = (-By, 0, 0)$ the latter relation does not even involve additional gauge phases since these are already contained in the hopping matrix element. We further note that an equivalent point of departure for the derivation of G_{PP} is the Bloch condition for states in the lead [22, 58]. Setting $Z = G_{PP} \bar{V}_{QP}$ and using the hermiticity condition $\bar{V}_{QP} = \bar{V}_{PQ}^* \equiv \bar{V}^*$, Eqs. (2.48,2.49) can be converted to a quadratic matrix equation

$$ZZ - \bar{V}^{-1} (G_{PP}^0)^{-1} Z + \bar{V}^{-1} \bar{V}^* = 0. \quad (2.50)$$

Solvents Z of a quadratic matrix equation, $Q(Z) = 0$, can be constructed from the eigenpairs (β_i, χ_i) of the corresponding quadratic eigenvalue equation $Q(\beta_i) \chi_i = 0$, $i \in [1, \dots, 2N]$ in the diagonal form [59],

$$Z = MBM^{-1} \quad \text{with} \quad M = [\chi_1, \dots, \chi_N], \quad B = \text{diag}(\beta_i). \quad (2.51)$$

The quadratic eigenvalue equation is equivalent to a generalized eigenvalue problem $A\tilde{\chi} = \beta C\tilde{\chi}$ of twice the original dimension [57]. Its $2N$ dimensional eigenvectors $\tilde{\chi} = (\chi, \beta\chi)$ are solutions of the symmetric eigenproblem

$$\begin{pmatrix} -\bar{V}^* & 0 \\ 0 & \bar{V} \end{pmatrix} \begin{pmatrix} \chi \\ \beta\chi \end{pmatrix} = \beta \begin{pmatrix} -(G_{PP}^0)^{-1} & \bar{V} \\ \bar{V} & 0 \end{pmatrix} \begin{pmatrix} \chi \\ \beta\chi \end{pmatrix}, \quad (2.52)$$

where $(G_{PP}^0)^{-1} = E_F - \hat{H}_{1D}^{tb}$ and \hat{H}_{1D}^{tb} is the Hamiltonian of the one-dimensional transverse tb strip at $x = 0$. The Fermi energy E_F and the magnetic field B enter (2.52) as independent parameters at which the eigenstates $\tilde{\chi}_m$ and eigenvalues β_m are evaluated. The longitudinal momenta of the lead states $\xi_m(x, y) = \chi_m(y)e^{ik_m x}/\sqrt{\theta_m}$ are related to the eigenvalues by the relation $\beta = \exp(ik\Delta x)$. The orthonormalization of the $2N$ eigenvectors $\tilde{\chi}_m$ can be formulated in terms of matrix relations, which, for the generalized eigenproblem, read

$$\frac{1}{\sqrt{\theta_m\theta_n}}\tilde{\chi}_m^T C\tilde{\chi}_n = 2i \frac{k_m}{|k_m|} \delta_{mn}. \quad (2.53)$$

Similarly we have for the completeness relation,

$$\sum_m^{2N} \frac{|k_m|}{k_m \theta_m} \tilde{\chi}_m \tilde{\chi}_m^T = 2i C^{-1}. \quad (2.54)$$

With this specific choice of normalization the norm factors θ_m are determined such that every propagating state carries unit flux. We note parenthetically that the quadratic eigenvalue equation Eq. (2.50) could also be applied to the semi-infinite lead at zero B field. However, in that case, the Green's function for quantum wires can be calculated analytically [49, 50] by complex contour integration.

2.6 Assembling all the modules

Provided that the Green's functions of all the necessary modules are available, we have to link them among each other to assemble the entire scattering geometry. However, in the presence of a magnetic field, we have to take into account that the different modules are calculated in different symmetry-adapted gauges. Joining modules requires, therefore, in general a gauge transformation $\mathbf{A} \rightarrow \mathbf{A}' = \mathbf{A} + \nabla\lambda$. For the Green's function on the grid, $G(\mathbf{r}_i, \mathbf{r}'_j)$, this transformation is simplified by the fact that the matrix of gauge transformations,

$$[\Lambda(\mathbf{r}_j)]_{jk} = \exp[-i\lambda(\mathbf{r}_j)/c] \delta_{jk}, \quad (2.55)$$

is diagonal in the grid representation. Correspondingly, the transformation of both the hopping potential \bar{V} and the Green's function is local, i.e.

$$\begin{aligned} \bar{V}(\mathbf{r}_i, \mathbf{r}'_j) &\rightarrow \bar{V}'(\mathbf{r}_i, \mathbf{r}'_j) = \Lambda(\mathbf{r}_i) \bar{V}(\mathbf{r}_i, \mathbf{r}'_j) \Lambda^*(\mathbf{r}'_j) \\ G(\mathbf{r}_i, \mathbf{r}'_j) &\rightarrow G'(\mathbf{r}_i, \mathbf{r}'_j) = \Lambda(\mathbf{r}_i) G(\mathbf{r}_i, \mathbf{r}'_j) \Lambda^*(\mathbf{r}'_j). \end{aligned} \quad (2.56)$$

It is thus not necessary to transform the gauges of different modules to one global gauge. Instead, it is sufficient to perform a local gauge transformation at the points of the junctions $\{r_i\}$, such that the gauges of the two modules to be joined agree *at these points*. Note, however, that gauge transformations are required not only when changing the gauge itself, but also when modules are shifted in space. Nevertheless, the number of gauge transformation required to assemble the total Green's function G^{tot} can be kept quite small. This is illustrated in the following with the help of the example of the stadium with parallel lead orientation (see Fig. 2.3). Starting point is the link module, which we line up along the y -axis, symmetrically around the origin. For "attaching" to it the half-circle no gauge transformation is required, since along the y -axis the link module is identical to its field-free form, no matter which gauge is chosen. Transforming the connected object (half-circle plus link module) from the symmetric to the Landau gauge allows to (a) shift it along the x -axis and (b) "attach" the rectangle to it, both without any further gauge transformation. For the second half-circle the procedure is similar. In the case of 180° lead orientation, the fully assembled stadium and the leads are already in the same gauge and can be directly connected. In the case of 90° lead orientation one additional gauge transformation at the junction of the rectangle with the exit lead is necessary.

To illustrate in detail how different modules are joined by solving a Dyson equation, we will focus on the connection of two adjacent modules: the semi-infinite lead and the half-circle (see Fig. 2.11). Consider e.g. the Green's function² describing the propagation from the radial slice L to the Cartesian slice J ,

$$G_{L,J} = \underbrace{G_{L,J}^0}_{=0} + G_{L,Q}^0 \bar{V}_{Q,P} G_{P,J} \quad (2.57)$$

with

$$\bar{V}_{Q,P} = V_{Q,P} \Delta_R = \bar{V}_{P,Q}^* = V_{P,Q}^* \Delta_R. \quad (2.58)$$

In Eq. (2.57), $G_{L,J}^0$ stands for the Green's function of the disconnected modules while $G_{L,J}$ is the Green's function of the connected, enlarged system. The indices P and Q refer to the slices of grid points on both sides of the gap between the modules to be connected. Note that the hopping matrix is weighted with the area of the unit cell of the tight-binding grid. Each multiplication in Eq. (2.57) stands for a matrix multiplication where the dimension is given by the number of sites within the slice. In order to close the system of matrix equations, two more Dyson equations are needed (see Fig. 2.11b)

$$G_{P,J} = G_{P,J}^0 + G_{P,P}^0 \bar{V}_{P,Q} G_{Q,J}, \quad (2.59)$$

and finally

$$G_{Q,J} = \underbrace{G_{Q,J}^0}_{=0} + G_{Q,Q}^0 \bar{V}_{Q,P} G_{P,J}. \quad (2.60)$$

From the coupled equations above and the boundary conditions at the borders we obtain

$$G_{L,J} = G_{L,Q}^0 \bar{V}_{Q,P} (1 - G_{P,P}^0 \bar{V}_{P,Q} G_{Q,Q}^0 \bar{V}_{Q,P})^{-1} G_{P,J}^0. \quad (2.61)$$

²In the following paragraphs we assume that all Green's functions are in the same gauge.

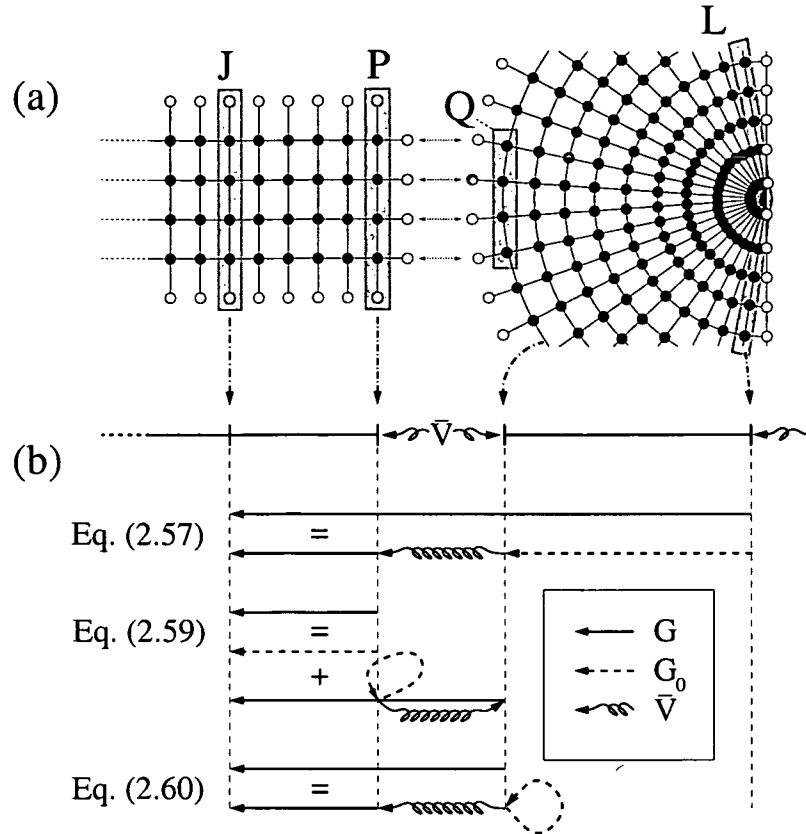


Figure 2.11: (a) Illustration of the joining of modules by recursions. As an example we show the connection of a lead to a half-circle. For these two modules no additional link module is required, provided that the lead width is small compared to the radius of the circle. (b) Diagrammatic illustration of the corresponding Dyson equations.

The recursion method outlined above has the advantage that it involves only one matrix inversion for connecting two entire modules. Furthermore, for connections performed at lead mouths, the dimension of the matrices involved along the border is small due to the small number of grid points required.

In the case of attaching a lead to a cylindrical module we can employ a very simple approximation such that the use of an additional link module can be avoided: Under the assumption that the opening of the lead is small compared to the radius of the module, we can approximate the arc of the circle at the lead mouth to be a straight line (see Fig. 2.11a). This approximation is valid as long as the wavelength of the electron is large compared to the mismatch between the grids. However, for keeping the Hamiltonian at this junction Hermitian, we have to make sure that the Cartesian hopping potential in propagating direction is equal to the radial component of the cylindrical hopping potential,

$$V^x = -\frac{1}{2\Delta x^2} = V_{N^e, N^{e+1}}^e. \quad (2.62)$$

We must also demand that the Cartesian and the cylindrical unit cells at the junction have the same size,

$$\Delta x \Delta y = \varrho_{Ne} \Delta \varrho \Delta \varphi. \quad (2.63)$$

These two conditions imply the following relations for the spacings in the Cartesian and the polar grid,

$$\Delta x = \sqrt{\frac{\varrho_{Ne}}{\varrho_{Ne+1/2}}} \Delta \varrho \quad \text{and} \quad \Delta y = \sqrt{\varrho_{Ne} \varrho_{Ne+1/2}} \Delta \varphi. \quad (2.64)$$

2.7 Transport coefficients

Once the Green's function for the total scattering problem G^{tot} is assembled, the transport coefficients t_{nm} and r_{nm} can be calculated. At zero magnetic field this evaluation proceeds just as described above [see Eqs. (2.6, 2.7)]. However, as soon as a magnetic field is also present in the leads, this procedure has to be modified to take into account the generalized orthogonality relation Eq. (2.53) for the transverse lead states χ_m at $B \neq 0$. In other words: To extract the S -matrix, the matrix elements of the current operator must be of gauge-invariant form. This requirement can be fulfilled by employing a double-sided gradient operator which is defined as [60]

$$f \vec{D} g = f(\mathbf{x}) \mathbf{D} g(\mathbf{x}) - g(\mathbf{x}) \mathbf{D}^* f(\mathbf{x}) = -g \vec{D} f \quad \text{with} \quad \mathbf{D} = \nabla - \frac{i}{c} \mathbf{A}(\mathbf{x}). \quad (2.65)$$

With its help the transmission amplitudes can be evaluated as [22, 58, 60]

$$t_{nm}(E_F, B) = -\frac{i}{4\sqrt{\theta_n \theta_m}} \int_{-d/2}^{d/2} dy_2 \int_{-d/2}^{d/2} dy'_1 \chi_n^*(y_2) e^{-ik_n x_2} (\vec{D} \cdot \hat{\mathbf{x}}_2)^* G^{\text{tot}}(\mathbf{x}_2, \mathbf{x}'_1, E_F, B) (\vec{D}' \cdot \hat{\mathbf{x}}'_1) \chi_m(y'_1) e^{ik_m x'_1}. \quad (2.66)$$

Primed and unprimed coordinates are situated in the entrance and exit lead respectively. The unit vectors $\hat{\mathbf{x}}_n$ are assumed to be pointing in outward direction of the n -th lead and θ_m denotes the outgoing particle flux carried by $\chi_m(y'_1) e^{ik_m x'_1}$ through the lead cross section.

The operator \vec{D} can be expressed in discretized space by a finite difference approximation of its derivative term. In this discretized form the operator \vec{D}^{dis} allows to rewrite the orthogonalization condition of the lead states (2.53) in the more compact notation

$$\frac{1}{\sqrt{\theta_m \theta_n}} \tilde{\chi}_m^T C \tilde{\chi}_n = \left[\xi_m \vec{D}^{\text{dis}} \xi_n \right]_{x=x_0} = 2i \frac{k_m}{|k_m|} \delta_{mn}. \quad (2.67)$$

In the above equation we employed the previously introduced lead states $\xi_m(x, y) = \chi_m(y) e^{ik_m x} / \sqrt{\theta_m}$ and fix the variable x at an arbitrary transverse strip in the lead ($x = x_0$). Equation (2.67) allows a very efficient evaluation of the transport coefficients in Eq. (2.66). We illustrate now the details for this procedure with the help of the example of two semi-infinite leads (depicted in Fig. 2.5). In this case the

Green's function which we need for the evaluation of Eq. (2.66) is $G^{\text{tot}} = G_{QP}^{i,+}$. This retarded (+) Green's function from the strip Q to the strip P in the infinite (i) lead consists of the Green's functions of two semi-infinite (si) leads (see Fig. 2.5),

$$G_{QP}^{i,+} = G_{QQ}^{\text{si},+} \bar{V}^* (\mathbb{1} - G_{PP}^{\text{si},+} \bar{V} G_{QQ}^{\text{si},+} \bar{V}^*)^{-1} G_{PP}^{\text{si},+}. \quad (2.68)$$

With the help of the advanced (-) Green's function $G_{PP}^{\text{si},+} = [(G_{PP}^{\text{si},-})^*]^T$, the above equation can be written as,

$$G_{QP}^{i,+} = \underbrace{G_{QQ}^{\text{si},+} \bar{V}^*}_{A} (\mathbb{1} - G_{PP}^{\text{si},+} \bar{V} G_{QQ}^{\text{si},+} \bar{V}^*)^{-1} [(\bar{V}^{-1})^*]^T \underbrace{[(G_{PP}^{\text{si},-} \bar{V})^*]^T}_{B}. \quad (2.69)$$

In such a way we can identify in Eq. (2.69) the term A as the retarded solvent Z and the term B as the advanced solvent of Eq. (2.50). In these solvent matrices the transverse lead states χ_m appear in a way described by Eq. (2.51). Note that the Green's function $G^{\text{tot}} = G_{QP}^{i,+}$ obviously contains the same states χ_m as the ones it is projected on in Eq. (2.66). On closer inspection it can be verified that the operators \vec{D} and \vec{D}' in Eq. (2.66) always project the states χ_m which are implicitly contained in the Green's function G^{tot} onto the states χ_n which explicitly appear in Eq. (2.66). The action of these operators can therefore be evaluated conveniently by the orthonormalization condition in Eq. (2.67). Note that such an evaluation relies on the fact that the terms A and B appear on the very left and very right hand side of the expression in Eq. (2.69).

For an arbitrary scattering geometry with leads (see e.g. Fig. 2.1) the situation is quite similar to the above example of the infinite lead. This is because also in the general case the Green's function G^{tot} entering Eq. (2.66) will have the same structure as in Eq. (2.69),

$$G^{\text{tot}} = \underbrace{G_{QQ}^{\text{si},+} \bar{V}^*}_{A} \underbrace{\left(\dots \right)}_C \underbrace{[(G_{PP}^{\text{si},-} \bar{V})^*]^T}_{B}. \quad (2.70)$$

Only the middle term (C) will, of course, be different from Eq. (2.69), because it contains the specific information about the scattering geometry in between the leads. This difference does however not prevent an evaluation of Eq. (2.66) according to the procedure we introduced for the example of the infinite lead, since also here the solvent terms (A and B) appear conveniently one on each side of Eq. (2.70).

For the reflection amplitudes the procedure is somewhat more involved. Although the defining formula is identical to the one for the transmission amplitudes [60],

$$r_{nm}(E_F, B) = -\frac{i}{4\sqrt{\theta_n \theta_m}} \int_{-d/2}^{d/2} dy_2 \int_{-d/2}^{d/2} dy_1' \chi_n^*(y_2) e^{-ik_n x_2} (\vec{D} \cdot \hat{x}_2)^* G^{\text{tot}}(\mathbf{x}_2, \mathbf{x}_1', E_F, B) (\vec{D}' \cdot \hat{x}_1') \chi_m(y_1') e^{ik_m x_1'}, \quad (2.71)$$

it is more complicated to evaluate, since the variables \mathbf{x} and \mathbf{x}' are now both situated in the entrance lead. The two projections (i.e. derivatives) in Eq. (2.71) are therefore

not independent of each other. Translating this situation into the matrix notation of the discretized problem we find that the projections in Eq. (2.71) cannot be evaluated with the help of the orthogonalization condition (2.67) as conveniently as for the transmission amplitudes. This is because in the expression for r_{nm} the solvent terms A and B do not arrange as they did for t_{nm} . Going back to the example of the infinite lead, Fig. 2.5, we see that this dilemma occurs because the Green's function entering Eq. (2.71), $G^{\text{tot}} = G_{PP}^{i,+}$, consists of the following terms,

$$G_{PP}^{i,+} = \underbrace{G_{PP}^{\text{si},+}}_D + \underbrace{G_{PP}^{\text{si},+} \bar{V} (\mathbb{1} - G_{QQ}^{\text{si},+} \bar{V}^* G_{PP}^{\text{si},+} \bar{V})^{-1} G_{QQ}^{\text{si},+} \bar{V}^* [(\bar{V}^{-1})^*]^T}_{E} \underbrace{[(G_{PP}^{\text{si},-} \bar{V})^*]^T}_B. \quad (2.72)$$

Whereas the second term (E) again contains on its left and right hand side solvents (A and B) of Eq. (2.50), the first term (D) does not. This situation prevents us from employing the same procedure as for the evaluation of the transmission amplitudes. We tackle this problem by considering now the general case of an arbitrary scattering geometry with leads. For this general scenario the structure of the total Green's function G^{tot} entering Eq. (2.71) will be the same as in Eq. (2.72),

$$G^{\text{tot}} = \underbrace{G_{PP}^{\text{si},+}}_D + \underbrace{G_{PP}^{\text{si},+} \bar{V}}_A \underbrace{(\dots)}_F \underbrace{[(G_{PP}^{\text{si},-} \bar{V})^*]^T}_B, \quad (2.73)$$

again with the exception of the middle term F . We replace now the "problematic" term in Eq. (2.73), $G_{PP}^{\text{si},+}$, by the expression induced by Eq. (2.72). With this replacement Eq. (2.73) takes the form

$$G^{\text{tot}} = \underbrace{G_{PP}^{i,+}}_G - \underbrace{G_{PP}^{\text{si},+} \bar{V} (\mathbb{1} - G_{QQ}^{\text{si},+} \bar{V}^* G_{PP}^{\text{si},+} \bar{V})^{-1} G_{QQ}^{\text{si},+} \bar{V}^* [(\bar{V}^{-1})^*]^T}_E \underbrace{[(G_{PP}^{\text{si},-} \bar{V})^*]^T}_B + \underbrace{G_{PP}^{\text{si},+} \bar{V}}_A \underbrace{(\dots)}_F \underbrace{[(G_{PP}^{\text{si},-} \bar{V})^*]^T}_B. \quad (2.74)$$

In this form the projection of the Green's function G^{tot} in Eq. (2.71) can again be evaluated with the help of the orthogonalization condition (2.67) as conveniently as for the transmission amplitudes. This is because the first term (G) in Eq. (2.74) does not contribute to r_{nm} , since there is zero reflection in an infinite lead. Furthermore the projection of the second and third term ($E + H$) can be evaluated by the orthonormalization conditions Eq. (2.67) because in these terms the solvents A and B appear on the left and right hand side.

The resulting transport coefficients t_{mn} and r_{mn} can finally be checked numerically to form a unitary S matrix. The conductance through the scattering device is evaluated using the Landauer formula as in the field-free case [see Eqs. (2.9,2.10)].

2.8 Scattering wave functions

The scattering wavefunction $\psi(\mathbf{x})$ can be obtained at any point \mathbf{x} by projecting the retarded Green's function (by means of the operator $\vec{\mathbf{D}}$) on the incoming wave (in mode m) [22, 60],

$$\psi_m(\mathbf{x}) = -\frac{1}{2\sqrt{\theta_m}} \int_{-d/2}^{d/2} dy'_1 G^{\text{tot}}(\mathbf{x}, \mathbf{x}', E_F, B) (\vec{\mathbf{D}}' \cdot \hat{\mathbf{x}}'_1) \chi_m(y'_1) e^{ik_m x'_1}. \quad (2.75)$$

The term G^{tot} contains the solution of the Dyson equations for all modules linked. For the evaluation of the scattering wavefunction $\psi(\mathbf{x})$ the Green's function G^{tot} has to be evaluated at a large number of points \mathbf{x} throughout the entire scattering region. For a reasonably smooth wavefunction plot this number of points may be smaller than the entire number of gridpoints in the tb grid. However, the numerical effort for plotting the scattering wavefunction is still much higher than for the evaluation of the transport coefficients since the Green's function is then required only at the junctions between the modules. Nevertheless, also for wavefunctions plots the MRGM is more efficient than the standard RGM, as will be explained below.

2.9 Efficiency of the MRGM

The efficiency of the MRGM results from the following properties: First the number of recursions (i.e., of matrix inversions) needed to obtain the Green's function of the total scattering problem G^{tot} is given by the fixed number of modules required to build up the scattering structure. This number is independent of the de Broglie wavelength. The latter enters only in terms of the size of the matrices involved in the recursion since with increasing E_F (decreasing λ_D) more grid points are required to represent the continuum limit. By comparison, in the standard RGM the Green's function is calculated recursively at every new slice in propagating direction. This amounts to a large number of recursions, of the order of grid points in longitudinal direction $n_{\parallel} \gg 1$. Each of these recursions requires the inversion of a matrix, the size of which is determined by the number of grid points in transverse direction $n_{\perp} \gg 1$. Therefore, for high mode numbers and short wavelengths, a large number of gridpoints and of inversions are needed which renders the standard RGM eventually very time consuming. In the MRGM described above, the number of inversions is given by the number of modules needed to build the structure, independent of the wavelength. Moreover, the size of the matrices involved in joining the leads with the structure is modest, such that the number of inversions of large matrices e.g. in the case of the stadium is reduced to four. In the regular structures such as the circle, no inversion of large matrices is required at all.

One feature of the MRGM is particularly convenient for the calculation of the transport coefficients as a function of the Fermi wavenumber k_F (or Fermi energy E_F). These calculations are simplified by the fact that the solution of the eigenvalue problem ($|E_m\rangle, E_m$) entering the Green's function for each module [Eq. (2.27)] is independent of E_F . For the evaluation of the Green's function at different values

of E_F the eigenproblem $\hat{H}^{tb}|E_m\rangle = E_m|E_m\rangle$ therefore has to be solved only once. Unfortunately, this feature does not extend to the variation of the magnetic field since both $|E_m\rangle$ and E_m are dependent on B . Because of this property a new solution of the tb eigenproblem is required for each value of the field. The most severe restriction of the MRGM is, however, that its applicability is limited to those scattering structures which can be assembled from or cut out of separable modules. Also random potentials and soft walls can only be included as long as they preserve the separability of each module. We mention at this point, that a "hybrid RGM" for dealing with arbitrary boundary geometries was presented in the literature [22]. Finally we remark that with the MRGM changes in position and direction of the leads can be done without any major effort.

Chapter 3

Numerical results for high magnetic fields and high energies

In this chapter we present first magnetoconductance results which were calculated within the MRGM at high magnetic fields B and large Fermi wavenumbers k_F . As prototype cavity geometries we use the circular and stadium shaped quantum dots depicted in Fig. 2.1 and consider different geometries for the attached quantum wires.

3.1 Accuracy checks

Several checks for the accuracy of the numerical results have been performed. Exact relationships for transport coefficients such as conservation of unitarity and the Onsager relations are fulfilled with an accuracy of better than 10^{-10} . The grid density is chosen such that the magnetic flux per unit cell is $B\Delta_R/c < 0.01$ (as in Ref. [61]). Moreover, the typical number of grid points per Fermi half-wavelength is greater than 30. Only for very high energies (Fig. 3.2) the relative grid density is lower. For low magnetic fields, we can compare our results for $|t_{nm}(k_F)|^2$ with previous methods. As an example we show in Fig. 3.1 a comparison for $|t_{11}(k_F)|^2$ with the calculation by Yang *et al.* [13], which is based on a wave function expansion in spherical waves. The agreement for the circle is very good although diamagnetic terms are neglected in the approach of Ref. [13]. For the stadium, the differences between the two methods are somewhat larger. This is due to the fact that the expansion of the stadium wave functions in spherical waves leads to a unitarity deficiency (see Fig. 3.1). We can also reproduce previous results of Ref. [13] concerning statistical magnetoconductance properties in chaotic and regular cavities. These will not be treated again. Our focus will be on the high magnetic field and high energy regime where other methods failed.

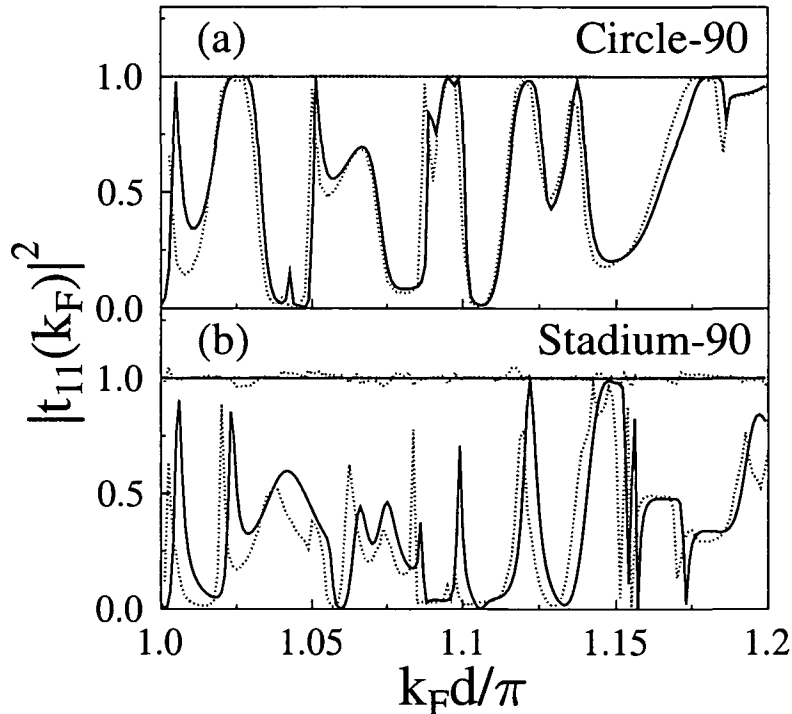


Figure 3.1: Comparison between the present MRGM (solid line) and the wavefunction matching technique [13] (dotted line) for the first-mode transmission probability $|t_{11}(k_F)|^2$ at $B/c = 1$ in a small window of k_F : (a) circle with perpendicular leads, (b) stadium with perpendicular leads ($d = 0.35$, $A^{\text{dot}} = 4 + \pi$). In both cases also $|t_{11}(k_F)|^2 + |r_{11}(k_F)|^2$ is shown. Contrary to the MRGM (solid line), the wave function matching technique (dotted line) deviates from the unitarity limit in (b).

3.2 Wavefunctions

The starting point for the analysis of the scattering states $\psi(\mathbf{x})$ for ballistic transport through quantum dots is Eq. (2.75). Figures 3.2 and 3.3 display the resulting electron density $\propto |\psi(\mathbf{r})|^2$ in the scattering region. In Fig. 3.2 we consider the wavefunctions at very high k_F for both the circle and the stadium billiards which are prototypical structures for regular and chaotic dynamics respectively. Large k_F corresponds to the regime where the convergence towards classical scattering trajectories is expected to emerge. Figures 3.2a and 3.2b illustrate the different dynamics for an injection at high ($m = 20$) and at low mode numbers ($m = 1$), respectively. Since high mode numbers correspond classically to a large injection angle, the wavefunction condenses around a pentagon-shaped whispering gallery trajectory. For low-mode injection, a small circle representing the centrifugal barrier (or caustic) is seen, as well as rays representing the asterisk orbits [62]. Figures 3.2c-h display scattering states for the stadium [63, 64]. At low magnetic fields, the dynamics is chaotic and a typical wavefunction features a quasi-random pattern with a modest density enhancement near classically unstable periodic orbits (see Figs. 3.2g-h). For special

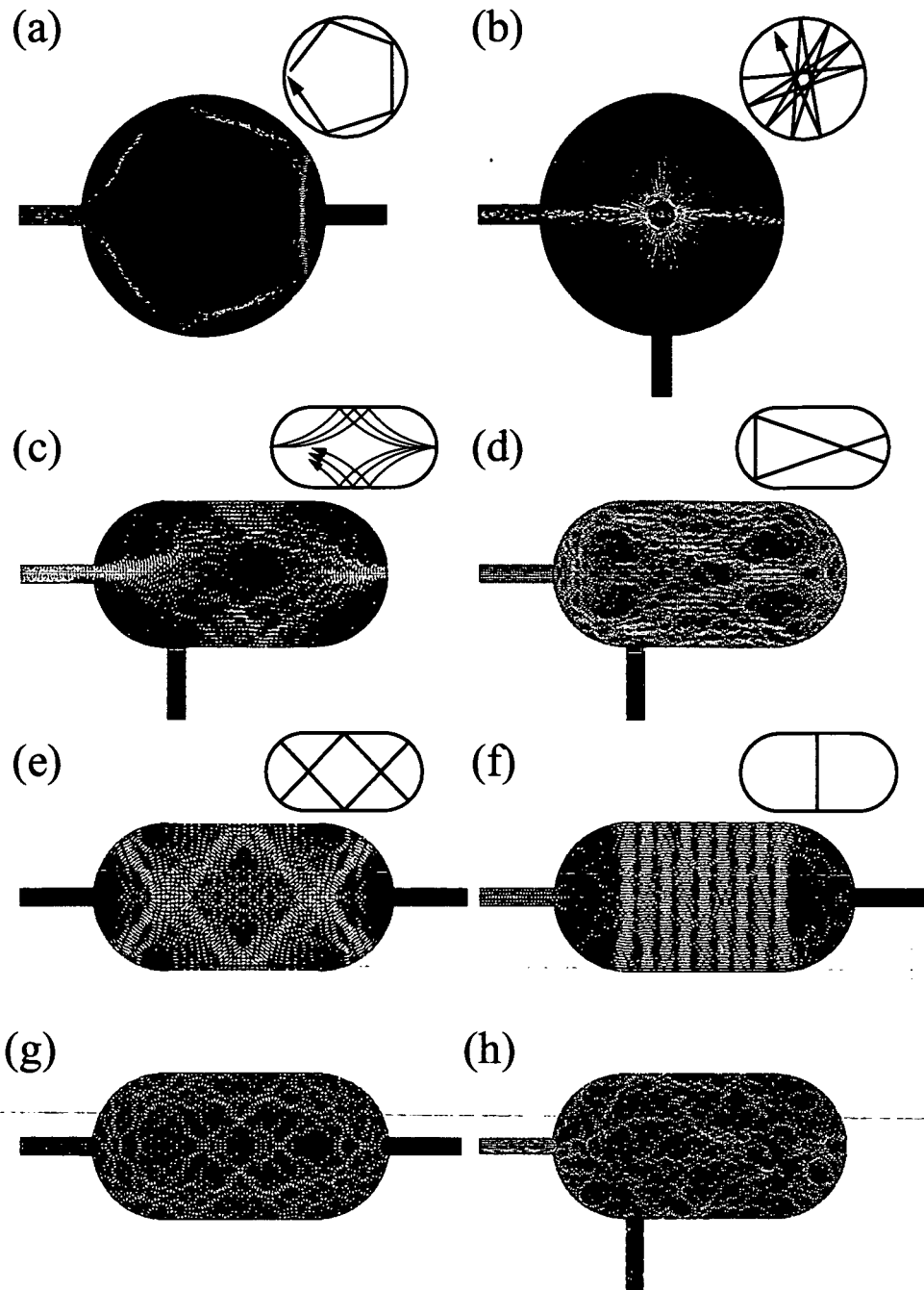


Figure 3.2: Absolute square of the scattering wave functions $|\psi(x, y)|^2$ at high k_F [(a): $k_F = 25\pi/d$, (b): $k_F = 12.5\pi/d$, (c), (e): $k_F = 6.01\pi/d$, (d): $k_F = 8.44\pi/d$, (f): $k_F = 4.46\pi/d$, (g): $k_F = 6.53\pi/d$, (h): $k_F = 8.28\pi/d$]. The four quantum dots considered above are the circle and stadium [64] with relative lead orientation of 90° and 180° , area $A^{\text{dot}} = 4 + \pi$, and lead width $d = 0.25$. In (a)-(f) the localization around classical trajectories is clearly visible (see insets for comparison). In the cases of (d)-(f), the wavefunction localizes around unstable periodic orbits ("scars"). Note the surprising fact that in contrast to the cases (a)-(c), these orbits are classically decoupled from the leads. The magnetic field is zero in all displayed figures, with the only exception of (c), where the field $B/c = 30.5$ allows for a whole bundle of equivalent trajectories with cyclotron radius $r_c = k_F c/B \approx 2.48$ to contribute to transport.

configurations of k_F and B “scars” emerge in the scattering wavefunctions (Fig. 3.2d-f). By contrast, for high magnetic fields the classical motion in the stadium becomes regular. In the present example (Fig. 3.2c) the wavefunction condenses around a “bundle” of cyclotron orbits executing three bounces at the cavity wall before exiting by the entrance lead. There has been an extensive discussion in the literature as to the existence of scars in open quantum billiards [21, 65, 66]. Our present results clearly underscore that scars, defined as the condensation of the wavefunction near classical unstable trajectories, clearly exist for large k_F .

At high fields and low values of k_F , the formation of “edge states” can be observed (see Fig. 3.3). These states correspond to the classical “skipping orbits”, which are restricted to a region very close to the boundary. With increasing B fewer edge states can be excited in the cavity. In Fig. 3.3c ($B = 68.5$) three transverse edge states are present while in Fig. 3.3d ($B = 125$) only a single edge state remains [64]. For two edge states carrying flux across the quantum dot, interferences give rise to a stationary nodal pattern with a fixed number of antinodes along the boundary (see

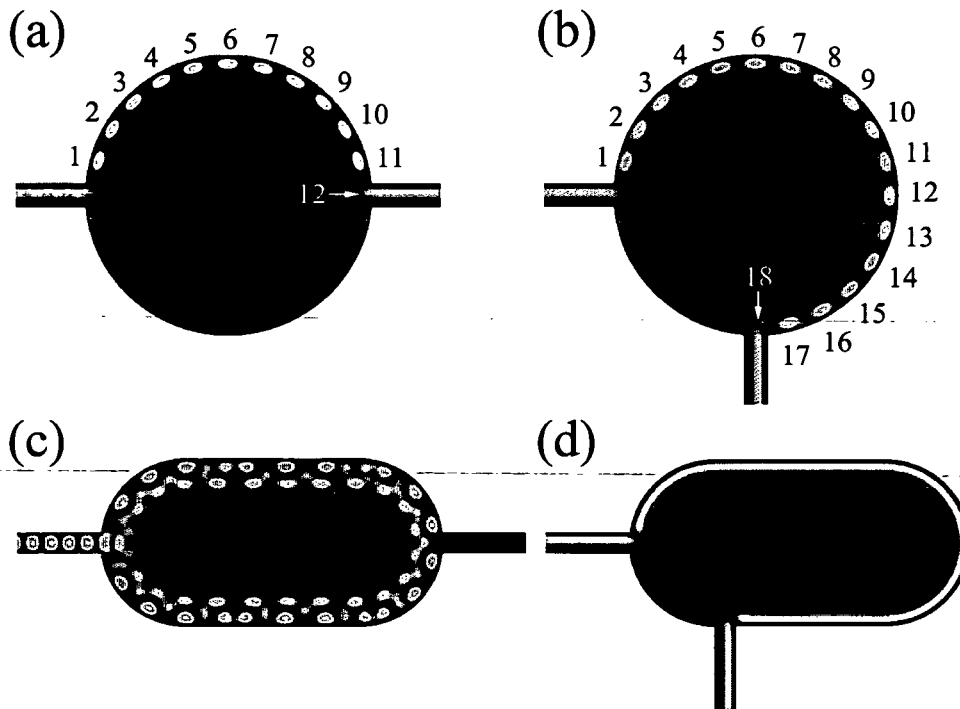


Figure 3.3: Absolute square of the scattering wave functions $|\psi(x, y)|^2$ in the edge state regime. The area of all geometries $A^{\text{dot}} = 4 + \pi$, lead width $d = 0.25$, and $k_F = 1.5\pi/d$. The four plots correspond to the points in the transmission spectra (Fig. 4.2), indicated by the letters (a)-(d). The numbers along the longitudinal direction of the edge states count the number of antinodes between entrance and exit lead (see corresponding numbers in Fig. 4.2). Note that edge states at different magnetic fields have up to n transverse nodes: (a) circle, 180° , $n = 2$, (b) circle, 90° , $n = 2$, (c) stadium, 180° , $n = 3$, and (d) stadium, 90° , $n = 1$.

Fig. 3.3a,b). We are not aware of any other method that has so far been capable of investigating scattering states of open structures in this high-magnetic field regime.

Part II
Applications

Chapter 4

Oscillations and resonances in transmission

In this chapter we investigate the specific signatures imprinted on the transport coefficients by the scattering process. A special focus will be put on the high energy and high magnetic field regime, where regular oscillations and resonances appear in the transmission/reflection as a function of the Fermi wavenumber k_F and the magnetic field B .

4.1 Transport at high energies

When exploring the high energy domain of transport through quantum dots, we observe a transition of the quantum mechanical dynamics towards the classical picture of electron motion. Classically the trajectories of the electron follow circle arcs with a cyclotron radius $r_c = ck_F/B$. With increasing energy not only a transition towards these trajectories is expected, but also the diffraction patterns of the electron at the two lead mouths converge towards the classical injection angles [67]. Both effects eventually lead to a localization of the scattering wave function around classical bouncing orbits. The “classical injection” of electrons can also give rise to a comparatively low number of topologically different semiclassical bouncing orbits that contribute to transport. Moreover, if only a few types of trajectories interfere at the lead mouths, also the transmission (reflection) amplitudes will be determined by a few-path rather than by a multi-path interference. For special configurations, where only two to three different trajectories are involved in the transport process, periodic transmission patterns will therefore arise. However, as a precondition for this behaviour to appear in a certain range of k_F (or B), the specific bouncing pattern of the contributing trajectories has to stay the same throughout this entire range. This stability requirement makes systems with regular classical dynamics more inclined to show periodic transmission fluctuations at high energies than chaotic systems. Note however that also classical systems which are fully chaotic for zero magnetic field can acquire regular components for non-zero field [68].

In Fig. 4.1a we show a part of a typical spectrum of the transmission amplitude

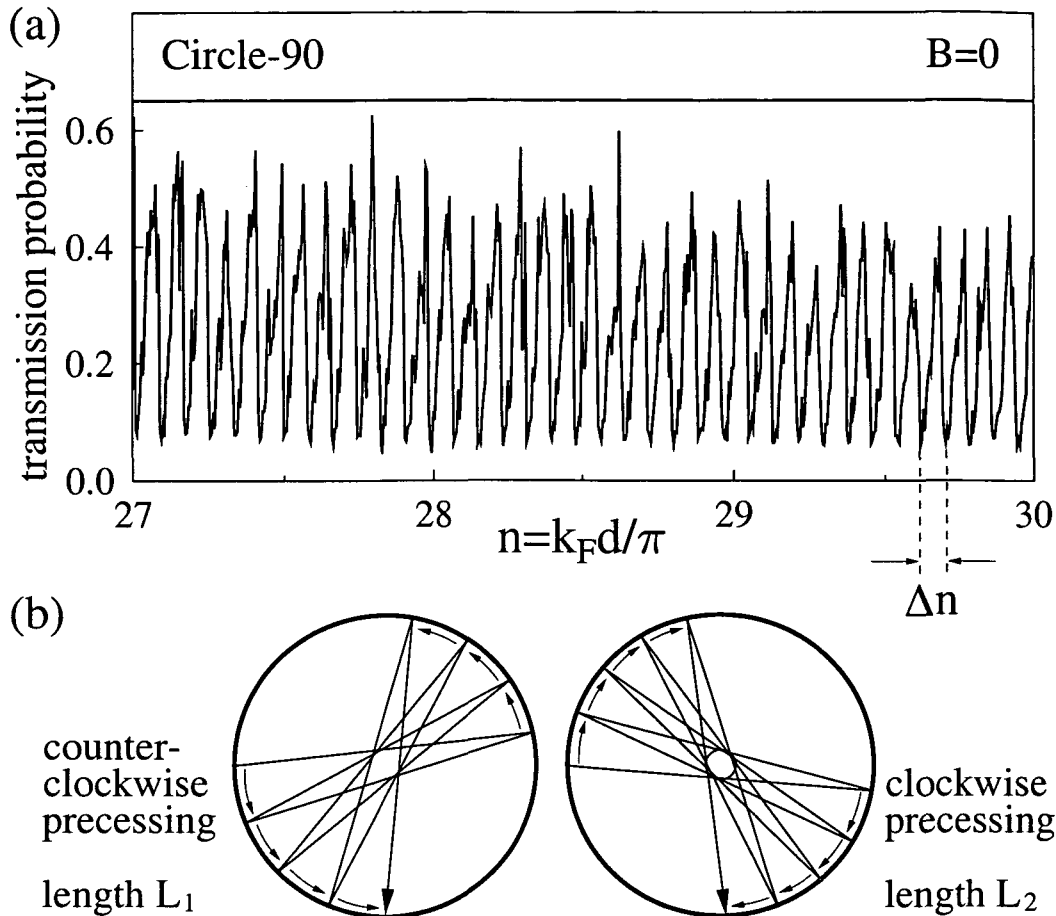


Figure 4.1: (a) First mode transmission probability $\sum_{m=1}^{29} |t_{m,1}(n)|^2$ for transport through the circular dot with 90° lead orientation. In the semiclassical regime shown here ($27 < n < 30$) regular patterns with period Δn appear in the data and can be explained by the interference of the trajectories in (b). The constant length difference $\Delta L = L_2 - L_1$ is related to Δn and the lead width d by the relation $\Delta n = d / \Delta L$.

$|t_{11}(k_F)|^2$ for the circle with 90° lead orientation. Periodic patterns as a function of k_F are clearly visible. The corresponding scattering wave function which is repeatedly reappearing around every maximum of this pattern is always similar to the wavefunction shown in Fig. 3.2b. We note that the period in the oscillations of the transmission probability (Δk_F) corresponds very well to the difference in path lengths ($\Delta L = L_2 - L_1$) between the two contributing trajectories depicted in Fig. 4.1b, $\Delta k_F = \pi / \Delta L$.

A particularly advantageous property of these oscillations is the fact that they indicate in which range of k_F (or B) the scattering wave function is well localized. This is because both the oscillations and the localization phenomena are often only visible when the number of trajectories participating in the transport process is very low. Since MRGM calculations for transport coefficients are faster than for wavefunctions, this feature allows to scan different parameter intervals for an oscillatory

behaviour and to pin down localization effects by plotting the wavefunctions at those parameter configurations where oscillations appear.

4.2 Transport at high magnetic fields

Also in the high magnetic field regime characteristic oscillations are observable, which are caused by an interference between different edge states. Figure 4.2 shows the high magnetic field regime of the transmission probability in the first mode $m = n = 1$ for both circle and stadium. Different orientations of the exiting quantum wire were chosen (oriented 90° and 180° relative to the incoming lead). A few universal trends are easily discernible: above a certain critical value of the magnetic field (denoted by B_c^1), the strongly fluctuating transmission probability gives way to very regular oscillations in all four cases [see insets of Fig. 4.2 for magnification]. The threshold value B_c^1 and the magnetic field, at which transport is terminated (separately displayed in Fig. 4.3) are identical for all systems investigated. Below B_c^1 the transport signal displays “beats”, i.e. the Fourier transform of the signal is characterized by several frequencies. The “universality” (i.e. geometry independence) of these features is related to the fact that in the high magnetic field regime transport is controlled by edge states (as depicted in Fig. 3.3). These states play a very prominent role in the Quantum Hall effect and have been studied extensively [6, 18, 69–71]. At magnetic fields, where the magnetic length is smaller than the system dimensions, $l_B \ll D$, they are the only states coupling to the quantum wire since bulk Landau states cannot be accessed through the leads. The edge states shown in Figs. 3.3a to 3.3d correspond to the points in the transmission spectrum also labeled by (a) to (d) in Fig. 4.2. By comparison with the scattering wavefunctions (as in Fig. 3.3), we observe that in the magnetic field region $B_c^n < B < B_c^{n-1}$ edge states have up to $n - 1$ transverse nodes in the direction perpendicular to the boundary. Furthermore, the number of longitudinal antinodes from entrance to exit lead (see the corresponding numbers in Fig. 3.3a,b) can be directly mapped onto successive maxima in Fig. 4.2 (see numbers there). The range of B depicted in Fig. 4.2 corresponds to $B \gtrsim B_c^2$ at $k_F = 1.5\pi/d$. The transmission spectrum becomes increasingly complex as B is reduced or equivalently k_F is increased (not shown).

To determine the positions of the values B_c^n we consider the energy shift of Landau levels near the boundary. Bulk Landau levels are degenerate since their quantized energy $E_n = (n + 1/2)B/c$ is independent of their position in space. This degeneracy is lifted if a Landau state is placed in the vicinity of the cavity wall: with decreasing distance to this boundary the energy of the state increases. Therefore the energies of edge states associated with the quantum number n lie above the asymptotic bulk value E_n . When the incoming electron is diffracted at the mouth of the entrance lead, only those edge states whose energy is below the Fermi energy can carry flux. Due to the sharp edges at the junction between lead and quantum dot, all energetically accessible edge channels are populated. The magnification of the scattering wavefunction near the lead mouth (Fig. 4.4) highlights the diffractive edge scattering. This is in contrast to smooth edges where states in the lead could

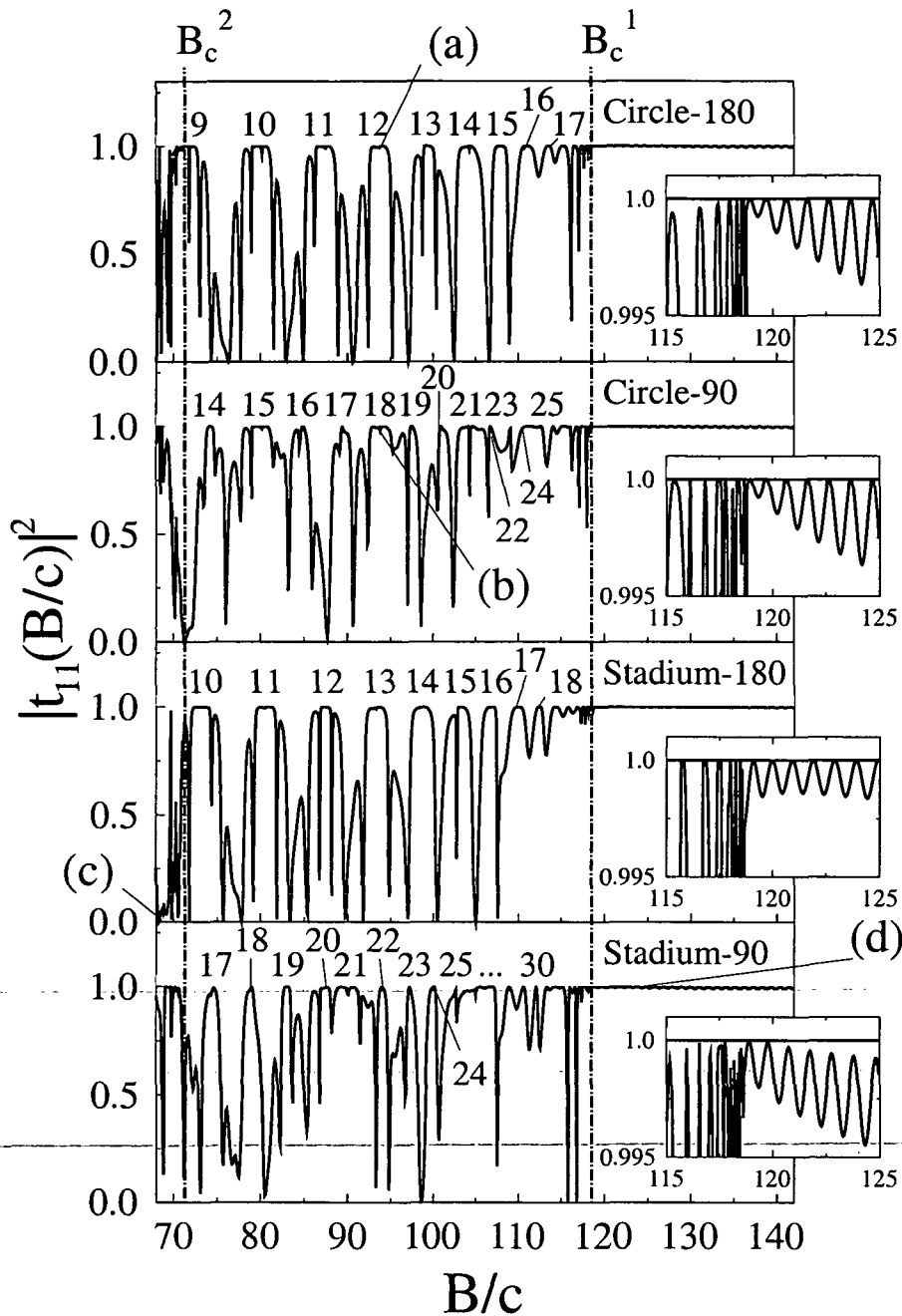


Figure 4.2: Transmission probabilities $|t_{11}(B/c)|^2$ in the high magnetic field limit for circle and stadium billiard with 180° or 90° lead orientation. ($k_F = 1.5\pi/d$, $d = 0.25$). B_c^2 and B_c^1 are the threshold magnetic fields $B_c^n/c = k_F^2/(2n+1)$ (vertical dash-dotted lines). Above B_c^1 regular oscillations appear (see insets for magnification). For $B_c^2 < B < B_c^1$ irregular fluctuations set in. Their large-scale structure can be explained by the number of interference maxima the two edge states form along the boundary between entrance and exit lead (see indicated numbers). The points (a)-(d) correspond to the wavefunctions shown in sections (a)-(d) of Fig. 3.3.

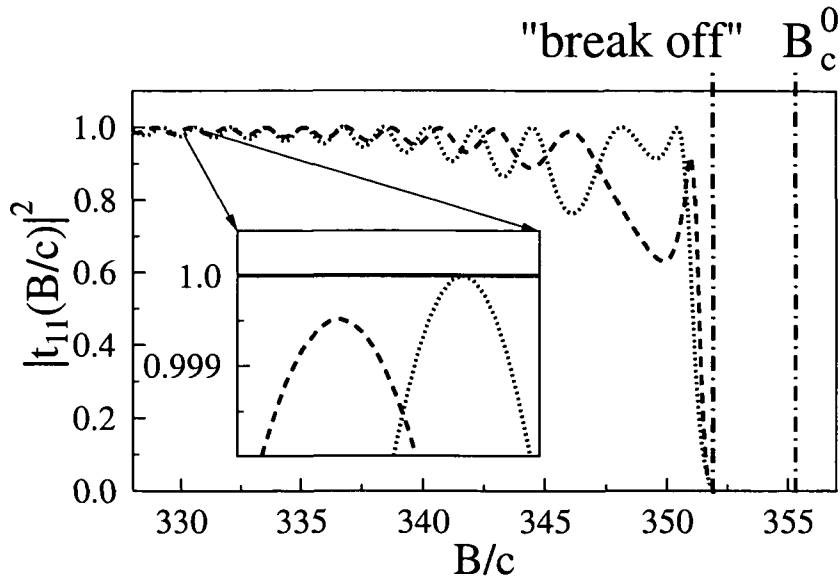


Figure 4.3: Transmission probabilities $|t_{11}(B/c)|^2$ in the high-field limit, near the point where transport terminates. The dashed line stands for the stadium billiard (90° lead geometry) and the dotted line for the circle (we show the case of 90° and 180° lead orientation which give rise to identical transmission probabilities). The two dash-dotted vertical lines mark the point where transport breaks off and the analytically determined threshold value $B_c^0 \approx 355.3$ (see text for details). The inset shows that the transmission probabilities for the circle reach the maximum value 1 which is only approximately true for the stadium with 90° -lead geometry.

cross the lead junction adiabatically, i.e. without changing their state of quantization [72]. With sharp lead junctions however all edge states with quantum number $n' \leq n$ will participate in transport up to a magnetic field where E_n touches the Fermi energy, $E_n = E_F$, i.e. at the critical magnetic fields $B_c^n/c = E_F/(n + 1/2)$. These threshold values are indicated by the dot-dashed vertical bars in Figs. 4.2 and 4.3 for $B_c^2 \approx 71.1$, $B_c^1 \approx 118.4$ and $B_c^0 \approx 355.3$ for a lead width $d = 0.25$ and $k_F = 1.5\pi/d$. In our numerical data, both the position of these threshold values as well as their independence of the geometry are in excellent agreement with this prediction. The only exception is the critical magnetic field B_c^0 . Its value (355.3) lies slightly above the point where the transmission spectrum ceases (at $B \approx 351.8$) (see Fig. 4.3). The reason for this deviation is the fact that the termination point of the spectrum is not determined by the magnetic field of the lowest bulk Landau level in the cavity (i.e. B_c^0), but by the highest field at which the leads still carry flux. In the leads, however, the magnetic length does not satisfy the condition $l_B \ll d$ (at $k_F = 1.5\pi/d$: $l_B \approx d/4.7$). Contrary to the cavity, the wavefunctions still “feel” the constriction by the opposing wall in the lead. For this reason, the threshold magnetic field values of the transverse lead states lie slightly below those of the bulk Landau levels, leading to a termination already below B_c^0 .

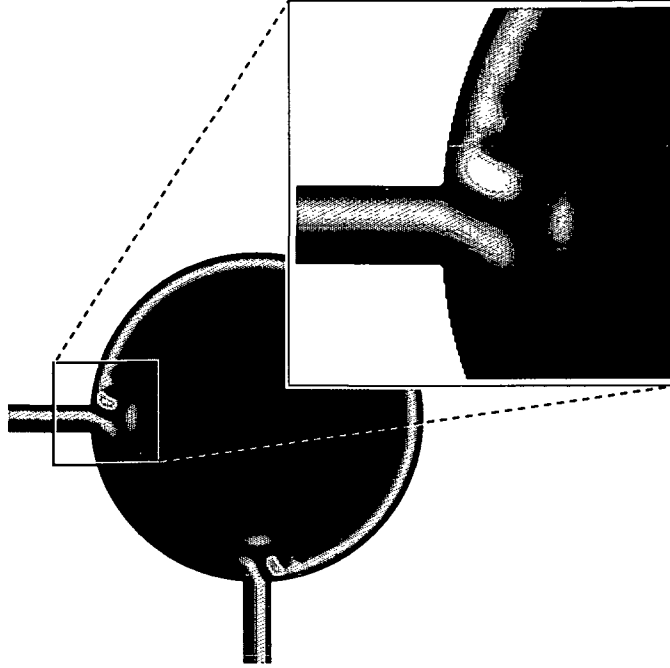


Figure 4.4: *Electron density $|\psi(x, y)|^2$ for the circle billiard with diffractive scattering highlighted. ($A^{\text{dot}} = 4 + \pi$, lead width $d = 0.25$ and $k_F = 1.5\pi/d$.) The magnetic field $B = 118.7$ is just above the threshold to the single-edge state regime $B_c^1 = 118.44$.*

4.3 Multi-channel interferences

The regular oscillations above B_c^1 as well as the complex fluctuating pattern below B_c^1 can be explained by a multi-channel scattering description. This model can be viewed as a generalization [39, 40, 73, 74] of a single-channel picture [69, 75, 76]. For this description to be applicable, the cavity of the dot has to have smooth boundaries and disorder must be absent. Under these circumstances the flux transported by edge states is conserved in the interior and changed only by diffractive scattering at lead junctions: A fraction of the flux will exit through the lead while the remaining portion of the flux will continue to propagate along the boundary. The stationary scattering state can be viewed as a coherent superposition of wavepackets repeatedly encircling the billiard. In order to translate this picture into an analytic expression we define amplitudes for transmission and reflection at the two lead junctions. We denote the amplitudes for transmission from transverse mode m in the entrance lead to the edge state in the dot with quantum number i by \tilde{t}_{mi} . The amplitudes \tilde{t}'_{in} stand for transmission from edge state i in the dot to the transverse mode n in the exit lead. The amplitudes \tilde{r}_{ij} (\tilde{r}'_{ij}) describe edge state reflection at the entrance (exit) lead from mode i to mode j . (The tilde signs serve to distinguish these amplitudes from the transport coefficients for the whole geometry t_{nm} and r_{nm} .) We further

define the following matrices

$$[\tilde{T}]_{ij} = \tilde{t}_{ij} e^{ik_j L_j - iBA_j/c}, \quad [\tilde{T}']_{ij} = \tilde{t}'_{ij} \quad (4.1)$$

$$[\tilde{R}]_{ij} = \tilde{r}'_{ij} e^{ik_j L'_j - iBA'_j/c}, \quad [\tilde{R}']_{ij} = \tilde{r}_{ij} e^{ik_j L_j - iBA_j/c}, \quad (4.2)$$

where L_j, A_j (L'_j, A'_j) denote the lengths L and areas A the edge state j covers from entrance to exit (from exit to entrance) of the dot. The areas A can be determined in gauge-invariant form although the corresponding classical orbits are not necessarily closed [77]. The transmission through the whole cavity $t_{ji} = [T]_{ij}$ is then written as a geometric series of matrices,

$$\begin{aligned} T &= \tilde{T}(1 + \tilde{R}'\tilde{R}(1 + \tilde{R}'\tilde{R}(1 + \dots)))\tilde{T}' \\ &= \tilde{T} \left(\sum_{i=0}^{\infty} (\tilde{R}'\tilde{R})^i \right) \tilde{T}' \\ &= \tilde{T}(1 - \tilde{R}'\tilde{R})^{-1}\tilde{T}'. \end{aligned} \quad (4.3)$$

Equation (4.3) serves as a convenient starting point for the analysis of the transmission fluctuations. Consider first the regime $B > B_c^1$, where only the lowest transverse edge state is excited. In this case Eq. (4.3) reduces to its scalar version [69, 75, 76]

$$T^{\text{tot}} = |t_{11}|^2 = \frac{|\tilde{t}_{11}|^2 |\tilde{t}'_{11}|^2}{1 - 2 \text{Re}[\tilde{r}'_{11} \tilde{r}_{11} e^{i\gamma}] + |\tilde{r}'_{11}|^2 |\tilde{r}_{11}|^2}, \quad (4.4)$$

with $\gamma = k_1(L_1 + L'_1) - B(A_1 + A'_1)/c$. As expected, the fluctuations of $|t_{11}(B/c)|^2$ are determined by an Aharonov-Bohm type phase γ [9]. At fixed k_F , the oscillation period is $\Delta B = 2\pi c/A_1^{\text{tot}}$. By $A_1^{\text{tot}} \equiv A_1 + A'_1$ we denote the area which the edge state acquires in one revolution around the dot. Taking into account that the dynamically accessible area of the edge state is somewhat smaller than the geometric area, $A_1^{\text{tot}} < A^{\text{dot}} = 4 + \pi$ (see Fig. 3.3), the prediction for the oscillation period is in excellent agreement with our numerical findings. Equation (4.4) also explains why the oscillation period is increasing with increasing B (see Fig. 4.3). This explanation makes use of the fact, that for increasing magnetic field skipping orbits with *fixed quantum number* n have an *increasing* mean distance from the boundary [76]. Note, however, that the distance of edge states from the boundary increases with the quantum number n . Since higher n die out earlier for increasing magnetic field, the overall effect shows the anticipated *decreasing* mean distance from the boundary for increasing magnetic field. However, for *fixed quantum number* n a larger B field implies a smaller enclosed area A_1^{tot} and therefore a higher oscillation period ΔB . Furthermore Eq. (4.4) accounts for the fact that for most structures the successive maxima of T^{tot} reach unity [75]. (The small deviation from this rule of the stadium with 90° lead orientation will be explained below). In addition to unitarity, $[|\tilde{t}'_{11}|^2 + |\tilde{r}'_{11}|^2 = 1]$ we have for identical lead junctions $\tilde{r}_{11} = \tilde{r}'_{11}$. (We call two junctions *identical* if the local environment of their lead mouths is the same and their respective distance is larger than a few wavelenghts.) Above B_c^1 scattering of an edge state at a junction is essentially a one-dimensional process, for which the probability

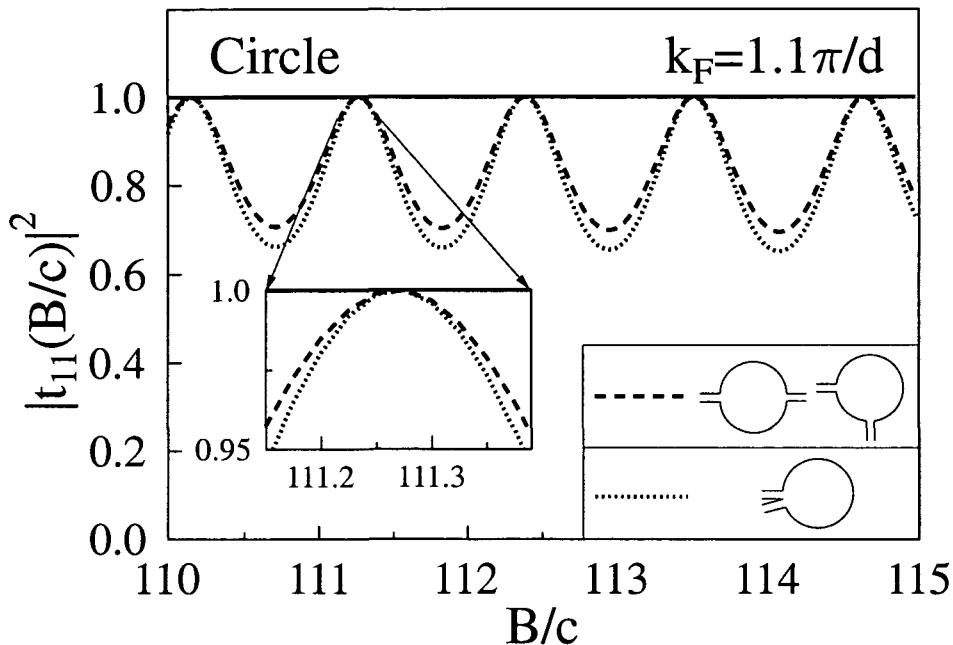


Figure 4.5: Transmission probability $|t_{11}(B/c)|^2$ at $k_F = 1.1\pi/d$ for transport through the circular billiard in the single-edge channel regime, $B > B_c^1$. As long as the entrance and exit lead mouths have a mutual distance of more than a few wavelengths, $|t_{11}|^2$ stays invariant with respect to rotations of the leads around the circle boundary (see dashed line for 90° and 180° lead orientation). Only when the leads are close to each other (dotted line) $|t_{11}|^2$ changes significantly. The maxima of the oscillations remain invariant (see inset for magnification).

for transmission from left to right has the same magnitude as vice versa. Identical lead junctions therefore also imply $\tilde{t}_{11} = t_{11}$, provided that the two corners of the lead junction have the same shape. If and only if all of the three above conditions are fulfilled, Eq. (4.4) yields $T^{\text{tot}} = 1$ at the resonance condition $\gamma = 2\pi n, n \in \mathbb{Z}$. Since for the two circle geometries and for the 180° -stadium the two lead junctions are identical, we indeed find in these cases that $|t_{11}(B)|^2$ periodically reaches unity. On the other hand, when the leads are attached to the stadium at an angle of 90° , one lead is attached to the straight section while the other is attached to the semi-circle. The local environment of the two lead mouths is in this case different (i.e. the lead junctions are not *identical*), for which reason our numerical results do not quite reach $|t_{11}|^2 = 1$, when the resonance condition is fulfilled for this geometry (see inset of Fig. 4.2d and Fig. 4.3).

One interesting feature of the transmission fluctuations in the single-channel regime of the circular dot ($B > B_c^1$) is their invariance with respect to the lead orientation (see Fig. 4.5). The numerical results for the transmission probabilities of the circle with 180° and 90° lead orientation differ only at the tenth decimal digit (!). This fact, as well as the observation that in the case of the stadium billiard the two lead orientations give different results, can again be explained by Eq. (4.4). The important point to note is that the interference phase ($\gamma = k_1 L_1^{\text{tot}} - BA_1^{\text{tot}}/c$) does

not change when changing the positions of the leads around the circle. Due to the rotational symmetry also the coefficients \tilde{t}_{11} , \tilde{t}'_{11} , \tilde{r}_{11} and \tilde{r}'_{11} are the same for different angles between the leads. The same is thus true for the total transmission T^{tot} through the circular dot. The only exception to this rule occurs when the two leads are in close proximity to each other of only a few wavelengths. In this case the transmission probability changes as compared to the results for the 180° and 90° lead orientation. However, due to the mirror symmetry of the two lead junctions, the maxima of the oscillations stay unchanged in position and height ($|t_{11}|_{\text{max}}^2 = 1$), even when the leads are placed very close to each other (see Fig. 4.5).

The fluctuations in the regime $B < B_c^1$ displayed in Fig. 4.2 can be analyzed with the help of a multi-channel scattering description. In the interval $B_c^2 \leq B \leq B_c^1$ two channels corresponding to two edge states are open in the cavity and one channel in each of the leads. From the entrance to the exit lead mouth the two edge channels acquire the phases $e^{ik_1 L_1 - iBA_1/c}$ and $e^{ik_2 L_2 - iBA_2/c}$ respectively. At fixed k_F , their interference at the exit lead will therefore give an oscillatory contribution to the total transmission $T^{\text{tot}}(B) = |t_{11}|^2$ of the form

$$T^{\text{tot}}(B) \propto \cos^2[B(A_1 - A_2)/(2c)]. \quad (4.5)$$

For closer analysis we need to evaluate Eq. (4.3) which involves the inversion of 2×2 matrices. In the case of parallel lead orientation the corresponding expressions are simplified due to the fact that the phases acquired from entrance to exit lead and vice versa are the same ($A_n = A'_n$ and $L_n = L'_n$), leading to

$$\begin{aligned} t_{11} = & \left[e^{i\varphi_1} \tilde{t}_{11} \tilde{t}'_{11} + e^{i\varphi_2} \tilde{t}_{12} \tilde{t}'_{21} + e^{i(2\varphi_1 + \varphi_2)} (\tilde{r}_{11} \tilde{t}_{12} - \tilde{r}_{12} \tilde{t}_{11}) (\tilde{r}'_{21} \tilde{t}'_{11} - \tilde{r}'_{11} \tilde{t}'_{21}) \right. \\ & + e^{i(\varphi_1 + 2\varphi_2)} (\tilde{r}_{21} \tilde{t}_{12} - \tilde{r}_{22} \tilde{t}_{11}) (\tilde{r}'_{22} \tilde{t}'_{11} - \tilde{r}'_{12} \tilde{t}'_{21}) \left. \right] / \left[1 - e^{i2\varphi_1} \tilde{r}_{11} \tilde{r}'_{11} - e^{i2\varphi_2} \tilde{r}_{22} \tilde{r}'_{22} \right. \\ & \left. - e^{i(\varphi_1 + \varphi_2)} (\tilde{r}_{21} \tilde{r}'_{12} + \tilde{r}_{12} \tilde{r}'_{21}) - e^{i2(\varphi_1 + \varphi_2)} (\tilde{r}_{11} \tilde{r}_{22} - \tilde{r}_{12} \tilde{r}_{21}) (\tilde{r}'_{12} \tilde{r}'_{21} - \tilde{r}'_{11} \tilde{r}'_{22}) \right]; \end{aligned} \quad (4.6)$$

with the abbreviated notation $\varphi_n = k_n L_n - BA_n/c$. In Fig. 4.6 we show one half-period of the beats in $T^{\text{tot}}(B) = |t_{11}(B)|^2$ for $[\pi n < B(A_1 - A_2)/(2c) < \pi(n + 1)]$, as calculated with Eq. (4.6). The absolute square of the numerator (dashed line, N) and denominator (dotted line D) of Eq. (4.6) display very similar oscillations, both in frequency and amplitude. However, since $T^{\text{tot}} = N/D$, a series of dips are superimposed on the term $\cos^2[B(A_1 - A_2)/(2c)]$ at the points where N and D have their common minima. To classify these dips (i.e. antiresonances) we make use of the fact [39, 40, 73] that the unitarity of Eq. (4.6) allows the mapping of the transport coefficients at the lead junctions (which are assumed to be identical) onto six independent parameters: the four phases ($\phi, \vartheta, \phi_1, \phi_2$) and the two moduli (s, p) with absolute values $|s|, |p|$ restricted to the interval $[0, 1]$. The latter two parameters are (1) the modulus, s , of the reflection amplitude of the wave incoming in mode 1 and reflected into mode 1 at the entrance lead junction,

$$\tilde{r}''_{11} = s e^{i(\psi + \vartheta)}, \quad (4.7)$$

and (2) the modulus, p , of the partial injection amplitude of the incoming wave into the lowest edge state in the cavity, corrected for the partially reflected flux,

$$\tilde{t}_{11} = \tilde{t}'_{11} = p \sqrt{(1 - s^2)} e^{i[(\phi_1 + \psi)/2 + \vartheta]}. \quad (4.8)$$

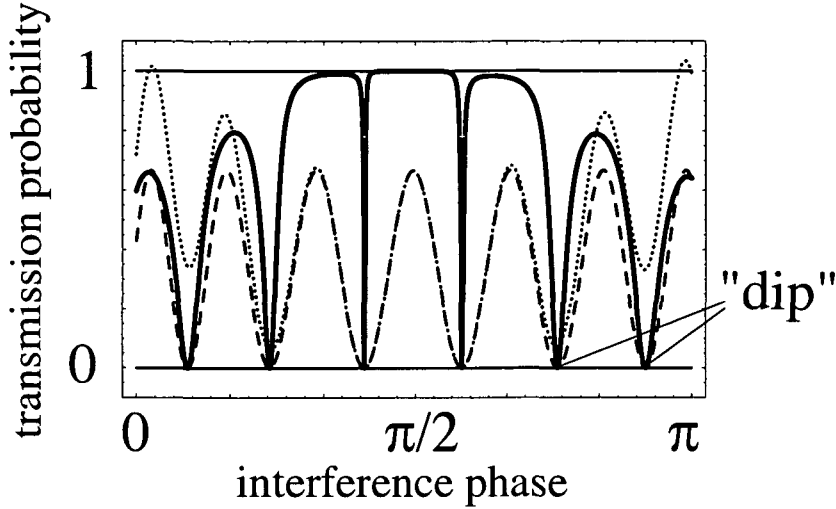


Figure 4.6: One half-period of the beating $\pi n < B(A_1 - A_2)/(2c) < \pi(n + 1)$ in the transmission probability $|t_{11}(B/c)|^2$ (solid line), as calculated with our interference model [see Eq. (4.11)]. The numerator (dashed line, N) and denominator (dotted line, D) of $|t_{11}(B/c)|^2$ show very similar oscillations (with a small offset). (N/D) features sharp “dips”, at the points where N and D have their common minima. These dips are window resonances (also called Breit-Wigner antiresonances) and represent a symmetric limit of the Fano resonance lineshape. See text for details.

Because of the symmetries of the set-up, the injection (ejection) amplitude at the entrance (exit) lead junction are equal. Accordingly, the injection amplitude into the second edge state in the cavity is given by

$$\tilde{t}_{12} = \tilde{t}'_{21} = \sqrt{(1-s^2)(1-p^2)} e^{i[(\phi_2+\psi)/2+\vartheta]}. \quad (4.9)$$

Analogous expressions can be deduced for the other partial amplitudes entering Eq. (4.6),

$$\begin{aligned} \tilde{r}_{11} &= \tilde{r}'_{11} = -[(1-p^2) + p^2s] e^{i(\phi_1+\vartheta)}, \\ \tilde{r}_{12} &= \tilde{r}'_{12} = \tilde{r}_{21} = \tilde{r}'_{21} = (1-s) \sqrt{p^2(1-p^2)} e^{i[(\phi_1+\phi_2)/2+\vartheta]} \\ \tilde{r}_{22} &= -[p^2 + (1-p^2)s] e^{i(\phi_2+\vartheta)}. \end{aligned} \quad (4.10)$$

We omit a detailed analysis of the phases in Eqs. (4.7)-(4.10) since they do not explicitly enter our analysis in the following. With the above parametrization the absolute square of t_{11} [Eq. (4.6)] can be simplified to [39, 40, 73]

$$T^{\text{tot}} = |t_{11}|^2 = \frac{(1-s^2)^2}{|\alpha|^2|\beta|^2} \frac{\sin^2(\eta/2 + \vartheta_0)}{\sin^2(\eta/2 + \vartheta_0 + \Delta) + \Gamma_0^2}, \quad (4.11)$$

with $\phi = (\varphi_2 + \phi_2) - (\varphi_1 + \phi_1)$, $\eta = (\varphi_2 + \phi_2) + (\varphi_1 + \phi_1)$, $r' = (1-p^2) e^{-i\phi/2} + p^2 e^{i\phi/2}$, $\delta = \arg(r')$, $\vartheta_0 = \vartheta + \delta$, $\alpha = 1 + s e^{i(\eta+2\vartheta)}$, $\beta = 1 + s e^{-2i\delta}$, and $\Delta = \arg(\beta/\alpha)$.

The linewidth Γ_0 is given by

$$\Gamma_0 = \left| \frac{1 - |r'\beta/\alpha|^2}{2r'\beta/\alpha} \right|. \quad (4.12)$$

In the generic case of $s \neq 0$, resonances occurring in Eq. (4.11) show a typical Fano profile of the form [34]

$$T^{\text{tot}} \approx |t^{\text{bg}}|^2 \frac{(B/c - B_n/c)^2}{(B/c - B_n/c + \Delta)^2 + \Gamma_0^2}, \quad (4.13)$$

with t^{bg} being the coefficient for background scattering [78]. The Fano resonances at $B/c = B_n/c - \Delta$ will have an asymmetric lineshape unless $\Delta = 0$ (i.e. $s = 0$). This is however the case for the billiard systems we consider, since almost no reflection of incoming lead states takes place at the lead mouths, $\tilde{r}''_{11} \approx 0$, and therefore $s \approx 0$. Under this assumption Eq. (4.11) simplifies to

$$T^{\text{tot}} \approx \frac{\sin^2(\eta/2 + \vartheta_0)}{\sin^2(\eta/2 + \vartheta_0) + \Gamma_0^2}, \quad (4.14)$$

with linewidth $\Gamma_0 = (1 - |r'|^2)/(2|r'|)$. This equation describes symmetric resonance lineshapes which can be identified as *window resonances* (also called Breit-Wigner dips/antiresonances) of the form

$$T^{\text{tot}} \approx \frac{(B/c - B_n/c)^2}{(B/c - B_n/c)^2 + \Gamma_0^2}. \quad (4.15)$$

The physical picture resulting from this analysis is the following: In the magnetic field region $B_c^2 \leq B \leq B_c^1$, where two edge states are present in the interior of the dot and one in each of the leads, the transmission probability shows large-scale oscillations intersected by sharp window resonances. The large-scale envelope function is given by $1/(1 + \Gamma_0^2)$. Its maxima perfectly match with the roughly estimated term $\cos^2[B(A_1 - A_2)/(2c)]$ from Eq. (4.5) and can therefore be identified with the numbered points in Fig. 4.2, each of which corresponds to an integer number of longitudinal antinodes in the wavefunction along the boundary (see Fig. 3.3). The antiresonances superimposed on these oscillations occur at magnetic fields $B = B_n$ (where $\eta/2 + \vartheta_0 = n\pi$, $n \in \mathbb{Z}$) and their linewidth is given by Γ_0 . As a result, resonances which are situated on maxima of the term $1/(1 + \Gamma_0^2)$ are sharper than at its minima [see numerical data in Fig. 4.2 and Fig. 4.6 for confirmation]. For an increasing number of edge states populated in the cavity ($B < B_c^2$) our numerical results show that the density of antiresonances is rapidly growing. This behaviour finally leads to a resonance overlap for a large number of edge states which is prerequisite for the onset of Ericson fluctuations (i.e. universal conductance fluctuations). For completeness we remark that the above analysis for the B -dependence of T^{tot} can likewise be carried out with k_F instead of B as the variable parameter. We can similarly identify threshold values k_c^n in the wavenumber k_F , below which a number of n edge states survive. As an example we show some numerical results for the transmission probability $T^{\text{tot}}(k_F)$ in the case of one, two, and three participating edge states in Fig. 4.7. The occurring Aharonov-Bohm oscillations and sharp resonances can again be described by Eq. (4.4) or Eq. (4.11) respectively.

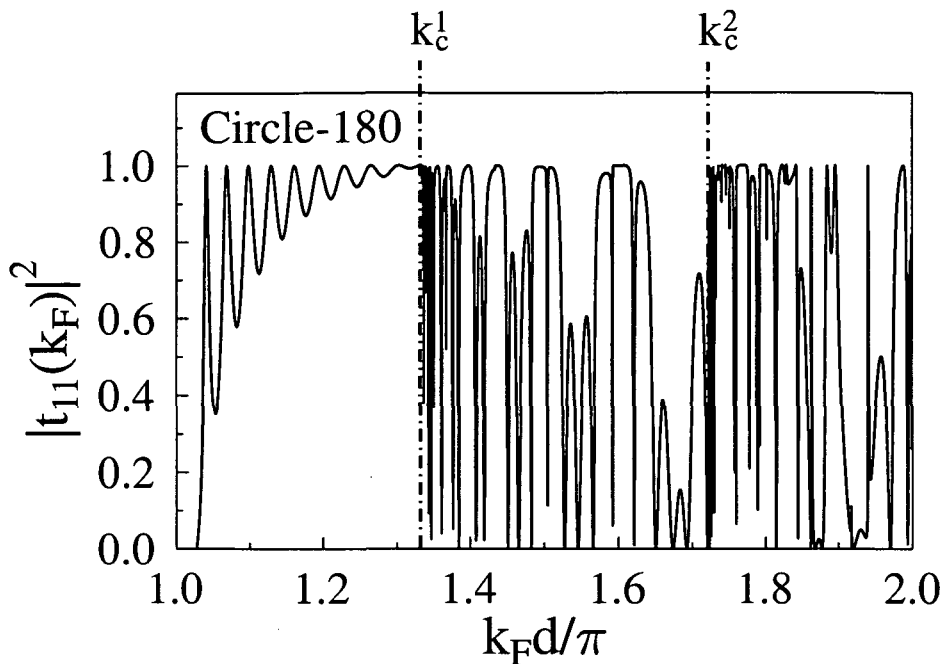


Figure 4.7: *First mode transmission probability through the circular billiard with 180° lead orientation and magnetic field strength $B/c = 93.6$ as a function of the electron wavenumber k_F . Above the critical wavenumbers k_c^1 (k_c^2) the second (third) edge state in the circle can be accessed. Note that depending on the number of accessible edge states Aharonov-Bohm oscillations and Fano resonances are observable here as a function of k_F , similar to the case of varying the magnetic field B (see Fig. 4.2).*

4.4 Comparison with experiments

A series of experiments [1, 2, 76, 79, 80] have been performed where Aharonov-Bohm oscillations (ABOs) similar to the ones discussed here have been observed in ballistic transport measurements. The origin of the ABOs in these experiments is however twofold: In Refs. [1, 2, 76], it is the presence of edge states in a quantum dot which gives rise to the observed oscillations. In Refs. [79, 80] on the contrary, the investigated scattering devices have the form of a ring, to which the scattering wave function is confined. The latter set-up thus gives rise to ABOs already at low magnetic fields and has therefore been more readily accessible to a theoretical description [81]. However, to our knowledge, no quantitative description for magnetotransport through a quantum dot in the regime of only one or two participating edge states has yet become available. We therefore discuss in the following similarities and differences between our calculations and the experimental data from [1, 2]. One important observation is that the magnetic fields where these quasi-regular transmission fluctuations appear in the experiment are lower than in the present calculation. For example, in the experiment for circle and stadium shaped quantum dots in a *GaAs/AlGaAs*-heterostructure [1, 2], the threshold magnetic field values

would be (in SI-units)

$$B_c^n = \frac{2\pi h}{(2n+1)\lambda_F^2 e} \quad \text{with} \quad \lambda_F = \sqrt{\frac{2\pi}{n_s}}. \quad (4.16)$$

With a sheet density of $n_s = 3.6 \times 10^{11} \text{cm}^{-2}$ in the interior of the dot, the threshold magnetic fields are given by $B_c^2 \approx 3$ Tesla and $B_c^1 \approx 5$ Tesla. However, in the experiment regular oscillations were already observed below 2 Tesla. At those field values we find highly irregular transmission fluctuations corresponding to a threshold magnetic field B_c^n with $n \gg 1$, indicative of a high density of resonances and Ericson fluctuations. We expect the origin of this discrepancy to lie in the absence of sharp edges in the experiment and, hence, of diffractive edge scattering. In the experimental quantum dot, the edges should be fairly smooth, leading to near-adiabatic transitions to edge states at the entrance to the quantum dot. Therefore fewer edge channels are excited than by diffractive edge scattering, where all energetically accessible channels up to n are populated. Our present results suggest that the observed transmission fluctuations are a direct measure of the sharpness of the edges at the lead mouth. Therefore, investigations of quantum dots with varying sharpness of edges would be desirable. Since these are, however, difficult to fabricate we consider a different experimental approach which is based on the analogy between transport in the edge state regime and field-free transport through a rectangle. Such structures are accessible for microwave experiments [11, 82] and will be considered in the next chapter. The measured transmission through such a microwave device provides a stringent test for the multi-channel interference model presented above. For a truly quantitative comparison between the experiment and the numerical data, also the residual decoherence present in the transport process has to be accounted for by the MRGM. As will be shown, such a decohering mechanism can indeed be incorporated in the MRGM. As a result we obtain excellent agreement between the measurement and our calculations.

Chapter 5

Fano resonances

In the previous chapter we encountered so-called *window resonances* in transport through quantum dots at very high magnetic fields. In the presented multi-channel interference model the symmetric lineshape of these resonances naturally occurred as the limiting case of the more general asymmetric Fano lineshapes. Our aim in the following is to learn more about these asymmetric resonances in quantum transport processes.

Generally speaking, Fano resonances can be seen as a scattering feature which occurs when (at least) one resonant and one non-resonant pathway connecting the entrance with the exit channel interfere. Fano resonances have been observed in a wide array of different subfields of physics starting with photoabsorption in atoms [34, 83, 84], electron and neutron scattering [85, 86], Raman scattering [87], photoabsorption in quantum well structures [88], scanning tunnel microscopy [89], and ballistic transport through quantum dots (“artificial atoms”) [78, 90–92]. Interest in observing and analyzing Fano profiles is driven by their high sensitivity to the details of the scattering process. For example, since Fano parameters reveal the presence and the nature of different (non) resonant pathways, they can be used to determine the degree of coherence in the scattering device. This is due to the fact that decoherence converts Fano resonances into the more familiar limiting case of a Breit-Wigner resonance [93]. Furthermore, they provide detailed information on the interaction between nearby resonances leading to “avoided crossings” in the complex plane [94, 95], and to stabilization of discrete states in the continuum (“resonance trapping” [96, 97]).

5.1 Transport through a microwave cavity

For a closer investigation of Fano resonances in the field of ballistic quantum transport we make use of the following three observations:

1. The multi-channel interference model discussed above not only describes transport through quantum dots in the edge-state regime, but also other field-free transport processes like through carbon nanotubes [39, 40] or through rectangular quantum dots with parallel lead orientation as in Fig. 2.1b [74].

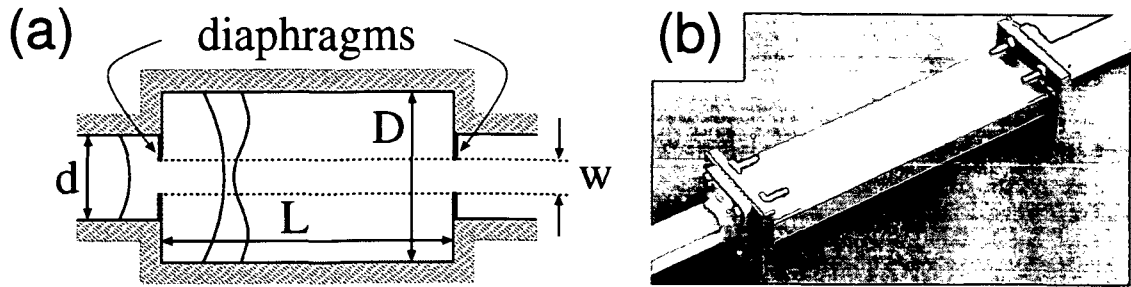


Figure 5.1: (a) Schematic sketch of the microwave scattering device consisting of a rectangular cavity with leads attached symmetrically on opposite sides. Tunable diaphragms at the lead junctions allow to control the coupling between the cavity and the leads. Note the fourfold symmetry of the complete set-up. The open even transverse cavity states are indicated. (b) Photograph of the experimental set-up. The diaphragm-openings are cut into interchangeable thin metal plates screwed between the waveguides and the cavity (not visible).

2. In the multi-channel interference model we encountered the parameters s and p on which the lineshape of the resonances is strongly dependent. Varying these parameter should allow to tune resonances through the whole spectrum of Fano lineshapes.
3. Two-dimensional coherent single-electron transport at zero magnetic field can be experimentally simulated by *microwave billiards* [11]. In particular, measurements on rectangular microwave cavities which can be described with the multi-channel interference model are conveniently realized and show good agreement between experiment and theory [82].

Combining all of the three above observations, we arrive at the design of a scattering device which is particularly suitable for the investigation of tunable Fano resonances (see Fig. 5.1). In its experimental realization, our scattering facility consists of two commercially available waveguides (height $h=7.8$ mm, width $d=15.8$ mm, length $l=200$ mm) which were attached both to the entrance and the exit side of a rectangular resonator (height $H=7.8$ mm, width $D=39$ mm, length $L=176$ mm). At the junctions to the cavity metallic diaphragms of different openings were inserted. The microwaves are injected with frequencies between 12.3 and 18 GHz, where two even transverse modes are excited in the cavity and one transverse mode in each of the leads. To ensure strong coupling, the injection of microwaves is mediated by an adaptor.

We further note that the design of the set-up incorporates the following practical features: Transport across this rectangular cavity with parallel leads can be described very conveniently by the multi-channel interference model. Except for the magnetic field dependence and effects going beyond the single particle picture (e.g. electron-electron interaction), the dynamics of microwaves and electrons is equivalent. For this reason our device also simulates ballistic electron motion through a quantum

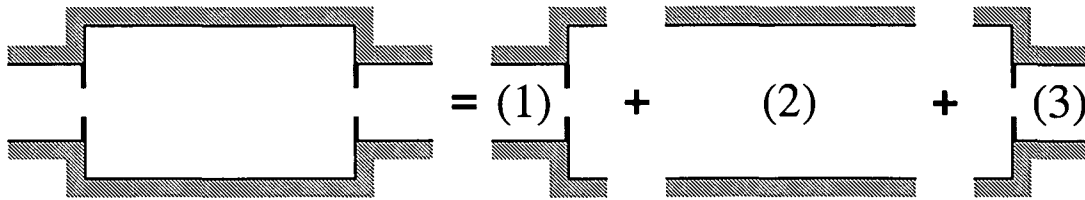


Figure 5.2: *Decomposition of the scattering device into three separate substructures: (1) a junction with diaphragm from a narrow to a wide constriction, (2) a wide constriction of length L , and (3) a junction from a wide to a narrow constriction with diaphragm.*

dot. Furthermore, the amplitude s , which plays the role of the tuning parameter, can be varied by the additional diaphragms inserted between the leads and the cavity. In contrast to recent investigations on mesoscopic dots and single-electron transistors [90, 92, 93], where comparison between theory and experiment has remained on a mostly qualitative level, our model system allows for a detailed quantitative analysis of all features of tunable resonances, since decoherence is kept at a low level. By comparison with numerical results obtained by the MRGM, the parametric variation of Fano resonances and the degree of decoherence can be quantitatively accounted for.

5.2 Comparison between experiment and theory

In the following we will present a detailed comparison between the experiment and the predictions of the MRGM. The measurements on the microwave scattering experiment were performed by Kuhl and Stöckmann at the Philipps University in Marburg, Germany. We solve the S matrix for the single particle Schrödinger equation for this quantum dot by assuming hard-wall boundaries and imposing scattering boundary conditions at asymptotic distances. The coupling of the leads to the cavity of length L is varied by changing the width of two symmetrically placed diaphragms in the interval $w \in [0, d]$ (see Fig. 5.1). The lead width d and the width of the rectangular cavity D determine how many flux-carrying modes are open at a certain energy E in each of the three scattering regions (lead-cavity-lead). We consider in the following the range of wavenumbers where one flux-carrying mode is open in each of the leads, while the first and second even transverse modes are open inside the cavity, thus providing two alternative pathways of quantum transport. In order to explain how transport across the cavity can be rewritten in terms of the multi-channel interference model, we decompose this process into a multiple scattering series. This decomposition is equivalent to the model we discussed previously for transport by edge states (see section 4.3). It involves three pieces [74], each of which is characterized by a mode-to-mode transmission (reflection) amplitude or a propagator (see Fig. 5.2): (1) the transmission of the incoming flux from the left lead state m into the transverse mode i in the cavity, \tilde{t}_{mi} , or reflection back into the lead, \tilde{r}_{mk}'' , (2) the propagation inside the cavity from the left to the right, $G^{(LR)}$, or

from the right to the left, $G^{(RL)}$, and (3) the transmission from the cavity state i to the state n of the right lead, \tilde{t}_{in} , or internal reflection at each of the two vertical cavity walls with amplitude \tilde{r}_{ij} . We note that all of these quantities (1)-(3) can be obtained independently of each other by the MRGM. The transport coefficients in (1) and (3) are evaluated by numerically calculating the transmission amplitudes for transport from a narrow lead of width d to a wide lead of width D and vice versa (see Fig. 5.2). The lead Green's functions are, however, connected to each other by Dyson equations only at those grid points, which lie within the opening w of the diaphragms. For the evaluation of the Green's functions for propagation inside the cavity (2), we make use of the absence of mode mixing in the rectangular cavity. This feature is equivalent to the case of edge state transport and permits to write $G^{(LR)}$ and $G^{(RL)}$ as a spectral sum over transverse modes,

$$G^{(LR)}(x_R, x_L) = G^{(RL)}(x_L, x_R) = \sum_n |n\rangle \exp(ik_n|x_R - x_L|)\langle n|. \quad (5.1)$$

The variables $x_{R,L}$ are the x -coordinates of the right (left) lead junction with $|x_R - x_L| = L$. The longitudinal momentum for each channel n in the cavity is given by $k_n = \sqrt{k^2 - (k_n^c)^2}$, with the momentum $k = \sqrt{2\varepsilon}$ and the threshold k -values $k_n^c = n\pi/D$. In perfect analogy to Eqs. (4.1,4.2) we further define the following matrices

$$[\tilde{T}]_{ij} = \tilde{t}_{ij}e^{ik_jL}, \quad [\tilde{T}']_{ij} = \tilde{t}'_{ij} \quad \text{and} \quad [\tilde{R}]_{ij} = \tilde{r}_{ij}e^{ik_jL}. \quad (5.2)$$

The transmission through the whole cavity $t_{ji} = [T]_{ij}$ can then be conveniently formulated in terms of a geometric series of matrices,

$$\begin{aligned} T(k) &= \tilde{T} \left(1 + \tilde{R}\tilde{R} (1 + \tilde{R}\tilde{R} (1 + \dots)) \right) \tilde{T}' \\ &= \tilde{T} \left(\sum_{i=0}^{\infty} (\tilde{R}\tilde{R})^i \right) \tilde{T}' = \tilde{T} (1 - \tilde{R}\tilde{R})^{-1} \tilde{T}'. \end{aligned} \quad (5.3)$$

The above formulation of the transport process has the following convenient features:

1. Rewriting Eq. (5.3) in terms of six independent parameters as in section 4.3 describes analytically how Fano resonances emerge in the transmission probabilities.
2. The identification of the resonant and non-resonant pathways relevant for the formation of Fano resonances is straightforward with the help of Eq. (5.3): Due to the absence of inter-channel mixing in the rectangular cavity, the non-resonant contribution corresponds to the $n = 0$ term of the sum describing direct transmission while the resonant contribution is made up by all multiple-bounce contributions ($n \geq 1$) in Eq. (5.3).
3. Decoherence effects due to dissipation of the microwave power in the cavity walls can be easily incorporated by analytically continuing k_n into the complex plane, $k_n = \sqrt{k^2 - (k_n^c)^2} + i\kappa$. With this extension the quantitative analysis of Fano resonances can be used to accurately determine the degree of dissipation present in microwave cavities.

To demonstrate the emergence of Fano resonances in transmission, we go back to section 4.3, where all the features of the multi-channel interference model were introduced. We now make use of the explicit dependence of the transmission on the two parameters s and p . In the present context s is the modulus of the reflection amplitude of the incoming wave in mode 1 and reflected into mode 1 at the left diaphragm [see Eq. (4.7)]. This parameter p is the partial injection amplitude of the incoming wave into the lowest mode of the cavity, corrected for the partially reflected flux [see Eq. (4.8)]. The key observation in the present context is that the square module s^2 is monotonically decreasing in between the limiting values $s^2 = 1$ for zero diaphragm opening ($w = 0$) and $s^2 \approx 0$ for fully open diaphragms ($w = d$). The parameter s plays a crucial role in the expression for the transmission probability $|T(\varepsilon, s)|$ as a function of the energy ε . Close to a given resonance ε_i^R this expression can be approximated by the Fano form as in Eq. (4.13) [34, 39, 40, 73],

$$|T(\varepsilon, s)|^2 \approx \frac{|\varepsilon - \varepsilon_i^R(s) + q_i(s) \Gamma_i(s)/2|^2}{[\varepsilon - \varepsilon_i^R(s)]^2 + [\Gamma_i(s)/2]^2}, \quad (5.4)$$

where $\varepsilon_i^R(s)$ is the position of the i -th resonance, $\Gamma_i(s)$ its width, and $q_i(s)$ the complex Fano asymmetry parameter, all of which depend on s . Window resonances appear in the limit $q \rightarrow 0$ while the Breit-Wigner limit is reached for $|q| \gg 1$. It should be noted that, in general, q cannot be simply identified with the ratio of resonant to non-resonant coupling strength [98, 99]. Fig. 5.3 presents both the experimental and theoretical dependence of the transmission probability $|T|^2$ on k (or ε). In the measurement, the diaphragms were successively closed in steps of 1 mm. The data sets of Fig. 5.3a,b,c represent the transmission probability for three different values of the opening of the diaphragms $w = 5.8, 8.8, \text{ and } 15.8$ mm, respectively. Note the remarkable degree of agreement between the measured and the calculated data without any adjustable parameter. In Fig. 5.3a where $w/d \approx 0.37$, transport is suppressed and mediated only by resonance scattering with narrow Breit-Wigner shapes centered at the eigenenergies of the closed billiard as indicated by the ticmarks. With increasing diaphragm opening (Fig. 5.3b) transport acquires a significant non-resonant contribution, leading to the widening and the overlap of resonances. Finally, for fully open leads (Fig. 5.3c) $w/d = 1$ (or $s \approx 0$), resonances appear as narrow window resonances in a non-resonant continuum. The trajectory of the resonance parameter as a function of s can be both experimentally and theoretically mapped out in considerable detail. Different types of resonances can be identified by their characteristically different resonance parameters. The evolution of the Fano parameter as a function of w/d (or s) for one resonance is highlighted in Fig. 5.4. The transition from a narrow Breit-Wigner resonance via a somewhat wider asymmetric Fano profile to a window resonance is clearly observable. The good agreement with theory allows to accurately determine the degree of decoherence present in the experiment. As the Fano profile, in particular near its minimum, is very sensitive to any non-interfering incoherent background, we can determine an upper bound for the damping by comparison between experiment and theory to be $\kappa \lesssim 10^{-4}$. As illustrated in Fig. 5.4, even a slightly larger value of $\kappa = 10^{-3}$ would drastically deteriorate the agreement between experiment and theory. In line

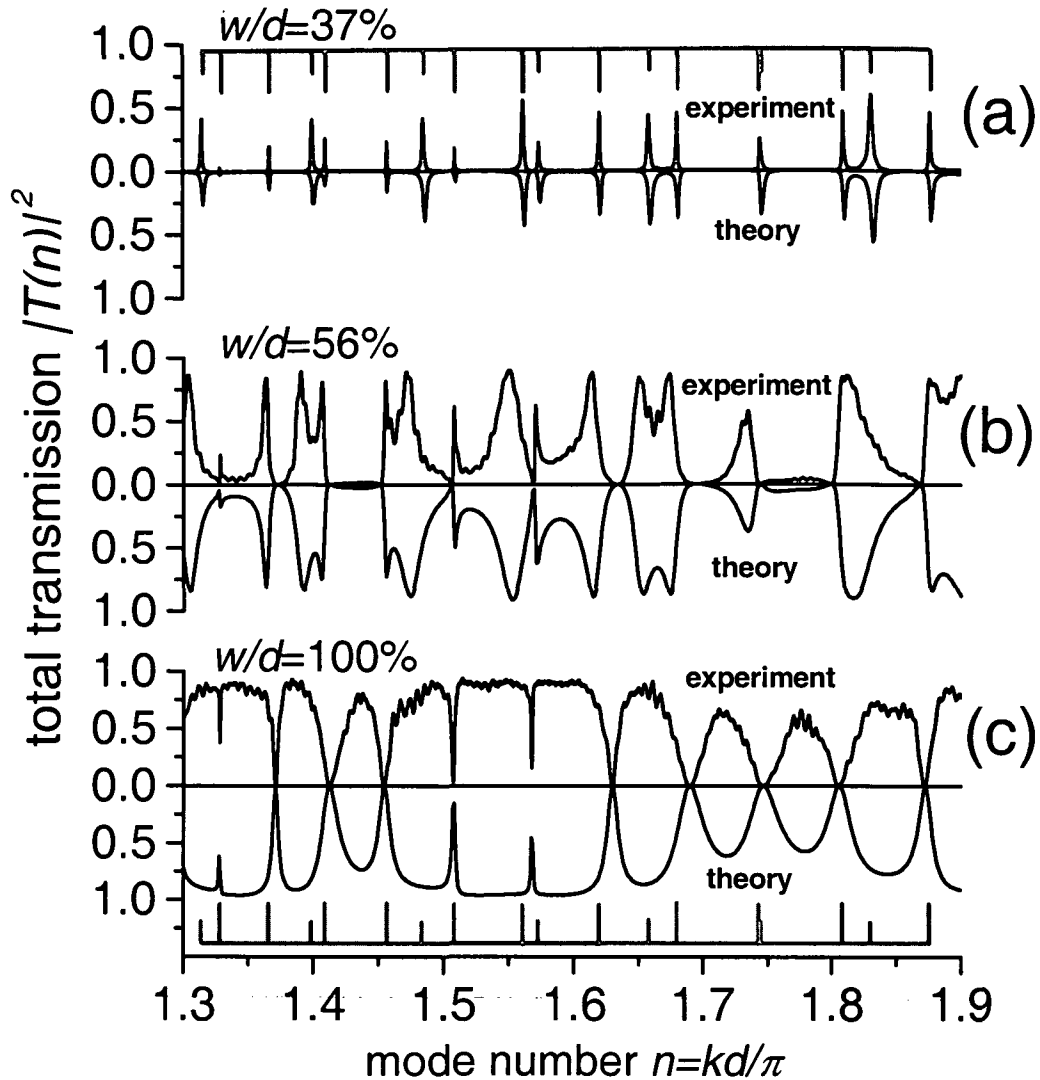


Figure 5.3: Total transmission probability, $T^{\text{tot}}(\sqrt{2\epsilon d}/\pi, w/d)$, for transport through the rectangular cavity with three different openings of the diaphragms: (a) $w/d = 37\%$, (b) $w/d = 56\%$ and (c) $w/d = 100\%$. For better comparison, the experimental (calculated) results are shown as mirror images. The positions of all eigenstates in the closed cavity are indicated by the gray tickmarks (for explanation of long vs. short tickmarks see text).

with the value $\kappa = 10^{-4}$, we obtain an imaginary part of the complex Fano parameter for systems without time-reversal symmetry [93] out of our fitting procedure as $\text{Im} q \lesssim 0.1$.

We note that decoherence in an open quantum system can be caused by different mechanisms: dephasing and dissipation. In Ref. [93] the decohering process considered was dephasing. Our results for the variation of a Fano resonance clearly demonstrate that dissipation has the same interference-reducing (i.e. decohering) effect on a Fano resonance as dephasing does: in both cases the Fano resonance acquires a complex asymmetry parameter q . This is one of the interesting highlights

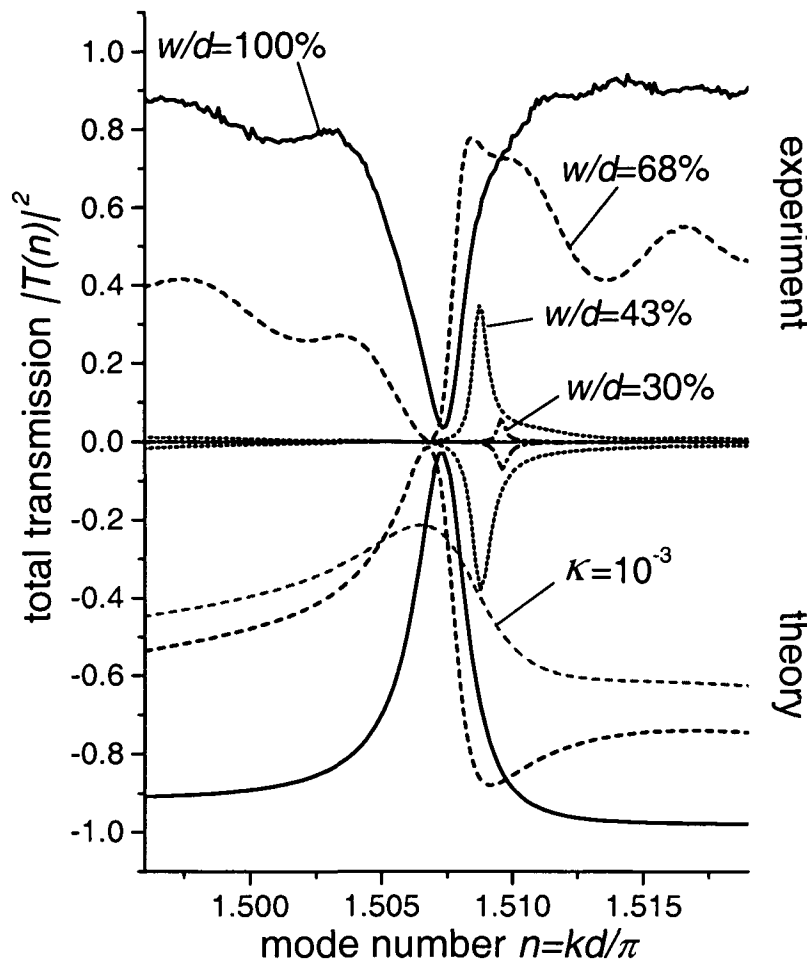


Figure 5.4: Fano resonance near the second even excited transverse mode at $kd/\pi \approx 1.5095$. Experimental and theoretical result for four different cavity openings (w/d) are shown. Curves with equal w/d -ratio are displayed in the same line style (solid, dashed, dotted, dash-dotted). For all calculated curves a damping factor $\kappa = 10^{-4}$ was used, except for the additional gray dashed curve shown for which $\kappa = 10^{-3}$ and $w/d = 0.68$.

of our experiment, which, to our knowledge, has not been demonstrated before. We note that by using superconducting cavities κ could still be further reduced [100], however with little influence on the result, since we have already nearly reached the fully coherent limit.

Following the parametric evolution of a large number of resonances yields a characteristic pattern of Fano resonance parameters (Fig. 5.5). Obviously, two distinct subsets of resonances appear in the rectangular billiards: one set is characterized by a strictly monotonic increase of Γ with increasing opening of the cavity and a large and only weakly dependent asymmetry parameter q . A second set of resonances features a strongly varying q (on the log-scale!) from large values near the Breit-Wigner limit to values close to $q \approx 0$ for wide opening, yielding a window resonance. At the same time, the width Γ first increases with w/d increasing from close to 0, then

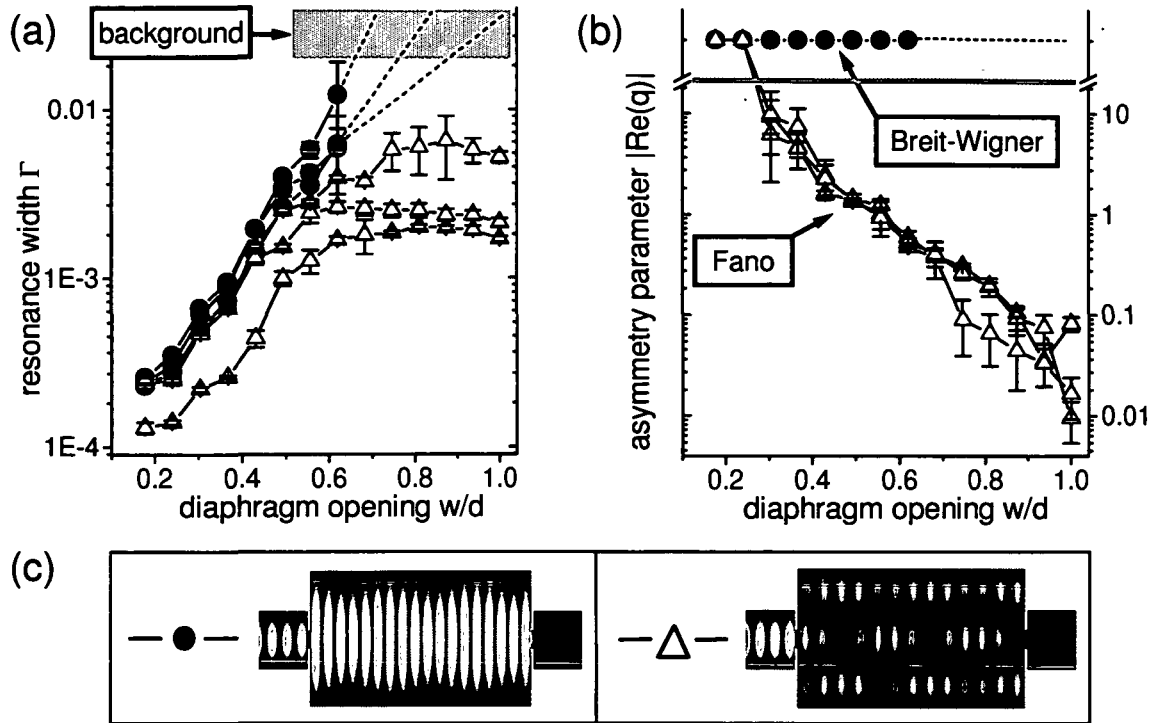


Figure 5.5: (a) Resonance width Γ and (b) real part of the asymmetry parameter $|\text{Re}(q)|$ as a function of the diaphragm opening w/d . The data are obtained by fits to experimental results. Solid circles ● (empty triangles Δ) correspond to resonances originating from the first (second) even cavity eigenstate. Typical wavefunctions $|\psi(x,y)|^2$ for these two classes of resonances are shown in (c) [101]. In (a) the width Γ of the ●-resonances is monotonically growing until resonances disappear in the background of the measured spectra (see gray horizontal bar). For Δ -resonances Γ reaches a local maximum and slightly decreases for $w/d \rightarrow 1$. In (b) the ●-resonances always have a $|\text{Re}(q)| > 10$, above which the Fano resonances are very close to the Breit-Wigner lineshape $[\text{Re}(q) = \infty]$. For the Δ -resonances q shows a strong w/d -dependence: resonances undergo a complete evolution from Breit-Wigner to window type as w/d varies between 0 and 1.

reaches a local maximum and finally decreases slightly when $w/d \rightarrow 1$. A similar non-monotonic behavior of Γ was recently observed in a single-electron transistor experiment [90]. Such features can be understood in terms of avoided crossings in the complex plane [94, 95] between interacting resonances. While the von Neumann-Wigner theorem [102] for bound states predicts avoided crossings between states of the same symmetry and thus a non-monotonic variation of the eigenenergy, interacting resonances can also display avoided crossings on the imaginary axis [94, 95], i.e. exchange of the width of resonances and thus leading to a non-monotonic behavior of one of the Γ involved. The two resonance poles approach each other in the complex energy plane and undergo an avoided crossing as a function of the coupling parameter s . As a result, for increasing s the resonance with large Γ gets even larger and will form a background, on top of which the narrow resonance is situated. This

somewhat counterintuitive stabilization or even narrowing of the width of one resonance despite an increased opening, i.e. an increased coupling to the environment, is sometimes referred to as “resonance trapping” [96, 97] and in the limit of $\Gamma \approx 0$ as the “formation of bound states in the continuum”. This could possibly provide an alternative explanation for the results of Ref. [90], where such a non-monotonic behavior was observed and has been previously explained in terms of increased impurity scattering [93].

A very interesting feature of the interacting resonances is the fact that they can be completely characterized in terms of scattering wavefunctions (see Fig. 5.5c). Resonances that undergo a complete evolution from Breit-Wigner resonances to a window resonance are all associated with the *second* even excited state in the cavity, while resonances that display a strictly monotonic increase of the width with increasing cavity opening are connected to transport through the transverse *ground state* of the cavity. This mapping is controlled by the amplitude p for transmission through the first transverse mode [see Eqs. (4.7,4.8)]. In the case that $p^2 > 1/2$ all resonances associated with the first mode are broader than the resonances associated with the excited state and vice versa for $p^2 < 1/2$. For geometric reasons the scattering device studied here (Fig. 5.1) always favors transport through the first cavity mode and therefore $p^2 > 1/2$. In this way we arrive at the remarkably simple result that all resonances associated with a first mode feature a strictly monotonic Γ and a large, but weakly varying q , while all resonances associated with the second mode feature a smaller and not strictly monotonic Γ with q undergoing the complete evolution from the Breit-Wigner to the window limit. This one-to-one mapping is also indicated in Fig. 5.3, where only second-mode resonances (indicated by the dotted ticmarks) “survive” the transition of $w/d \rightarrow 1$ while all first-mode resonances (short ticmarks) vanish in the background of the transmission spectrum. This knowledge could be very useful for the investigation of electron dynamics in mesoscopic scattering systems where the parametric evolution of Fano resonances could yield information about the interaction of internal states and their coupling to the environment.

The resonance poles in the complex plane can also be investigated explicitly with the help of the multi-channel interference model. Using analytical expressions for the transmission probability, we can evaluate these expressions also at complex values of the wavenumber k . In such a way the dynamics of poles in the complex k -plane can be analyzed as a function of the diaphragm opening. Inspired by the work in [103, 104] we calculated contour plots of the transmission probability (displayed in Fig. 5.6). For full opening of the diaphragms ($s = 0$) the complex poles and the “zeros” in the transmission probability on the real k -axis occur at the same $\text{Re}(k)$, thus giving rise to symmetric resonances (see Fig. 5.6a). When gradually closing the diaphragms, the poles are situated at a $\text{Re}(k)$ which is different from the position of the zero on the real axis. Such a constellation gives rise to asymmetric Fano resonances (see Fig. 5.6b,c). If the diaphragms are almost shut ($s \approx 1$), we are left with a number of poles, which are situated very close to the real k -axis (see Fig. 5.6d). The resulting resonances are thus very narrow and isolated from each other.

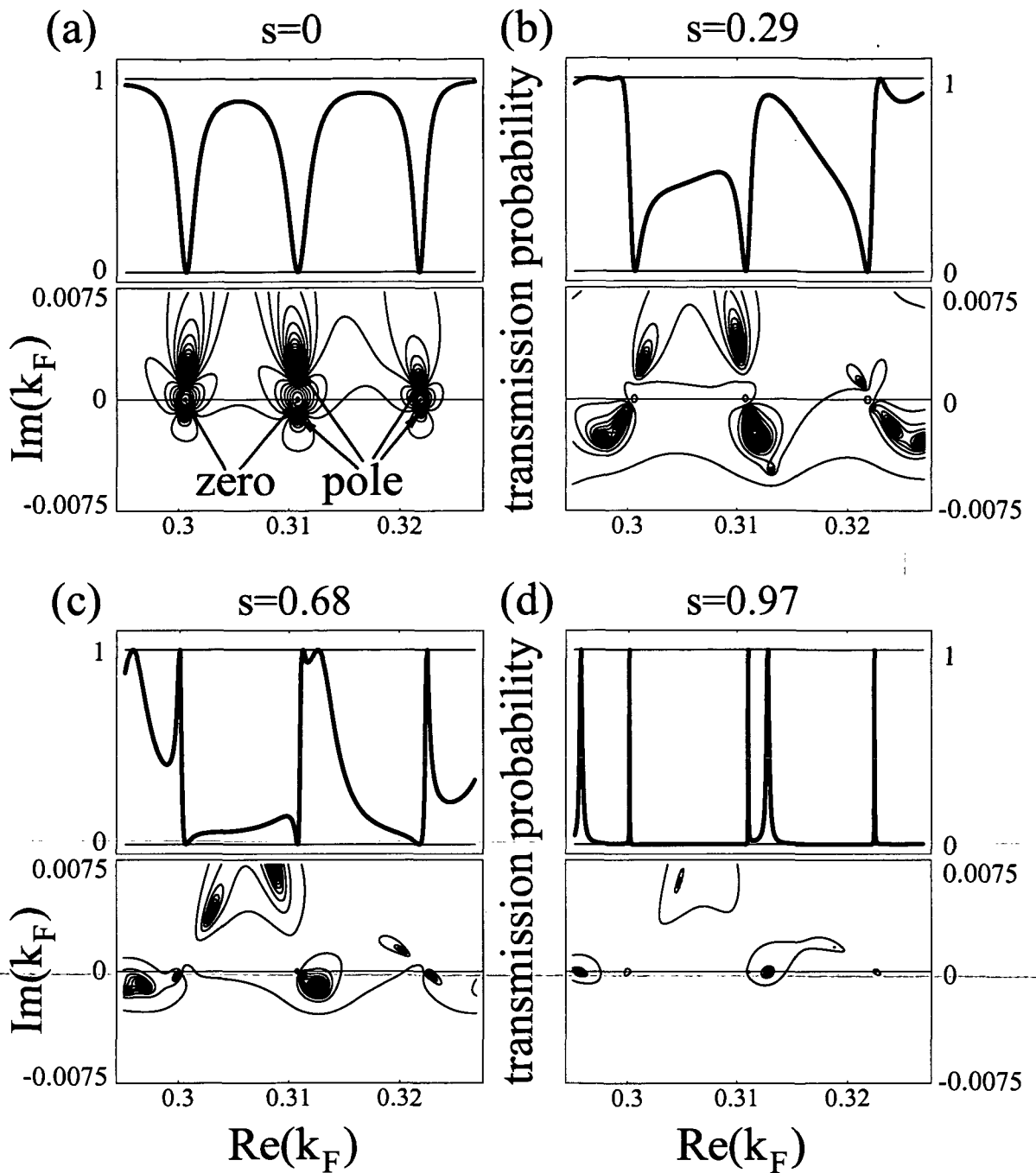


Figure 5.6: The k_F -dependence of transmission through the rectangular cavity, calculated with the multi-channel interference model. The diaphragms are successively closed: (a) $s = 0$, (b) $s = 0.29$, (c) $s = 0.68$, and (d) $s = 0.97$. The upper half of each figure shows the transmission probability on the real k -axis. The lower half depicts contour plots of the transmission probability in the complex k -plane. Poles and zeros in transmission move in the k -plane as a function of the opening of the diaphragms. Two of the zeros and four of the poles in (a) are marked by green arrows.

Chapter 6

Edge states and the integer quantum Hall effect

An important phenomenon in transport theory and condensed matter physics is the Hall effect. As Edwin Hall discovered in 1879, electrons flowing through a conducting bar give rise to a voltage perpendicular to their flux direction if a magnetic field B is present orthogonal to the surface of the bar. This effect can be explained by the Lorentz force the electrons are subject to. The voltage measured perpendicular to the electron current is called *Hall voltage* V_H and is linearly proportional to the magnitude of the magnetic field B . In 1980 Klaus von Klitzing found that the value of the Hall voltage in special semiconductor samples is quantized at low temperatures and very high magnetic fields [35]. When the quantization occurs at integer values of some unit voltage value we speak of the *integer quantum Hall effect* (as opposed to the *fractional quantum Hall effect* discovered soon thereafter) [6].

For the emergence of the quantum Hall effect the presence of edge states plays a crucial role [69]. Since the systems discussed in this thesis also give rise to edge states at high magnetic fields, we investigate in the following which traces of the quantum Hall effect are observable in our idealized scattering systems. With respect to the experimental conditions of the quantum Hall measurements the most drastic idealizations in the MRGM are the following:

1. The studied devices in the experiments are multi-electron systems. In our theory we make a single-electron approximation.
2. In a real Hall bar the potential landscape is most likely similar to a random surface with non-zero spatial correlation. In our calculations so far, we fixed the potential inside the dot to be constant.

The approximation (1) is a severe restriction which cannot be overcome within the present MRGM. For this reason we are not able to calculate the fractional Hall effect, since it is essentially a multi-electron phenomenon. Limitation (2) can be overcome by including random site energies in the tight-binding Hamiltonian. The challenge here is the inclusion of a random potential which is compatible with the separability requirements in the modules.

6.1 The Hall voltage

To obtain the Hall voltage V_H in our open quantum dots, we make use of an approach put forward in Ref. [105]. The idea presented there consists of determining the Hall voltage as the difference between two local chemical potentials at the points a and b ,

$$V_H = \mu_a - \mu_b. \quad (6.1)$$

These two points are positioned as depicted in Fig. 6.1, i.e., perpendicular to the electron flux from the entrance to the exit lead. The density of states in both leads is given by n_0 . As will be shown in Eq. (6.3), V_H is also proportional to the difference between the chemical potentials at the entrance and exit lead (μ_L and μ_R). To derive this result, we calculate the chemical potential at point a by connecting this point to a measurement reservoir (denoted by “ r ”) with a density of states n_r and a chemical potential μ_a . The reservoir interacts with scattering states injected from the left or right lead by a coupling matrix element $\sigma |\psi_a^{L,R}|^2$. The parameter σ describes the coupling between the measurement reservoir and the dot and $\psi_a^{L,R}$ denotes the scattering wave function at point a for states coming from the left or right lead, respectively. Consider now the current coming to the reservoir from the left lead. There are $(\mu_L - \mu_a)n_0$ fully occupied states that may decay into an empty reservoir state. By Fermi’s golden rule, the rate of this interaction is: $\sigma |\psi_a^L|^2 n_r$. The current from the left lead into the reservoir is therefore: $(\mu_L - \mu_a)n_0 \sigma |\psi_a^L|^2 n_r$. Similarly,

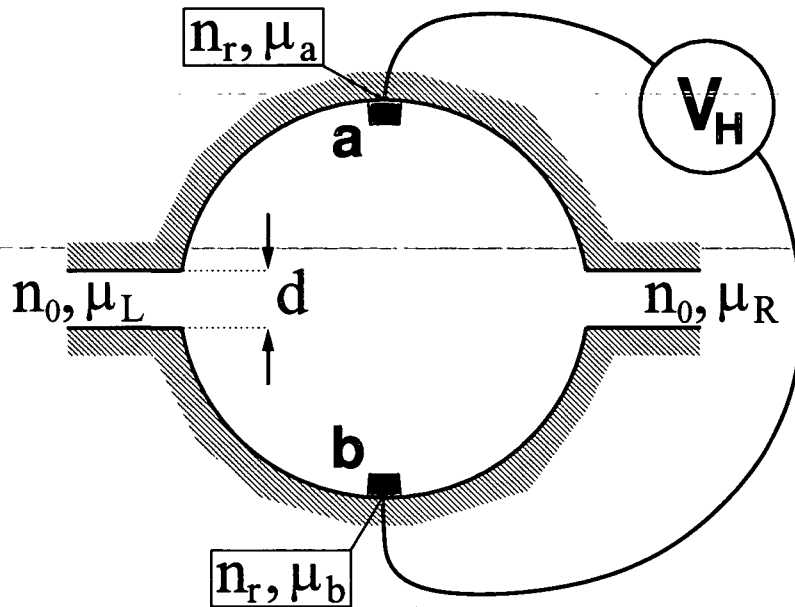


Figure 6.1: *Circular quantum dot connected to the chemical potentials μ_L and μ_R by two leads attached on opposite sides. The Hall voltage is given as the difference between the chemical potentials at point a and b , $V_H = \mu_a - \mu_b$. To each of these two points a reservoir with a density of states n_r and a chemical potential μ_a and μ_b is attached.*

the current resulting from states coming from the right lead into the reservoir is: $(\mu_R - \mu_a) n_0 \sigma |\psi_a^R|^2 n_r$. Since the chemical potential at a is equal to the chemical potential of the reservoir connected with a , the net current between a and the reservoir must be zero. We therefore set the sum of the two above terms equal to zero and get

$$\mu_a = \frac{\mu_L |\psi_a^L|^2 + \mu_R |\psi_a^R|^2}{|\psi_a^L|^2 + |\psi_a^R|^2}. \quad (6.2)$$

The same argument can be applied to the chemical potential at point b . For the difference between the chemical potentials at a and b we then have

$$V_H = \mu_a - \mu_b = (\mu_L - \mu_R) \frac{|\psi_a^L|^2 |\psi_b^R|^2 - |\psi_a^R|^2 |\psi_b^L|^2}{(|\psi_a^L|^2 + |\psi_a^R|^2)(|\psi_b^L|^2 + |\psi_b^R|^2)}. \quad (6.3)$$

The above formula allows to calculate the Hall voltage V_H from the scattering wave functions ψ^L and ψ^R . In practice, the Green's function has to be evaluated twice at both points a and b (once for left and once for right injection). The wavefunctions are obtained according to Eq. (2.75) and inserted into Eq. (6.3). Note that in the special case of fourfold symmetric scattering geometries like in Fig. 6.1, ψ^R is just a mirror image of ψ^L . For all practical purposes it is advisable to evaluate the wavefunctions not just at the two grid points a and b : In order to avoid any local effects we average the wave functions over areas large compared to the grid spacing (indicated by the red areas in Fig. 6.1 and Fig. 6.2) and check whether varying the size of the areas does not alter the results drastically. If more than one lead state ξ_m is injected into the cavity, the total Hall voltage V_H is a sum of all the voltage

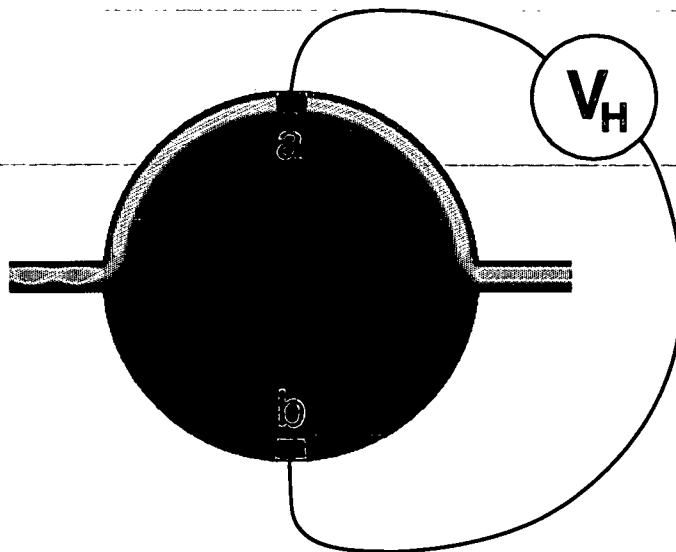


Figure 6.2: Absolute square of a scattering wave function in the single edge state regime of a circular quantum dot. The leads are attached on opposite sides, lead width $d = 0.25$, circle radius $R = 1.5$, wavenumber $k_F = 1.2\pi/d$ and magnetic field $B/c = 100$.

contributions V_H^m originating each from a different state ξ_m ,

$$V_H = \sum_{m=1}^M V_H^m. \quad (6.4)$$

From the Hall voltage we can then easily proceed to other transport quantities like the Hall conductivity G_H , which is defined as

$$G_H = \frac{(\mu_L - \mu_R) T^{\text{tot}}}{2\pi V_H}, \quad (6.5)$$

with T^{tot} being the total transmission probability for transport from the left entrance to the right exit lead.

6.2 Single edge state regime

To apply the above results we will now study one particular example numerically, i.e. transport through the circular dot in the single edge state regime [101]. A typical wavefunction in this magnetic field regime ($B > B_c^1$) is depicted in Fig. 6.2. To investigate the B -dependence of the Hall voltage V_H and the Hall conductivity G_H , we evaluate Eqs. (6.3,6.5) analytically as well as numerically (thereby following similar work in [75]).

As a starting point we reconsider the multi-channel interference model discussed in section 4.4. From the unitarity requirement that has to be fulfilled for the total scattering geometry and for each of the two lead junctions we obtain the following useful relations for the wavefunctions entering Eq. (6.3),

$$\begin{aligned} |\psi_a^L|^2 |t'_{11}|^2 &= T^{\text{tot}}, \\ |\psi_b^R|^2 |t_{11}|^2 &= T^{\text{tot}}, \\ |\psi_b^L|^2 &= |\psi_a^L|^2 |r'_{11}|^2 = |r'_{11}|^2 T^{\text{tot}} / |t'_{11}|^2, \\ |\psi_a^R|^2 &= |\psi_b^R|^2 |r_{11}|^2 = |r_{11}|^2 T^{\text{tot}} / |t_{11}|^2. \end{aligned} \quad (6.6)$$

Inserting these relations into Eq. (6.3), the Hall voltage V_H takes the form

$$V_H = (\mu_L - \mu_R) \frac{|t_{11}|^2 |t'_{11}|^2}{1 - |r_{11}|^2 |r'_{11}|^2}, \quad (6.7)$$

which, to first order, is independent of the magnetic flux. With the expression for T^{tot} [Eq. (4.4)] we derive for the Hall conductivity G_H ,

$$G_H = \frac{1}{2\pi} \frac{1 - |r_{11}|^2 |r'_{11}|^2}{1 - 2 \text{Re}[\tilde{r}_{11} \tilde{r}'_{11} e^{i\gamma}] + |\tilde{r}_{11}|^2 |\tilde{r}'_{11}|^2}, \quad (6.8)$$

where γ is the Aharonov-Bohm phase accumulated by the edge state within one revolution around the dot. In the same way as the total transmission T^{tot} , also the Hall conductivity oscillates periodically as a function of the magnetic field. If,

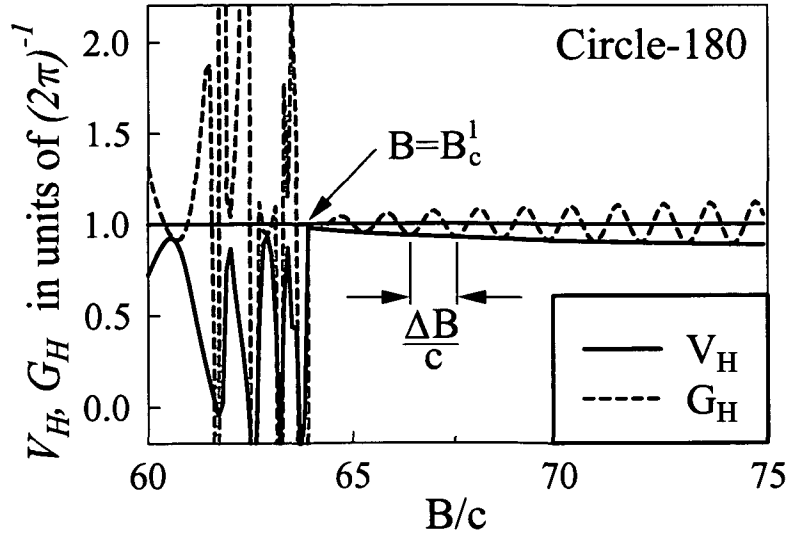


Figure 6.3: Hall voltage V_H and Hall conductivity G_H as a function of the magnetic field B in the circle with 180° lead orientation [101]. Lead width $d = 0.25$, area of the circle $A = 4 + \pi$ and electron wave number $k_F = 1.1001\pi/d$. In the single edge state regime ($B > B_c^1$) the Hall conductivity shows Aharonov-Bohm oscillations around the first Hall plateau at $(2\pi)^{-1}$ with a period of $\Delta B/c \approx 2\pi/A$. The chemical potentials are set here as $\mu_L - \mu_R = (2\pi)^{-1}$, as a result of which the Hall voltage coincides with the lower bound of G_H (see text). In the regime where two edge states are present ($B < B_c^1$) their interference along the boundary (see Fig. 3.3a) gives rise to strong fluctuations both in V_H and G_H .

however, we average Eq. (6.8) with respect to γ (by integration), we obtain the quantization condition of the lowest plateau value in the integer quantum Hall effect,

$$\langle G_H \rangle = \frac{1}{2\pi}. \quad (6.9)$$

We now consider the lower bound of G_H by choosing the angle γ such that the denominator of G_H in Eq. (6.8) becomes maximal. If the two lead junctions of the quantum dot are identical, we further have $t_{11} = t'_{11}$ and $r_{11} = r'_{11}$. Inserting these relations into Eq. (6.8) we have,

$$G_H^{\text{low}} = \frac{1}{2\pi} \frac{1 - |r_{11}|^2 |r_{11}|^2}{1 + 2|\tilde{r}_{11}|^2 + |\tilde{r}_{11}|^2 |\tilde{r}_{11}|^2} = \frac{1}{2\pi} \frac{1 - |r_{11}|^2}{1 + |r_{11}|^2}. \quad (6.10)$$

Under the condition of identical lead junctions also Eq. (6.7) can be simplified,

$$V_H = (\mu_L - \mu_R) \frac{|t_{11}|^2 |t_{11}|^2}{1 - |r_{11}|^2 |r_{11}|^2} = (\mu_L - \mu_R) \frac{|t_{11}|^2}{1 + |r_{11}|^2}. \quad (6.11)$$

Comparing Eq. (6.10) with Eq. (6.11) we note that the lower bound of the Hall conductivity, G_H^{low} , is given by $V_H/[2\pi(\mu_L - \mu_R)]$.

Checking these results with the MRGM we find perfect agreement between the

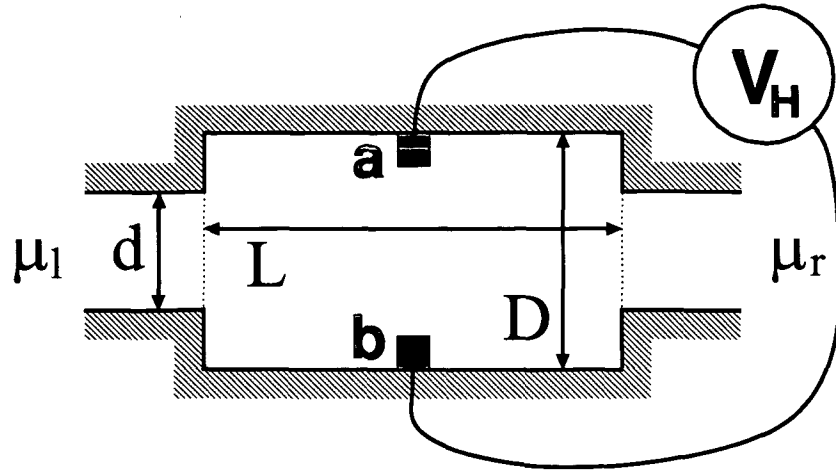


Figure 6.4: *Hall bar geometry: Rectangular quantum dot connected to the chemical potentials μ_L and μ_R by two symmetrically attached leads.*

analytical predictions and the numerical output. The data for V_H and G_H in the single edge state regime are shown in Fig. 6.3. We note that the mean value $\langle G_H \rangle = (2\pi)^{-1}$ and the results on the lower bound of G_H can be clearly confirmed by our numerical calculations.

6.3 Quantization in a Hall bar

To observe more than one plateau in the Hall voltage, we need to allow for more electron flux quanta to enter the scattering cavity. The most straight-forward way to achieve this would be to widen the leads in our scattering devices. In the framework of the MRGM additional link modules would be required to attach broad leads to a circular dot. We therefore choose, for simplicity, the geometry of a so-called *Hall bar*, which is depicted in Fig. 6.4. Unlike the circular dot, it is no problem here to increase the lead width d . Additionally, the Hall bar geometry offers the important advantage of strongly reduced backscattering in the case of widely open leads ($d \approx D$). This absence of scattering between forward and backward propagating edge states is a necessary condition for the quantum Hall effect to be observable [42]. In the single edge state regime of the circular dot this suppression of backscattering is realized “accidentally”, since most of the flux carried by the edge state leaves the cavity already after half a revolution (see Fig. 6.2). With two edge states excited in the circular dot this condition is no longer satisfied. As a consequence, neither V_H nor G_H stabilize around a Hall plateau below B_c^1 in Fig. 6.3. Strong fluctuations in V_H and G_H appear instead.

In the following we will study a system where backscattering is completely suppressed: the Hall bar with fully open leads ($d = D$). With this parameter setting the scattering geometry takes the form of an infinite lead, which should be the ideal system to observe several Hall plateaus. Our numerical results depicted in Fig. 6.5 show

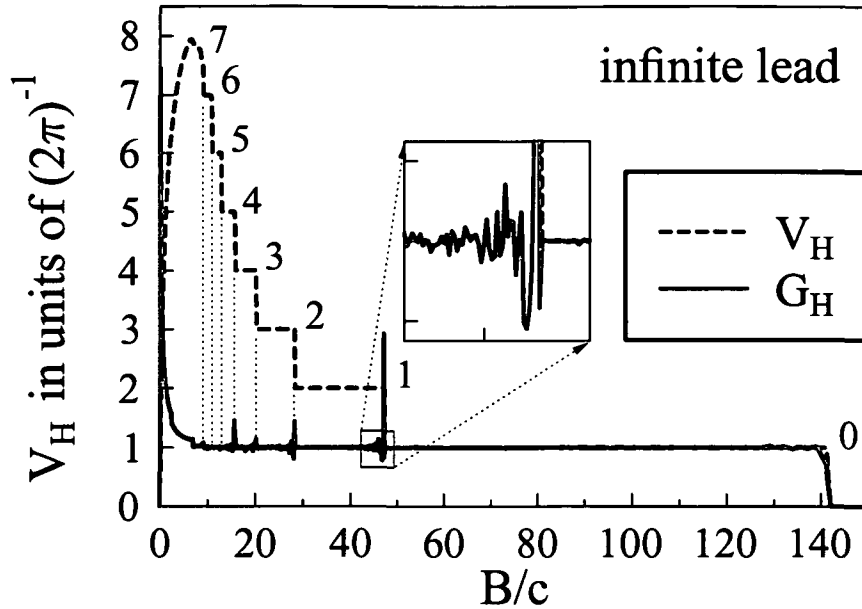


Figure 6.5: Hall voltage V_H and Hall conductivity G_H as a function of the magnetic field B in the infinite lead [101]. Lead width $d = 2.67$, chemical potentials $\mu_L - \mu_R = (2\pi)^{-1}$ and electron wave number $k_F = 10.1001\pi/d$. The steps in the plateaus of V_H and the corresponding peaks in G_H occur each at a critical magnetic field B_c^n (the integers $n = 0, \dots, 7$ are indicated at the corresponding steps). In the inset the oscillatory behaviour of G_H around $B = B_c^1$ is magnified.

indeed excellent agreement with these theoretical predictions: the plateau values of the Hall voltage stabilize at integer multiples of the first level, $V_H = n(\mu_L - \mu_R)/2\pi$. In the present case these levels are clearly visible for magnetic fields $B \gtrsim 10$. Below this value, the transverse quantization in the lead is mostly determined by the two confining walls and not so much by the magnetic field. The steps in the plateaus of V_H occur just at the critical magnetic fields B_c^n discussed earlier. In addition, at these points ($B = B_c^n$) the Hall conductivity G_H gives rise to peaks. In Fig. 6.5 these peaks are clearly visible. Note also the oscillatory behaviour just below the main peaks (see inset of Fig. 6.5 for magnification).

Many of the above features correspond very well to the observations in Hall measurements for real semiconductor samples. However, to allow for a quantitative comparison of our results with the experiments, we have to keep in mind that multi-electron effects as well as random potential scattering would have to be added to our theory. In the next section we show how the latter of these two modifications can be included in the MRGM.

6.4 Disorder potentials

To simulate scattering in a Hall bar more realistically, we include a disorder potential with non-zero spatial correlation into the tight-binding Hamiltonian of our system

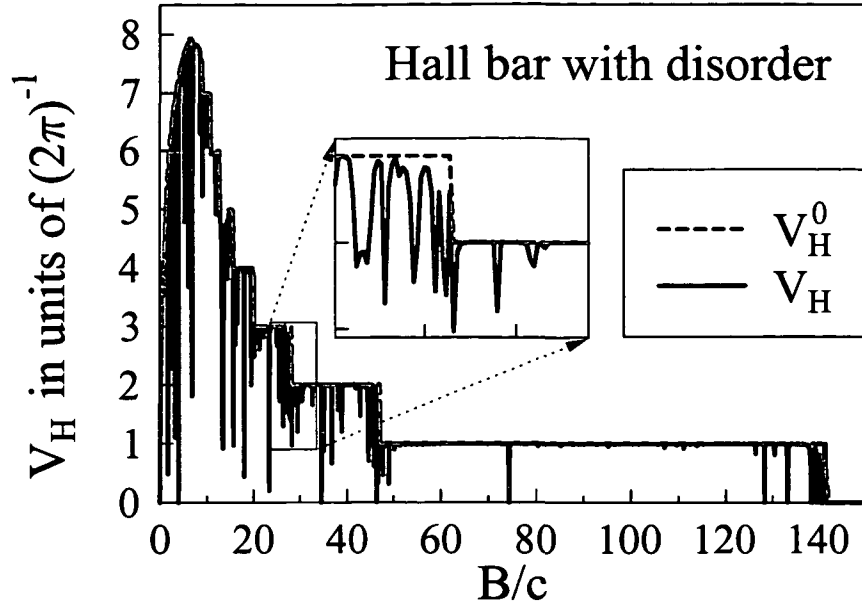


Figure 6.6: Hall voltage in the Hall bar with disorder (V_H , blue solid line) and with flat potential (V_H^0 , red dashed line) [101]. Correlation strength constant $C = 1$, disorder amplitude $A = 0.6$. All other system parameters are equivalent to Fig. 6.5. The Hall plateau values and positions of the steps are the same for both curves. However, the disorder potential leaves sharp dips superimposed on the Hall voltage stepfunction (see inset for magnification). These dips are relatively stable with respect to different realizations of the disorder potential (see Fig. 6.7).

[101]. Practically speaking, this amounts to the inclusion of a small random variation in each lattice site energy. In order for the MRGM still to work, this disorder potential must however preserve the separability within the modules. In the case of the rectangular module constituting a Hall bar geometry we therefore fix the random surface to depend only on the y -coordinate. The site energy in the Cartesian lattice [Eq. (2.3)] then takes the form

$$\varepsilon_j \longrightarrow \varepsilon_j + V^d(j). \quad (6.12)$$

For the disorder potential V^d we use correlated random distributions. These are calculated by an algorithm similar to the one presented in [106], adapted to our quasi one-dimensional potential V^d . The correlated random numbers $\eta_j^{(i)}$ are calculated iteratively by

$$\eta_j^{(i)} = \frac{\eta_{j-1}^{(i)} + \eta_j^{(i-1)}}{2} + 2e^{-C} \gamma_j^{(i)}, \quad (6.13)$$

where i is the iteration index, j the site index and $\gamma_j^{(i)}$ is a set of uniformly distributed random numbers $[-1, 1]$, calculated anew for every i . We start the iterative procedure with $\eta_j^{(0)} = 0, \forall j$. If in the iteration $\eta_j^{(i)}$ falls outside of $[-1, 1]$, it is backreflected by $\eta_j^{(i)} \rightarrow \pm 2 - \eta_j^{(i)}$. The parameter C controls the strength of the correlation by exponentially suppressing the uncorrelated random numbers. Finally

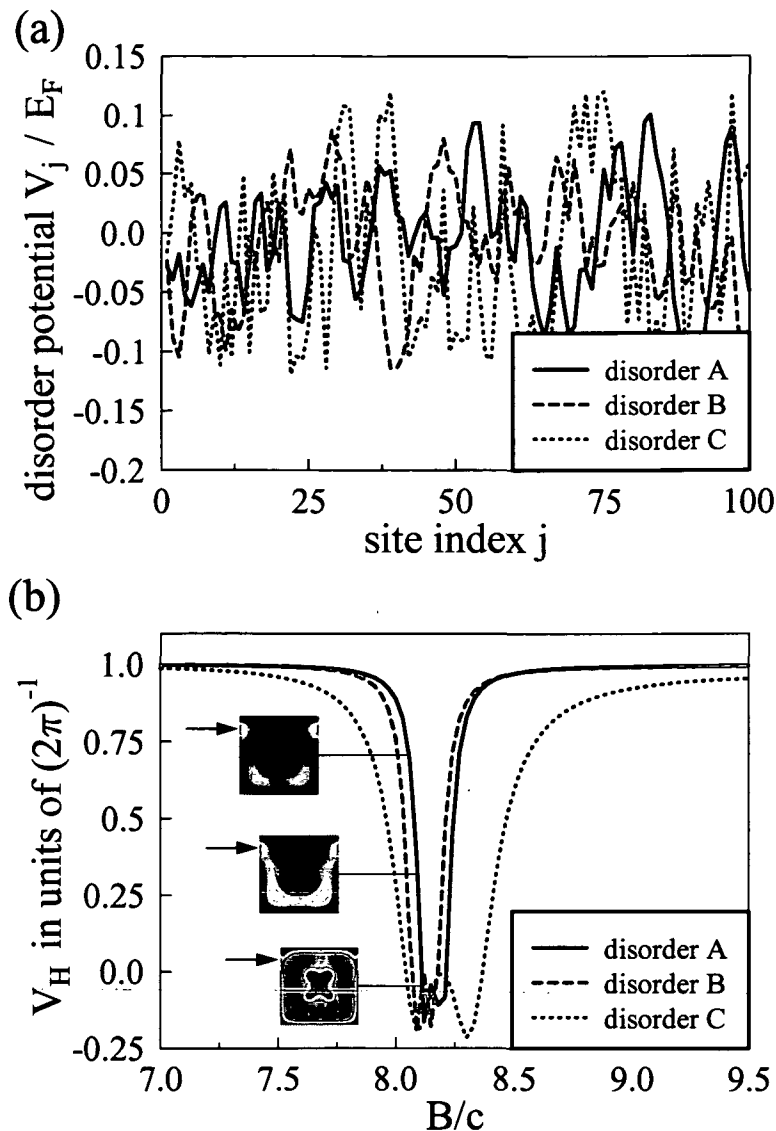


Figure 6.7: (a) Segment of three different realizations A, B, and C of a disorder potential V_j^d as a function of the site index j in y -direction of the Hall bar [101]. The data is shown in relation to the Fermi energy ($E_F = k_F^2/2$ with $k_F = 3.1\pi/d$). The lead width d is here equal to the cavity width D . (b) One antiresonance in the lowest plateau value of the Hall voltage is shown for the three different disorder potentials depicted in (a). The insets contain the corresponding wavefunction plots $|\psi(x,y)|^2$ in the region of disorder A. The black arrows indicate the position of the edge state when entering the disorder region.

we multiply the resulting distribution with a coupling constant A in order to control the strength of the disorder potential $(V_j^d)^{(i)} = A\eta_j^{(i)}$. The correlation between these random numbers can be characterized by the autocorrelation function and the mean

square amplitude,

$$K(n) = \langle V_j^d V_{j+n}^d \rangle = \frac{1}{N-n} \sum_{j=1}^{N-n} V_j^d V_{j+n}^d, \quad (6.14)$$

$$\langle (V^d)^2 \rangle = \frac{1}{N} \sum_{j=1}^N (V_j^d)^2. \quad (6.15)$$

- When including disorder into our numerical model for the Hall bar, we note that for moderate disorder strength A the Hall voltage neither changes its plateau values nor the positions of its steps. This result gives already some indication of the stability of the Hall voltage in real semiconductor samples [35]. However, within the Hall voltage plateaus we observe strong dips, which seem to occur at well defined magnetic fields (see Fig. 6.6). At low disorder strength these antiresonance features arise in rather narrow windows of the magnetic field. With increasing mean square amplitude of the disorder potential, these windows do however become larger and more frequent. Keeping the potential strength A fixed, but choosing for a different sampling of the random potential, we note that the peak positions do not change significantly, as long as the amplitude A is well below the Fermi energy. This behaviour is illustrated in Fig. 6.7 where we show (a) three different samples of the random potential and (b) one isolated antiresonance in the Hall voltage V_H , corresponding to each of the random potentials. We also observe that the correlation length of the disorder potential does not seem to influence the shape of the dips very strongly, as long as it stays below the electron wavelength λ_F (not shown). Finally, to explain the origin of the antiresonances we evaluate the scattering wave functions at the corresponding magnetic fields (see insets of Fig. 6.7). It can then be seen that the antiresonances are caused by a coupling of the incoming lead states to eigenstates which “live” in the region of the random potential. Similar resonance behaviour stemming from localized eigenstates are also reported in the literature [107, 108].

Chapter 7

De Haas-van Alphen oscillations

The de Haas-van Alphen (dHvA) effect is a phenomenon which is observed in very clean metal samples at very low temperatures and high magnetic fields [36]. Under these conditions the magnetic moment μ of the metal oscillates as a function of the magnetic field.¹ These oscillations, which are periodic as a function of $1/B$, are determined by the configuration by which the electrons of the system fill the N lowest Landau levels in the metal. With growing field strength B the degeneracy of these levels is increasing, as a result of which more electrons can fill the lower lying Landau levels. With growing field B there are magnetic threshold values B_i , where the quantum number of the highest lying level decreases by one. At these critical magnetic fields a jump in the derivative of the total system energy E^{tot} occurs. The magnetic moment of the system $\mu = -\partial E^{\text{tot}}/\partial B$ therefore shows discontinuous steps at these points B_i . Since the dHvA effect is due to the Landau quantization of a free electron gas, any thermal excitation blurs these oscillations.

The dHvA effect does not only occur for free electrons, but also in confined systems like in two-dimensional quantum dots and rings. When such a confining boundary is introduced, several additional phenomena do occur, as was studied in [109–112]. These additional contributions are due to the presence of edge states in systems with a boundary. In a non-confined electron gas these states are absent and all energy eigenstates take the eigenvalues of the discrete bulk Landau levels, $E_n = (n + 1/2)B/c$. The edge state energies E_{kn} , however, lie in between these values and can therefore mediate transitions between bulk levels. When plotting e.g. the energy eigenvalues of the tb Hamiltonian in a circular module as a function of the magnetic field, these edge state transitions can be well observed (see Fig. 7.1).

In the following calculation we require the observable of the total system energy E^{tot} for a number of N electrons in a given module (like the circle). It is calculated as the sum over the N minimum energy eigenvalues of the tb Hamiltonian for this module, $E^{\text{tot}}(B) = \sum_{k,n} E_{k,n}^{\text{min}}(B)$. In these considerations spin effects due to Zeeman splitting are not included. The magnetic moment μ is then derived as $\mu(B) = -\partial E^{\text{tot}}/\partial B$. In Fig. 7.2 both observables (E^{tot}, μ) are plotted as a function of the magnetic field B . Regarding μ , we first note that in the dHvA oscillations

¹Similar oscillatory behaviour as in the dHvA effect is not only observed in the susceptibility, but also in the conductivity and is then termed *Shubnikov-de Haas effect*.

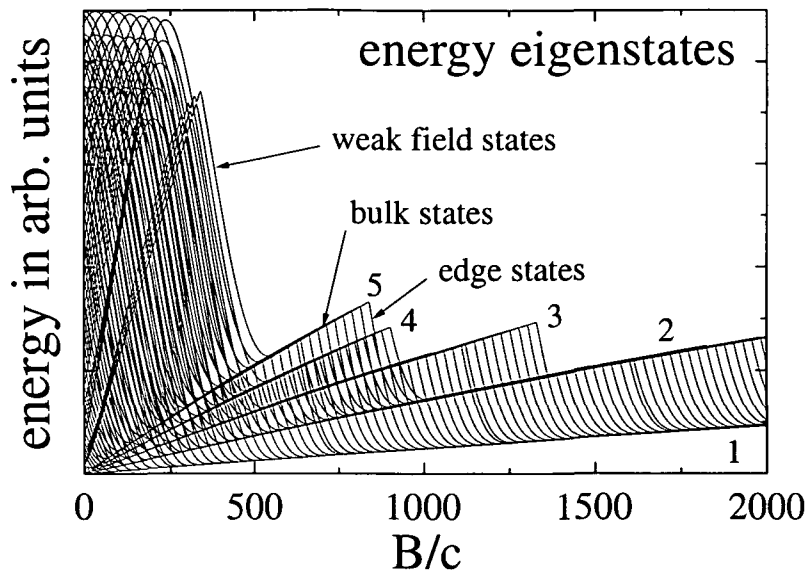


Figure 7.1: Energy $E_{kn}(B)$ of eigenstates in a circular tb module [see Fig. 2.4 and Eq. (2.35)] as a function of the magnetic field B . Only some states belonging to the lowest five Landau levels $n \in [1, \dots, 5]$ are displayed (see indicated numbers). Note the linearly increasing energy dependence of the bulk states and the transitions between them (mediated by edge states). At low magnetic fields the energy of the states is mainly determined by the finite size of the quantum dot.

the discontinuous steps at the threshold magnetic fields $B = B_i$ are smoothed out due to the edge state transitions.² However, the period of the oscillations, $\Delta_1 = B_i^{-1} - B_{i+1}^{-1}$, stays constant over a very large range of B , as for the unbounded systems. We further point out that the breaking of the bulk state degeneracy by the edge states leads also to additional fluctuations with high frequency and small amplitude, superimposed on the signatures of the dHvA effect. The origin of these contributions can be subdivided into two classes. The first class of oscillations is reminiscent of the Aharonov-Bohm (AB) effect, where each period Δ_2 corresponds to one edge state per occupied Landau level crossing the Fermi energy. Since the contribution of edge states to the total magnetization is considerably larger than that of bulk states, these transitions lead also to oscillations in the total magnetization μ [109, 112]. Due to the confinement of edge states to the region close to the boundary, their dependence on the magnetic field is approximately AB type. Since the AB effect is periodic in B and the dHvA effect is periodic in $1/B$ the number of AB oscillations superimposed on one period of the dHvA oscillations is growing rapidly with increasing field strength (see Fig. 7.2b). The second class of oscillations (with period Δ_3) was first discussed in [109] and is related to correlations between different Landau levels. Consider that close to a boundary the degenerate bulk states split into a ladder of equally spaced edge states E_{kn} (with spacing Δ_E). By increasing the

²We note parenthetically, that the threshold fields B_i are different from the previously introduced critical magnetic fields B_c^i .

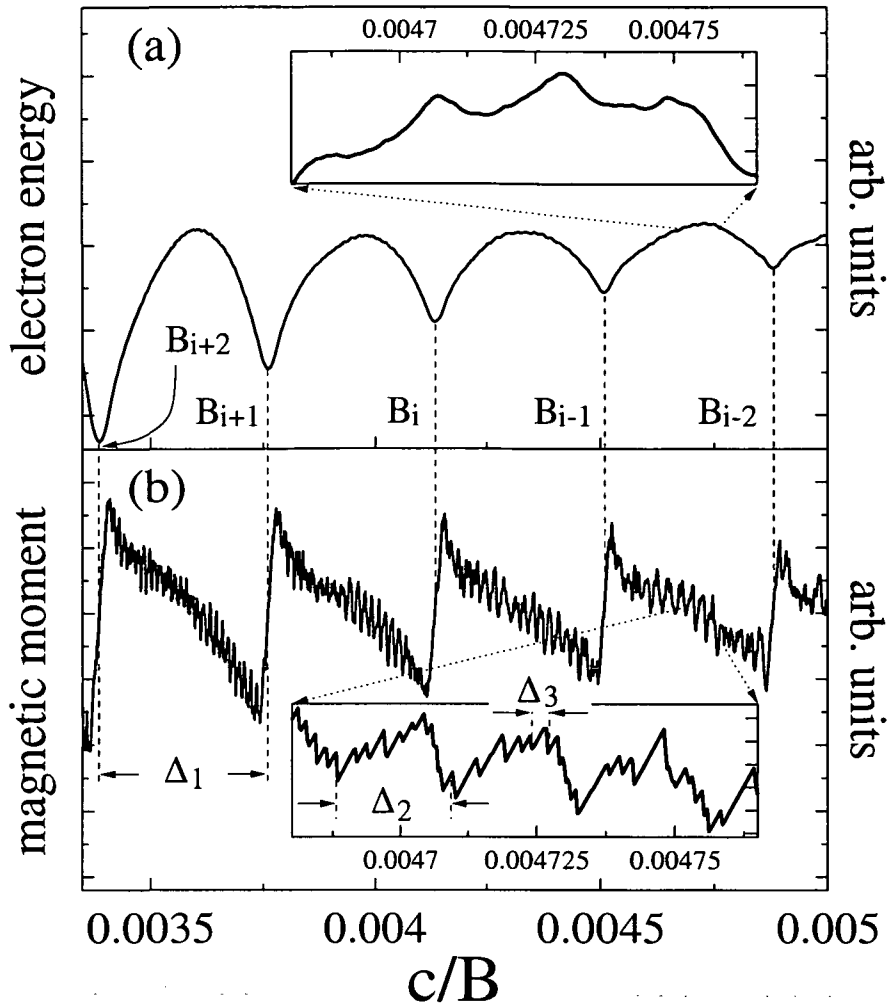


Figure 7.2: (a) Total electron energy of the 3000 lowest lying energy eigenstates in the circular module, $E^{\text{tot}}(B) = \sum_{k,n} E_{k,n}^{\text{min}}(B)$. To underline the periodicity of the oscillations in E^{tot} , the data are plotted here as a function of c/B . Note the dips in E^{tot} at the threshold fields B_i . (b) Magnetic moment of the circular module $\mu = -\partial E^{\text{tot}}/\partial B$. The $dH\nu A$ oscillations as a function of B^{-1} possess a constant period $\Delta_1 = B_i^{-1} - B_{i+1}^{-1}$. The presence of edge states in confined systems causes the discontinuous steps at B_i to be smoothed out and gives rise two additional types of fluctuations (see insets). These are superimposed on the large-scale $dH\nu A$ oscillations with periods Δ_2 , Δ_3 . Details are given in the text.

magnetic field B , all different ladders, belonging to different Landau levels n , are moving up in energy and change their spacing constant Δ_E . Whenever an edge state belonging to the bulk level n crosses the bulk level $n+1$, it thereby also crosses the minimum of the ladder $n+1$. Summing over the ladders for the calculation of the total energy $E^{\text{tot}}(B)$ therefore yields similar results at every one of these crossings. As a result we observe oscillations in $E^{\text{tot}}(B)$ and $\mu^{\text{tot}}(B)$, the period of which (Δ_3) is given by the difference between two adjacent crossings. It is important to note

however, that these oscillations are very much dependent on the particular boundary conditions chosen. In the case of hard wall boundaries discussed here, the edge state spectrum is very regular and so are the corresponding oscillations in the magnetic moment μ . In the case of smooth, non-harmonic boundaries a quite "noisy" signal is expected instead [109]. For completeness we mention that we are not aware of any experimental confirmation of this effect.

Chapter 8

Shot noise

In experiments dealing with quantum transport through microstructures, the electron conductance not only fluctuates as a function of parameters like the energy or the magnetic field, but also as a function of time. Apart from thermal effects, the origin of time-dependent fluctuations is related to the fact that an electric current corresponds to the flow of discrete electron charges (as opposed to a smooth fluidlike flow). In other words: the discrete number of electrons detected in the measurement apparatus shows statistical fluctuations around the average value of the electron current. These noise fluctuations, which are Gaussian and white, are called *shot noise* and were first theoretically analyzed by Walter Schottky in 1918 [113]. Schottky drew an analogy to the metal pellets in the charge of a hunting rifle, which gave the “shot effect” its name. Since the magnitude of fluctuations depends on the size of the pellets, this size can be determined by a measurement of the shot noise (provided that all pellets have the same size). In analogy, the quantum of the electron charge e can be derived from the mean square fluctuation in the electron current I at a frequency ω [113],

$$\langle \Delta I(\omega)^2 \rangle = 2e \langle I(\omega) \rangle \Delta\omega \quad (\text{in a.u. } e = 1). \quad (8.1)$$

The quantity $\Delta\omega$ is the noise frequency bandwidth and the brackets denote average values. The factor 2 comes from the positive and negative frequencies, which contribute identically. This formula also contains the quite intuitive result, that the relative fluctuations will be larger for smaller currents. From the mean square fluctuations $\langle \Delta I(\omega)^2 \rangle$ we can easily calculate the spectral density of the noise,

$$\tilde{S}(\omega) = \langle \Delta I(\omega)^2 \rangle / \Delta\omega. \quad (8.2)$$

Indeed this spectral density has e.g. been used in the experiment to measure the non-integer charge values implied by Laughlin’s theory of the fractional Hall effect [114, 115]. However, $\tilde{S}(\omega)$ not only carries information about the charge quantum, but also on the “particle” versus “wave” nature of a transport process [116]. In ballistic quantum transport experiments related phenomena have been investigated theoretically as well as experimentally [45, 117]. Furthermore it was discussed in the literature, whether shot noise also depends on the chaoticity of the dynamics inside

a scattering cavity [37, 44, 116, 118]. The present chapter is dedicated to the analysis of the above features.¹

8.1 Shot noise suppression

To explain the origin of shot noise, we consider a single particle which is scattered at a barrier (see also [37]). Let us assume that the particle arrives at the barrier with unit probability (i.e. the occupation number of the initial incident state is equal to 1). The particle is transmitted with probability T and it is reflected with probability $R = 1 - T$. We denote the occupation numbers of the transmitted and the reflected state by n_T and n_R respectively. Due to the quantization of charge, n_R and n_T can only be equal to 0 or 1 in each of the measurement processes. If the experiment is repeated a number of times, the average of the occupation numbers as well as deviations from the average value will follow binomial statistics. We use the notation $\delta n := \langle n \rangle - n$ and the relation $\langle n_T \rangle = 1 - \langle n_R \rangle$, which implies

$$\langle n_T \rangle^2 = \langle n_T \rangle - \langle n_R \rangle \langle n_T \rangle. \quad (8.3)$$

Knowing that for $n = 0, 1$ we have $n^2 = n$, the mean square of the deviation from the occupation number n_T can easily be calculated,

$$\langle (\delta n_T)^2 \rangle = \langle n_T^2 \rangle - \langle n_T \rangle^2 = \langle n_R \rangle \langle n_T \rangle = (1 - T)T = RT. \quad (8.4)$$

Such fluctuations, which are called *partition noise*, are proportional to both the transmission as well as the reflection amplitude. For the particular cases of $T = 0, 1$ the partition noise vanishes.

Instead of a barrier, let us now consider a quantum dot with an arbitrary number of leads. For the current in a narrow energy interval dE we have: $dI = (2\pi)^{-1} n(E) dE$. If we again denote the deviations of the average value by $\delta I := \langle I \rangle - I$, the correlation function of the current $I(t)$ in the leads a and b reads

$$S_{ab}(t - t') := \langle \delta I_a(t) \delta I_b(t') \rangle. \quad (8.5)$$

If the current is defined as a quantum mechanical operator $\hat{I}(t)$, one uses a symmetrized definition [37],

$$\hat{S}_{ab}(t - t') := \frac{1}{2} \langle \delta \hat{I}_a(t) \delta \hat{I}_b(t') + \delta \hat{I}_b(t') \delta \hat{I}_a(t) \rangle. \quad (8.6)$$

Unless there are time-dependent external fields, the correlation function is a function of $\Delta t := t - t'$ only.

The current $I(t)$ is determined by the difference in the occupation numbers n^+ and n^- of left- and right moving carriers in channel n [37],

$$\begin{aligned} I(t) &\propto \sum_n \int dE (n_n^+(E, t) - n_n^-(E, t)), \\ I(t') &\propto \sum_n \int dE' (n_n^+(E', t') - n_n^-(E', t')). \end{aligned} \quad (8.7)$$

¹For an introduction and overview of the field of *shot noise* we refer to [119] and [37], respectively.

Instead of the variable E' we can use $\omega := (E - E')$. The Fourier-transform of the current-current correlation function $\tilde{S}(\omega)$ is referred to as the power spectrum.

In a real experiment, part of the measured noise is always due to thermal fluctuations, but even in the zero-temperature limit some noise remains, although the Fermi distribution in each reservoir is then a step function. This remaining part of noise, which is due to the discreteness of the electron charge, is called *shot noise*. It is usually evaluated as the zero frequency limit of the power spectrum $S = \lim_{\omega \rightarrow 0} \tilde{S}(\omega)$. In the case of a two-terminal conductor (one incoming and one outgoing lead) the shot noise is [120–122]

$$S = \frac{|V|}{\pi} \text{Tr} (r^\dagger r t^\dagger t) = \frac{|V|}{\pi} \text{Tr} [(1 - t^\dagger t) t^\dagger t], \quad (8.8)$$

where V is the voltage applied between the incoming and the outgoing lead. The above equation can be conveniently transformed into the basis of eigen-channels, since the matrices $r^\dagger r$ and $t^\dagger t$ are diagonalized by the same transformation matrix. With the help of the eigenvalues T_n (R_n) of the product $t^\dagger t$ ($r^\dagger r$) we have,

$$S = \frac{|V|}{\pi} \sum_{n=1}^N (1 - T_n) T_n = \frac{|V|}{\pi} \sum_{n=1}^N R_n T_n. \quad (8.9)$$

The above formula reflects the result obtained for *partition noise* in Eq. (8.4): each eigenchannel contributes to noise in the same way as a single particle scattered at a barrier. Due to the independence of fluctuations in different channels, their contributions can simply be summed up. Note that the shot noise S , just like in the very simple model presented at the beginning of this section, vanishes in the cases of full transmission or full reflection. The upper limit of the shot noise S is reached for the *Poisson value*, discussed by Schottky [see Eq. (8.1)],

$$S_P = \frac{|V|}{\pi} \text{Tr} (t^\dagger t) = \frac{|V|}{\pi} \sum_{n=1}^N T_n = 2 \langle I \rangle. \quad (8.10)$$

This limiting value is expected for a Poissonian process of uncorrelated electrons. However, due to the Pauli principle, electrons in thermal equilibrium are correlated according to Fermi statistics and noise is strongly suppressed. This suppression is described by the term $(1 - T_n)$ in Eq. (8.9), since without it we would have $S = S_P$. The ratio of S to S_P is called "shot noise suppression factor" or *Fano factor*,² usually denoted by F and given by

$$F = \frac{\text{Tr} (r^\dagger r t^\dagger t)}{\text{Tr} (t^\dagger t)} = \frac{\sum_n (1 - T_n) T_n}{\sum_n T_n}. \quad (8.11)$$

The largest contribution to shot noise comes from eigenvalues around 1/2. In the limit of low transmission $T_n \ll 1$ in *all* eigenchannels n , the Fano factor F goes

²The term *Fano factor* (i.e. the shot noise suppression factor) goes back to a work by Ugo Fano on the statistics on ionization [123], but should not be confused with any of the terms used in the context of *Fano resonances*, going back to the same author.

to 1. Using random matrix theory (RMT), it is possible to calculate the expected eigenvalue distribution function for cavities with chaotic classical dynamics. If a cavity is chaotic and the transmission is symmetric in the sense that $\langle T \rangle = \frac{1}{2}$, then RMT yields the following distribution function of eigenvalues T [37],

$$P^{\text{RMT}}(T) = \frac{1}{\pi \sqrt{T(1-T)}}. \quad (8.12)$$

With the help of this function, one can calculate the expectation value of the transmission probability,

$$\langle T \rangle = \left\langle \sum_{n=1}^N T_n \right\rangle \approx N \int_0^1 dT P^{\text{RMT}}(T) T = \frac{N}{2}. \quad (8.13)$$

For the expectation value of the Fano factor we have,

$$\langle F \rangle = \left\langle \frac{\sum_{n=1}^N T_n(1-T_n)}{\sum_{n=1}^N T_n} \right\rangle. \quad (8.14)$$

The above equation can be easily evaluated,

$$\langle F \rangle = \frac{\left\langle \sum_{n=1}^N T_n(1-T_n) \right\rangle}{\left\langle \sum_{n=1}^N T_n \right\rangle} \approx \frac{N \int_0^1 dT P^{\text{RMT}}(T) T(1-T)}{\langle T \rangle} = \frac{1}{4}. \quad (8.15)$$

This value is known as the characteristic Fano factor for chaotic cavities. The value of 1/4 is, however, not always realized. Moreover, the deviation from 1/4 contains important information about the specific circumstances under which transport takes place. Interestingly enough the Fano factor depends on how “quantum” or “classical” the transport process through a scattering cavity is. Take e.g. the example of a classical particle, which is either fully transmitted or fully reflected when transported through a system. It has been claimed [116] that in the “classical limit” of the quantum transport problem, each of the N eigen-channels shows the same behaviour as the classical particle and is either fully reflected ($T_n = 0$) or fully transmitted ($T_n = 1$). If additionally the total transmission is equal to the total reflection $\langle R \rangle = \langle T \rangle = N/2$, we have an eigenvalue distribution function of the form

$$P^{\text{cl}}(T) = \frac{1}{2} [\delta(T) + \delta(T-1)]. \quad (8.16)$$

As is easily checked with Eq. (8.15) this “classical” eigenvalue distribution function implies a vanishing Fano factor ($F = 0$) and therefore a complete suppression of shot noise ($S = 0$).

In the following section the above predictions will be compared with numerical results for transport through the stadium, circle and rectangle billiard. The calculations were performed using the MRGM. To study the chaotic versus regular behaviour of the Fano factor these prototype geometries are very suitable. However, to study the “classical limit” of shot noise suppression, a tunable scattering geometry is introduced, which allows to vary the particle dwell time in the cavity. “Classical” and “quantum” transport are then realized for short and long dwell times respectively.

8.2 Numerical results

For a test of the RMT predictions we evaluated the transmission and reflection matrices of the stadium, circle and rectangular billiards (see Fig. 2.1) at a large number of different Fermi wavenumbers k_F (at zero magnetic field) [55, 124]. In each mode-interval (i.e. in $k_F \in [n, n+1]\pi/d$) the reflection and transmission matrices have been calculated at 200 equidistant points. Transport through the circular and rectangle billiard with both lead orientations has been analyzed in a momentum range of $k_F \in [1, 30]\pi/d$. Due to the larger numerical effort, the k_F -range for the stadium billiards is more limited, $k_F \in [1, 15]\pi/d$. The total transmission and

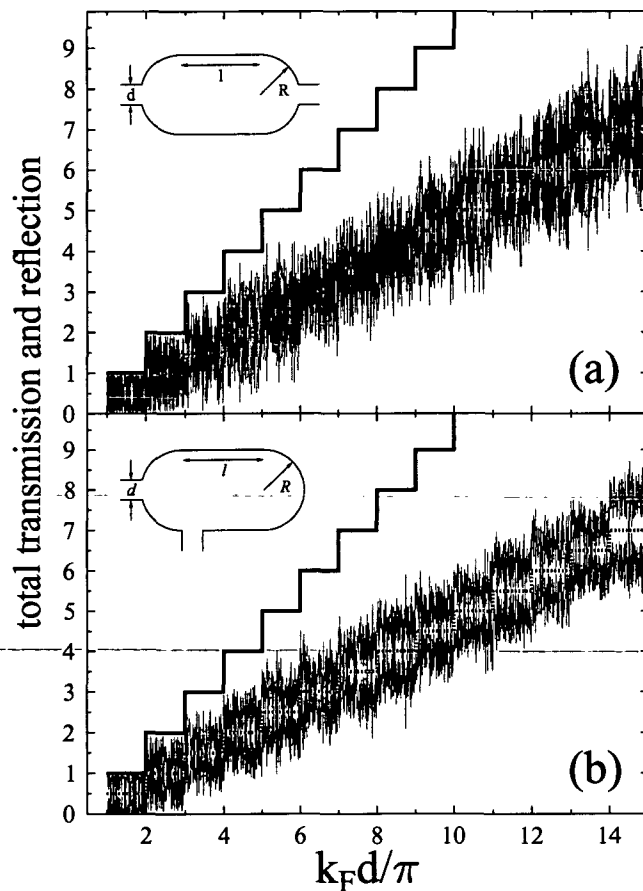


Figure 8.1: The total transmission probability $T^{\text{tot}} = \sum_{n,m} |t_{nm}|^2$ (blue line) and reflection probability $R^{\text{tot}} = \sum_{n,m} |r_{nm}|^2$ as a function of the wave vector k_F in (a) the stadium with opposite leads and (b) with perpendicular leads. The upper staircase function, $T^{\text{tot}} + R^{\text{tot}} = N$ (solid line) represents the quantum current conservation condition and indicates the number of open lead modes N . The lower staircase function at $N/2$ (dotted line) represents the value where transmission and reflection are equal, $T^{\text{tot}} = R^{\text{tot}} = N/2$.

reflection through these devices is depicted in Figs. 8.1, 8.2 and 8.3. We note that the fluctuations as a function of k_F are larger for regular dynamics in a cavity (for details see [55]). Accordingly, the stadium with perpendicular lead orientation shows the smallest amplitude in the fluctuations since there the contribution from non-universal paths is smallest. We further note that the condition of equality between transmission and reflection $\langle T^{\text{tot}} \rangle = \langle R^{\text{tot}} \rangle = N/2$ is only approximately realized in all of the systems considered. For the “chaotic” stadium billiards the fulfillment is somewhat better than in the “regular” cavities. The mismatch between total transmission and reflection is largest for the rectangular billiard with perpendicular leads. There the right cavity wall directly reflects a large fraction of the incoming flux back into the entrance lead, as a consequence of which $R^{\text{tot}} > T^{\text{tot}}$.

Let us consider next the Fano factor averaged over 200 points in each mode-interval

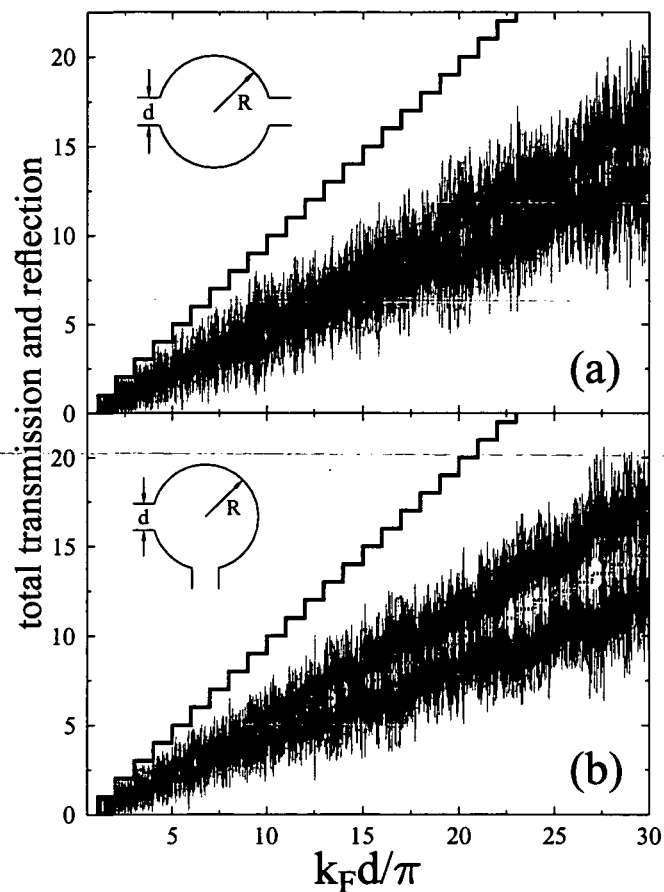


Figure 8.2: As in Fig. 8.1 but for (a) the circle with opposite leads and (b) with perpendicular leads.

n according to

$$\langle F(n) \rangle := \frac{\int_{\frac{n\pi}{d}}^{\frac{(n+1)\pi}{d}} dk \sum_{i=1}^n T_i (1 - T_i)}{\int_{\frac{n\pi}{d}}^{\frac{(n+1)\pi}{d}} dk \sum_{i=1}^n T_i}. \quad (8.17)$$

This function $\langle F(n) \rangle$ is plotted in Fig. 8.4 for all three geometries and both lead orientations. Surprisingly, all the six presented cases give Fano factors close to the RMT prediction of $1/4$. The most pronounced deviations from this value are discernible at low mode numbers. The explanation for this is that for low mode numbers the relative mismatch between R^{tot} and T^{tot} is largest. Particularly for the cases of the 90° -stadium and 90° -rectangle, this deviation at low mode numbers is most pronounced (see Figs. 8.1b and 8.3b respectively). In the case of the regular cavities, the Fano factor can be observed to deviate slightly from $1/4$ in the

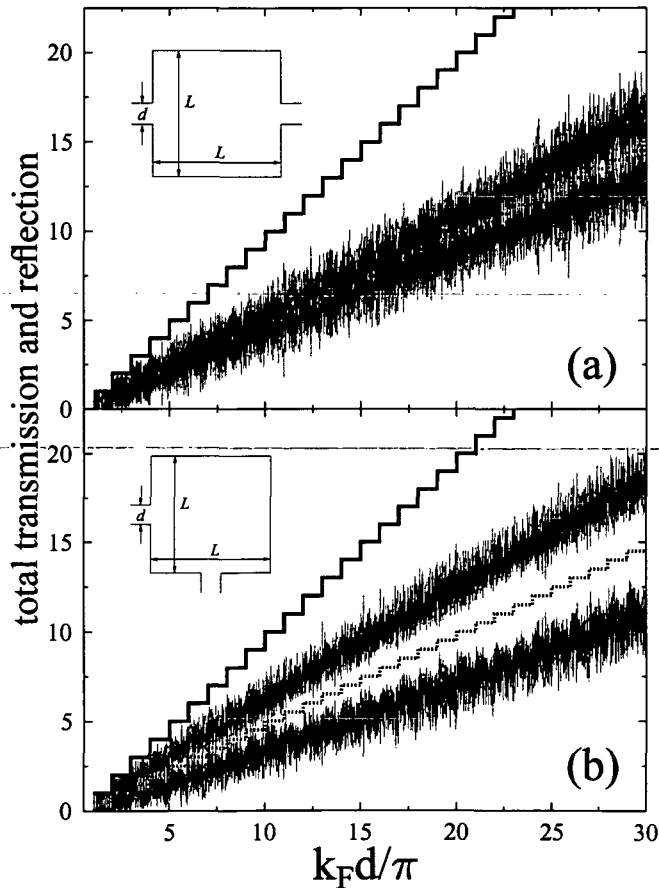


Figure 8.3: As in Fig. 8.3 but for (a) the circle with opposite leads and (b) with perpendicular leads.

high mode limit. This feature will be discussed below. For mode numbers around $n \in [10, 15]$ the averaged Fano factor $\langle F(n) \rangle$ is very similar for all the six geometries studied. From this observation we might conclude that the Fano factor is independent of whether chaotic or regular dynamics is governing the transport process. However, it has been claimed that billiard systems with regular classical dynamics show a shot noise suppression which is considerably stronger than for chaotic billiards [43, 44, 118]. This prediction is based on a reduced amount of diffraction due to the enhanced stability of trajectories in regular billiards. Without this diffraction the transport process could be expected to be more “deterministic” or “classical”,

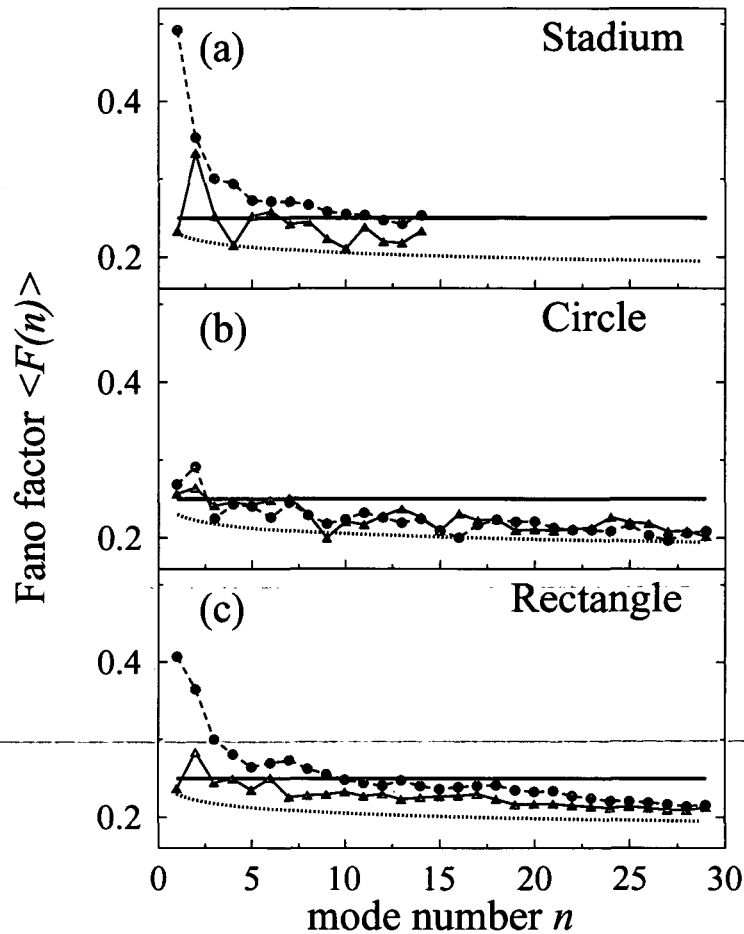


Figure 8.4: Fano factor $F(n)$ averaged over one-mode intervals for (a) the stadium, (b) the circle and (c) the rectangle billiards [124]. Green (red) circles (triangles) stand for 90° (180°) lead orientation respectively. Geometries and dimensions are as indicated in Fig. 2.1. In all the three figure parts the black solid line depicts the value from RMT ($1/4$) and the dotted line shows the predicted dependence of the Fano factor on the characteristic scattering times, $F = 0.25 \times \exp(-\tau_E/\tau_D)$. Note that for the evaluation of the dotted curve, the characteristic scattering times of the stadium were used [also in (b) and (c)]. We do not yet have an estimate for the dependence of F for the regular cavities.

with an eigenvalue distribution $P(T)$ shifted from the “quantum” value $P^{\text{RMT}}(T)$ in Eq. (8.12) towards the “classical” distribution $P^{\text{cl}}(T)$ given in Eq. (8.16). Along this quantum-classical transition the Fano Factor F should be reduced from $1/4$ towards 0. In our data shown in Fig. 8.4 such a characteristic difference between chaotic and regular dynamics is not visible in the Fano factor. Our interpretation of this result is, that the suppression of shot noise is not due to the *chaoticity* or *regularity* of the classical dynamics in these billiards. The Fano factor rather depends on the spread of the electronic wavepacket. Since “spreading” not only occurs in chaotic billiards but is due to the diffraction at the two lead mouths [74], also regular billiards like the circle or the rectangle can give rise to a Fano factor close to $1/4$. This consideration agrees with the observation in [118] that the Fano factor in the stadium billiard is drastically reduced if the electron is transmitted via a few whispering gallery states instead of exploring the whole chaotic phase space via many cavity states. Since in [74] was shown how to systematically include diffractive contributions into a semi-classical theory for quantum transport, the dependence of the Fano factor on these diffractive terms should be accessible for closer investigation. Further work along these lines is in progress [124].

An important feature of shot noise is that it is sensitive to the *dwelt time* τ_D , which measures the time during which the electron stays inside the cavity. For a chaotic cavity with area A^{dot} and two leads of width d attached to it, τ_D is given by the following expression,

$$\tau_D = \frac{A^{\text{dot}} \pi}{2 d v_F}. \quad (8.18)$$

This formula can be derived by assuming that in a chaotic cavity all points at the boundary are, on average, hit with equal probability by a trajectory [125, 126].

The shot noise power is expected to depend on whether τ_D is long or short compared to the *Ehrenfest time* τ_E (also called: *quantum break time*). The quantity τ_E is given by the time during which a wave packet of minimal size spreads over the whole scattering cavity. For a chaotic cavity this translates into

$$\tau_E = \alpha^{-1} \ln \left(\sqrt{A^{\text{dot}}} / \lambda_F \right). \quad (8.19)$$

with α being the Lyapunov exponent of the classical dynamics in the cavity. For the stadium billiards the exponent $\alpha \approx 0.45 \times v_F$ [127, 128]. In terms of these two time scales, the Fano factor is predicted to show an exponential suppression [116] according to,

$$F = \frac{1}{4} \exp(-\tau_E/\tau_D). \quad (8.20)$$

In the “quantum limit” of long dwell times ($\tau_D > \tau_E$) the RMT-value of $1/4$ is realized. In the case of many open lead modes - i.e. in the “classical” limit of short dwell times ($\tau_D < \tau_E$) - the Fano factor is exponentially reduced. In a recent experiment [45, 117] a behaviour which agrees qualitatively with Eq. (8.20) was indeed observed. To check whether the predicted shot noise suppression is also visible in the systems considered here, we reconsider Fig. 8.4a where the numerical data is compared to Eq. (8.20) (plotted as a black dotted curve). In view of the predicted slow decrease

of the Fano factor as a function of the wavenumber k_F , the limited range of our calculations (up to 15 open modes) prevents a quantitative comparison in the high-mode limit. On the other hand, the range of the data for the regular billiards in Fig. 8.4b,c is larger (up to 30 open modes) and a decrease of F for higher mode-numbers can indeed be observed there. Surprisingly, for $n > 10$ the data for the circle and the rectangle with both lead orientations give rise to Fano factors which are quite similar to each other. This fact might be a hint to a system-independent mechanism that suppresses shot noise also in regular quantum billiards. However, in these particular systems of circle and rectangle billiards neither the above definition for the dwell time Eq. (8.18) nor for the Ehrenfest time Eq. (8.19) can be applied. This is because in regular quantum billiards τ_D and τ_E are clearly dependent on the specific scattering dynamics. Only for long trajectories the spreading due to scattering at the lead mouths washes out the system specific details [74]. A formula for the k_F -dependence of this mechanism would therefore be very desirable and could provide an explanation for the decrease of F in Fig. 8.4b,c.

In this direction we performed a classical trajectory Monte-Carlo simulation for the rectangular and circular billiards. We find that the classical dwell time τ_D in these regular systems stays between 50-90% of the value of the dwell time in the stadium billiards [see Eq. (8.18)]. Since the Fano factor for our regular systems is not more strongly suppressed than in the case of the stadium, this result would point to the conclusion that the Ehrenfest-time τ_E for regular systems is also lower than for chaotic systems. Otherwise the suppression law Eq. (8.20) would give a much steeper decrease of the Fano factor for regular systems. It would however be quite surprising and counterintuitive if the Ehrenfest time turns out to be shorter for regular billiards than for chaotic ones. It will therefore be a topic for future investigation whether Eq. (8.20) is applicable at all for systems with regular dynamics. Work along these lines is in progress [124, 129, 130].

8.3 Distribution of transmission eigenvalues

In this section we try to gain further insight into the question why the Fano factors of regular and chaotic cavities are similar. Our starting point is to investigate the distribution function of the transmission eigenvalues T_n . As the stadium shaped billiards show chaotic classical dynamics, their distribution function $P(T)$ is predicted to be $P^{\text{RMT}}(T)$ as given in Eq. (8.12) in the limit $\tau_D \gg \tau_E$. Due to non-universal contributions the eigenvalue distribution function of regular billiards like the circle or the rectangle is usually expected to deviate from $P^{\text{RMT}}(T)$. However, since these billiards exhibit Fano factors which are similar to those of the stadium billiards, it is interesting to compare their eigenvalue distribution function with $P^{\text{RMT}}(T)$ as well. To obtain $P(T)$ we diagonalize the matrices $t^\dagger t$ and calculate their eigenvalues T_n . The range of eigenvalues $[0, 1]$ is split up into 50 equidistant intervals in order to bin the eigenvalues. For the stadium billiard a total number of $14 \times 200 = 2800$ eigenvalues has been evaluated in the k_F -interval $k_F \in [1, 15]\pi/d$. In the case of the circle and rectangle $29 \times 200 = 5800$ eigenvalues in the interval $k_F \in [1, 30]\pi/d$ were

calculated. Resulting distributions are shown in Fig. 8.5. Note that in all six cases, the eigenvalue distribution is quite close to $P^{\text{RMT}}(T)$. Since the distribution $P(T)$ determines the Fano factor by way of Eq. (8.15), the similarity between the Fano factors for all studied geometries obviously originates in the similar distribution of eigenvalues.

8.4 Tunable cavities

As mentioned above, the Fano factor F is predicted to show a strong dependence on the dwell time τ_D and the Ehrenfest time τ_E inherent in the scattering process. These two quantities do however change only very slowly as a function of the Fermi wavenumber k_F . As a consequence, only a slight shot noise suppression is observable in Fig. 8.4. To go beyond this numerical limit we turn to a setup that has recently

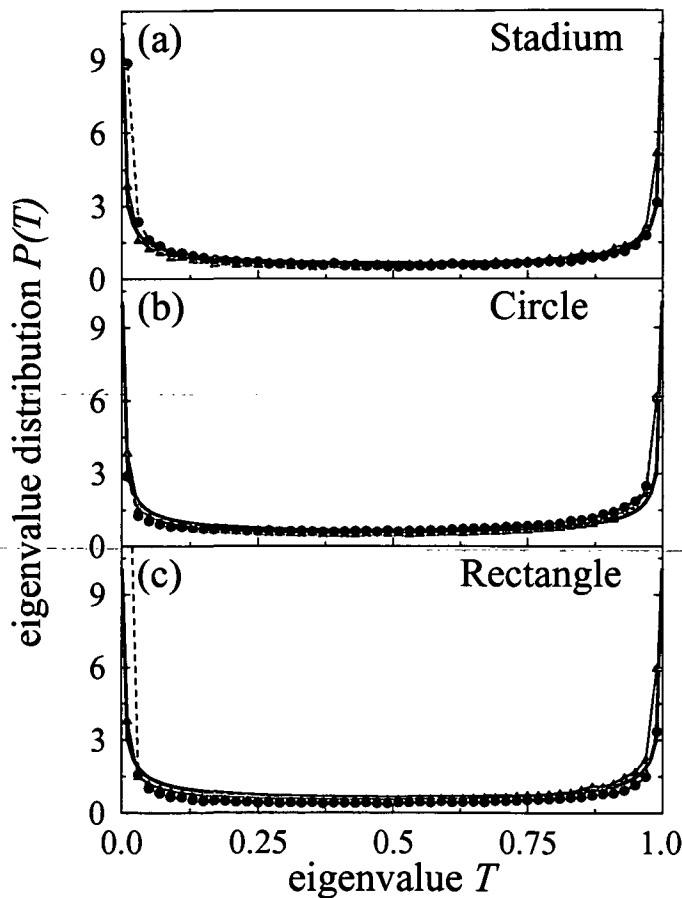


Figure 8.5: *Eigenvalue distribution $P(T)$ for (a) the stadium, (b) the circle and (c) the rectangle billiards [124]. Green (red) circles (triangles) stand for 90° (180°) lead orientation respectively. Geometries and dimensions are the same as indicated in Fig. 2.1. The RMT prediction for chaotic dynamics $P^{\text{RMT}}(T)$ is shown as a black solid line for all three geometries.*

been realized experimentally [45, 117]. The studied scattering device consists of a chaotic scattering cavity connected to two electron reservoirs via two tunable diaphragms. Although the cavity itself has rectangular shape in the experiment, the electron dynamics is chaotic due to random potential scattering. By changing the opening of the diaphragms the electron dwell time in the cavity τ_D can be tuned without changing the injection energy. This allows to study the τ_D -dependence of shot noise in detail.

To simulate the above experiment we consider here the scattering system depicted in Fig. 8.6. It consists of a cavity to which two leads are attached via tunable diaphragms. The cavity itself has the same height d as the leads and the distance between the two diaphragms is $2d$. Their openings are situated on top and bottom of the geometry to reduce direct scattering from one to the other. Between the diaphragms two quadratic modules with a y -dependent correlated disorder potential are attached to each other. In each module the randomness depends only on y , since an additional x -dependence would prevent us from directly using the MRGM. We note, however, that this limitation can be overcome [124]. On the other hand, separability within the cavity has to be destroyed to obtain truly chaotic dynamics. This is done by linking two modules with different disorder potentials. An efficient method to accomplish this goal is to calculate one module with disorder, to rotate it by 180° and to link the original module with the rotated one (see also Fig. 8.6). In this way the numerical effort is strongly reduced since only one module has to be computed.

The random disorder potential V_d is calculated as described in section 6.4. The

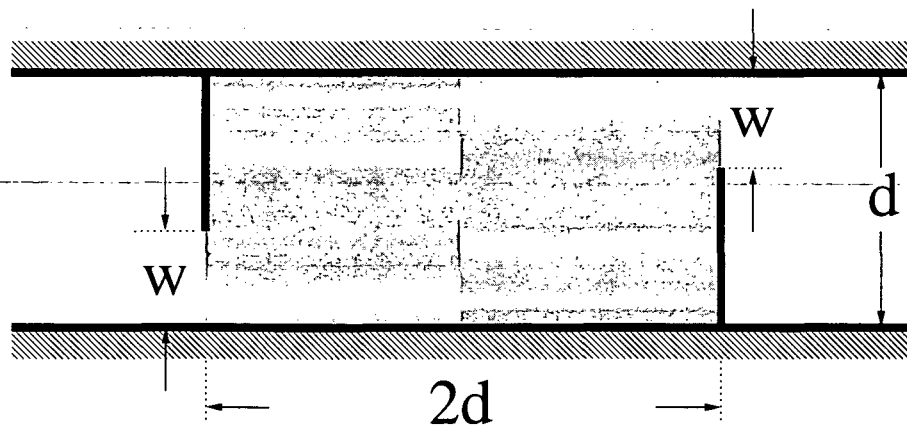


Figure 8.6: Scattering device with tunable diaphragms and cavity area $A^{\text{dot}} = 2d^2 = 4 + \pi$. By changing the openings $w \in [0, d]$, the electron dwell time in the cavity can be tuned without changing the electron energy E_F . The cavity region consists of two modules with a correlated disorder potential (see gray-shaded area). To save computing time, the second module contains the same random potential as the first one, but turned by 180° . In such a way the non-separability requirement for the combined modules is met, even though the disorder potential is only y -dependent in each module.

amplitude A of the disorder is determined by the following considerations: (1) If A is too large, the electron mainly stays inside the longitudinal "trenches" formed by our particular disorder potential and most of the electron flux will be reflected. (2) If A is not large enough, the electron will not be *randomized* sufficiently. Our aim is therefore to find an intermediate parameter regime where both objections (1) and (2) are removed. We are guided by the idea that the total transmission T^{tot} across two identical diaphragms must be

$$T^{\text{tot}} = T^{\text{dia}}/2, \quad (8.21)$$

in case that the cavity between the two diaphragms gives rise to chaotic dynamics and each diaphragm for itself allows for transmission T^{dia} [45, 117]. This is because the electron that enters into the cavity (with probability T^{dia}) has equal probability to exit either by the first or the second diaphragm due to the randomization. If we renormalize Eq. (8.21) by the total number of open lead modes N , we have

$$\frac{T^{\text{tot}}}{N} = \frac{T^{\text{dia}}}{2N} \approx \frac{w}{2d}, \quad (8.22)$$

After simulating different potentials and different opening ratios w/d , a potential strength $A = 0.1 \times E_F$ was chosen such that Eq. (8.22) is fulfilled (see also Fig. 8.7, where the corresponding data is shown).

When the diaphragms are strongly closed ($w \lesssim d/2$) the total transmission $\sum T_n$ is lower than the total reflection $\sum(1 - T_n)$, as a considerable part of the flux is already reflected back by the first diaphragm. Only a fraction of approximately w/d of the total flux passes through the first diaphragm. For this reason, the eigenvalue distribution $P(T)$ in our scattering device does not follow the symmetric distribution $P^{\text{RMT}}(T)$ shown in Eq. (8.12). A rather asymmetric distribution $P(T)$ is realized, especially in the case of $w \ll d$, where many eigenvalues $T \approx 0$ (not shown). Even though these large numbers of very low eigenvalues do not contribute substantially to the Fano factor as given in Eq. (8.11), they have the potential to alter the standard RMT result of a Fano factor $F = 1/4$, in spite of chaotic cavity dynamics. The decrease of F in the classical limit should however be unaltered by the asymmetry of $P(T)$. For the classical limit of $P(T)$ we have,

$$P_{(\text{as})}^{\text{cl}}(T) = a \delta(T) + (1 - a) \delta(1 - T), \quad \text{with } a \in (0, 1). \quad (8.23)$$

Note the difference to P^{cl} , defined in Eq. (8.16). Replacing $P^{\text{RMT}}(T)$ in Eq. (8.15) by $P_{(\text{as})}^{\text{cl}}(T)$ in Eq. (8.23), we obtain a complete shot noise suppression, i.e. a Fano factor $F = 0$, regardless of the value of the parameter a [see Eq. (8.15)]. For a rough estimate of the expected decrease of the Fano factor we use the previously discussed relation,

$$F = \frac{1}{4} \exp(-\tau_E/\tau_D). \quad (8.24)$$

The dwell time τ_D can again be estimated by Eq. (8.18), with the only difference that the diaphragm opening w has to be inserted instead of the lead with d . For the Ehrenfest time Eq. (8.19) could in principle be used. Unfortunately we do

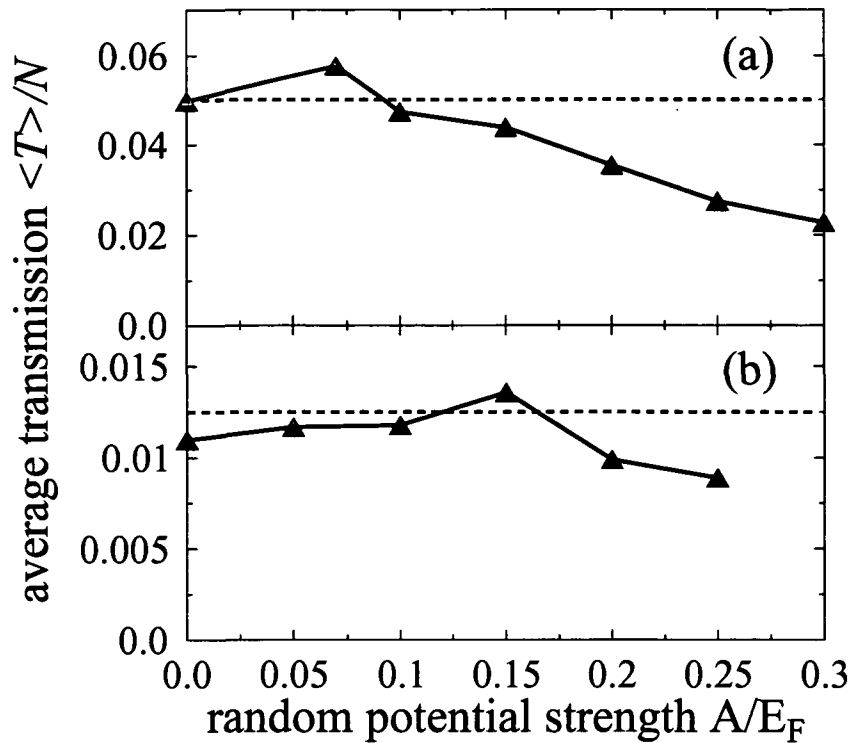


Figure 8.7: Renormalized average transmission probability $\langle T \rangle / N$ for different values of the random potential strength A [124]. The dimensionless correlation parameter C in Eq. (6.13) is set to 3 and the openings of the diaphragms are (a) $w/d = 0.025$ and (b) $w/d = 0.1$. The expected value for the optimal potential strength $\langle T \rangle / N = w/(2d)$ is indicated as a black dashed line. For very large values of A reflection dominates. Since at $A \approx 0.1 \times E_F$ a rather good agreement with the randomization condition is found, this value will be used in the following.

however not have a precise value for the Lyapunov exponent α available in our cavity. As a first order approximation we estimate that α for our tunable cavity is similar to the value in the stadium billiard: $\alpha \approx 0.45 \times v_F$. Inserting this value into Eq. (8.24), we get a rough estimate for the dependence on the Fano factor on the diaphragm openings w . In Fig. 8.8 this prediction is compared with numerical data and shows surprisingly good agreement. Fitting the numerical data with the function in Eq. (8.24) and α as the fitting parameter yields the best correspondence for $\alpha \approx 0.75 \times v_F$. Note that small openings (corresponding to large dwell times) lead to a relatively high Fano factor. Even though we have a quite asymmetric eigenvalue distribution function $P(T)$, the Fano factor for small diaphragm opening w is $F \approx 1/4$. For larger openings (smaller dwell times), the Fano factor decreases and follows the predicted exponential suppression.

Our results are also in close correspondence to experimental studies [45, 117]. This fact is particularly useful, since in contrast to the experiment, effects like impurity

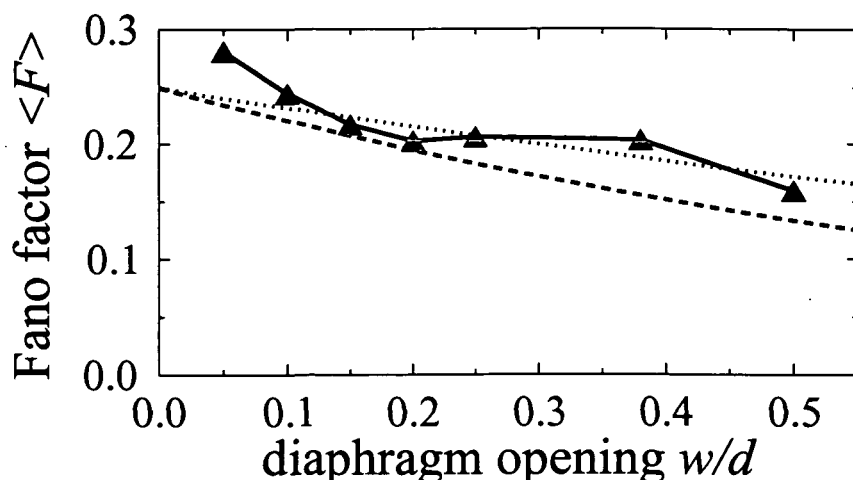


Figure 8.8: The Fano factor F as a function of the diaphragm opening w/d (red triangles), averaged over 30 different k_F values in the range $k_F \in [40, 41]\pi/d$ at a disorder potential strength $A \approx 0.1E_F$ [124]. The dashed black curve shows the decay due to the change in τ_D , $F = 0.25 \times \exp(-\tau_E/\tau_D)$, estimated with a Lyapunov exponent as in the stadium billiards, $\alpha \approx 0.45 \times v_F$. Fitting the numerical data yields a value of $\alpha \approx 0.75 \times v_F$, indicated by the dotted black curve.

scattering etc. can be excluded *a priori* in our theory. So far, the large computational effort involved in the numerical simulation of the quantum-to-classical crossover of shot noise has prevented a numerical test of the experiment. The results presented here should therefore be, to our knowledge, the first test of its kind. For completeness we mention that a dynamical model (“map”) has been introduced recently, which uses the kicked rotator to simulate chaotic scattering in a ballistic quantum dot [46]. This model also shows the predicted suppression of the Fano factor.

8.5 Future work

Future work on the subject of shot noise suppression will comprise a close investigation of the way in which the exponential shot noise suppression Eq. (8.24) changes in case of an asymmetric eigenvalue distribution $P(T)$. Another aim is to calculate more data points in Fig. 8.8, since it might then be possible to detect and, if confirmed, explain deviations from the exponential decay law in Eq. (8.24). As mentioned above, a formula is strongly desired for the k_F -dependence of the wavepacket spreading due to scattering at the open lead mouth [74]. A better approximation for the Ehrenfest time for regular billiards would thus become available. This would be particularly useful to describe shot noise suppression in quantum dots with regular classical dynamics.

Chapter 9

Weak localization

Transport through a classical resistor is well described by Ohm's law, according to which the resistance scales linearly with the length of the resistor. However, at low temperatures, where the coherence length of the electrons can be much larger than the mean free path, this linear scaling law breaks down. This is because in contrast to the behaviour predicted by classical transport theory, transmission in the regime of *quantum diffusion* is governed by elastic and inelastic scattering processes. If the electron coherence length is smaller than the whole sample size, we are in the regime of *strong localization*, first described by Anderson [131]. The quantum interference between many scatterers leads to a strong localization of the electrons (also called *Anderson localization*), where conductance through the sample is very much suppressed. If, on the other hand, the sample size is smaller than the coherence length, we are in what is called the *weak localization (WL) regime*. Here the transport process is governed by coherent (i.e. ballistic) electron motion and can be described with the Landauer-Büttiker formalism [51], as we did throughout this thesis.

A very prominent feature occurring in this regime is the so-called *weak localization effect*.¹ This phenomenon consists in a reduction of the mean value of conductance below the classical value. Among the first experimental investigations of this effect was the work published in [133], where conductance across thin wires was probed. A theoretical explanation for the *weak localization effect* is the following: In the Feynman picture of quantum theory transport is described by a sum over all possible paths which a particle can take from the initial to the final state. Each of these paths comes with an amplitude and a phase, both of which can be derived from the classical action along the path. Quantum transmission (reflection) is then calculated as the interference of all transmitted (reflected) paths. In contrast to the transmitted trajectories, all reflected paths interfere with their time-reversed partner. Since a trajectory and its time-reversed mirror image always come with the same phase (provided that no magnetic field is present), their interference will always be constructive, thus increasing the resistance as compared to the classical value. However, with a magnetic field in the sample, this enhancement of the resistance is reduced. That is because the magnetic field breaks the time-reversal symmetry by way of an Aharonov-Bohm phase, the sign of which is opposite for a trajectory and its time-

¹For an overview over the topic of weak localization see e.g. [18, 71, 132].

reversed partner. Consequently, the conductance increases with increasing B or equivalently the resistance decreases. This resistance peak around $B = 0$ has been subject to numerous investigations, both theoretical [13, 134–138] and experimental [1, 2, 38, 139]. Not only the height and width of the peak, but also its specific form was studied in detail. A very interesting feature in this context is the fact, that the WL peak line shape is predicted to be different for dynamical systems with either regular or chaotic dynamics. For chaotic cavities like the stadium [see Fig. 2.1c] theoretical investigations predict the peak to have a Lorentzian shape [135]. This result is determined by the rather randomly distributed trajectories in the stadium and the Aharonov-Bohm phases they acquire. In the experiment, the Lorentzian shape could indeed be found [38]. Furthermore, the measurement also showed that the line shape for a regular billiard like the circle [see Fig. 2.1a] follows a linearly decreasing triangular shape. This difference to the chaotic cavity can be explained by the conservation of angular momentum in the circle billiard. Due to this additional constant of motion, the trajectories in the circle acquire very large Aharonov-Bohm phases, leading to the triangular WL peak shape.

9.1 Numerical results and discussion

We now try to reproduce these experimental results for the circular quantum dot numerically. We calculate the total transmission T^{tot} and reflection R^{tot} at 600 equidistant k_F values in the interval $k_F = [2.2, 2.8] \times \pi/d$ and at fixed magnetic field B . An average over the 600 data points is done to smooth out non-universal contributions which blur the WL effect. Plotting the average values as a function of B around $B = 0$, we can expect to find the WL peak. The results obtained for the circle with 90° lead orientation are displayed by the solid line curves in Fig. 9.1 (other curves in the figure will be explained below). In parts (a) and (b) of Fig. 9.1 the WL peaks in the reflection and transmission are displayed. Figure (c) demonstrates the fulfillment of the unitarity requirement. Note that in Fig. 9.1a the expected linear decrease around $B = 0$ is indeed observable. Due to unitarity the WL effect leaves exactly the inverse peak in the total transmission as compared to the reflection.

Implicitly included in our calculations is the assumption of an infinite electron coherence length L_ϕ . This is because no dissipative or dephasing mechanism is present in our computation. In the experiment, however, these quantities play a crucial role, since they strongly affect the observability of the WL peak. As was shown in [38] a decrease of L_ϕ turns the triangular WL peak shape of the circle into a more Lorentzian shape, typical for chaotic cavities. This behaviour was demonstrated by repeating the WL measurements at different temperatures: The higher the temperature, the shorter the coherence length L_ϕ . As a consequence, the temperature allows to tune L_ϕ , above which length the trajectories involved in the transport process are suppressed. Since the area A and the magnetic field B enter the phase of the Feynman paths as conjugate variables (the classical action $S = kL - BA/c$), it is the long trajectories (i.e. those which acquire a large area A), which give rise to the steep incline at small magnetic fields B . By increasing the temperature, the longest

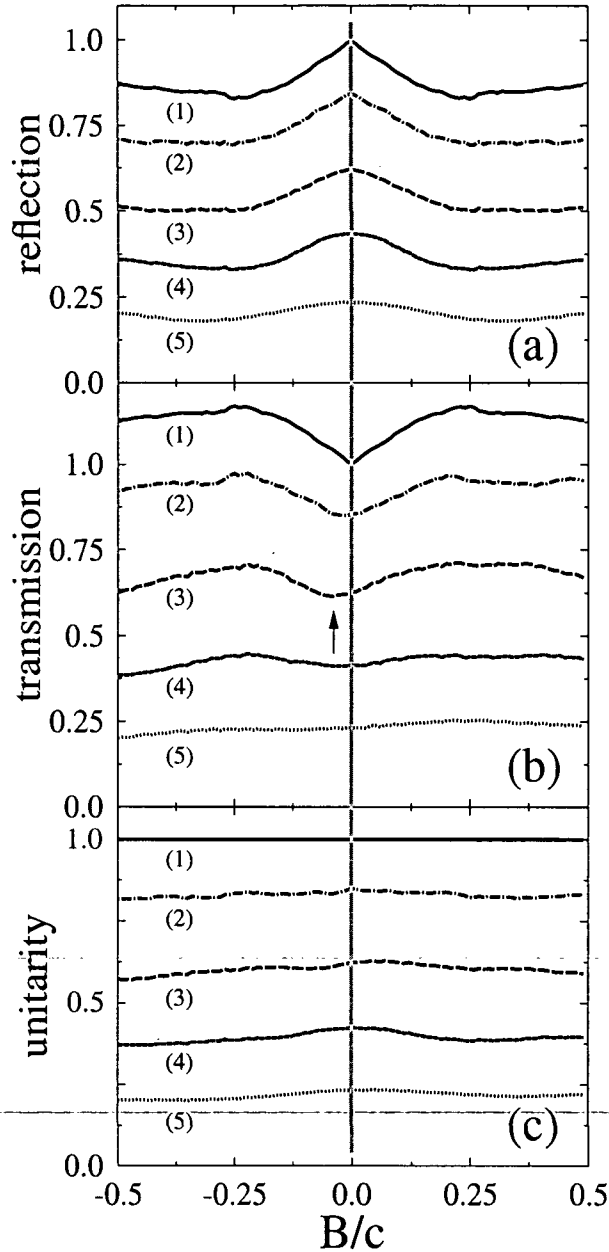


Figure 9.1: Weak localization peaks in the average of (a) total reflection $\langle R^{\text{tot}}(B) \rangle$ and (b) total transmission probability $\langle T^{\text{tot}}(B) \rangle$ as a function of the magnetic field B . To test the unitarity of the procedure we show in (c) the sum of the corresponding curves from (a) and (b). The gray vertical line marks the field free case ($B = 0$). In each of the three figure parts, the curves from top to bottom stand for the data (1) without any length cut off ($L_{\text{max}} = \infty$), (2) $L_{\text{max}} = 85$, (3) $L_{\text{max}} = 45$, (4) $L_{\text{max}} = 25$, and (5) $L_{\text{max}} = 15$. The average was taken over 600 equidistant values in the interval $k_F = [2.2, 2.8] \times \pi/d$. In (a) the triangular peak shape in the resistance becomes gradually visible for increasing L_{max} . In (b) the dip in the transmission lies off the center for a finite cut off length L_{max} (see indicated arrow). Note the B -dependent unitarity deficiency in (c).

trajectories are most strongly damped. In such a way a non-zero temperature can modify the steep triangular WL peak shape into a smoother and broader Lorentzian lineshape. Above a critical temperature, the WL peak is suppressed entirely.

To reproduce this transition to higher temperatures numerically, we introduce a cut off length L_{\max} into our averaging procedure for the WL curves. So far we calculated the $t_{mn}(k_F)$ and the $r_{mn}(k_F)$ at 600 equidistant points in a k_F -interval $k_F = [k_{\min}, k_{\max}]$ and took the average for the whole interval at a fixed magnetic field B . In the following, this data set will be subject to an additional transformation: Instead of evaluating its average value, we first perform a *Fast Fourier Transform (FFT)* [57] of the transport coefficients $t_{mn}(k_F)$,

$$\tilde{t}_{mn}(L) = \frac{1}{\sqrt{2\pi}} \int_{k_{\min}}^{k_{\max}} dk e^{-ikL} t_{mn}(k). \quad (9.1)$$

After that we set to zero all those values of $\tilde{t}_{mn}(L)$ for which $L > L_{\max}$ and obtain thereby the reduced Fourier transform $\tilde{t}_{mn}^{\max}(L)$. Transforming this quantity back to k -space,

$$t_{mn}^{\max}(k) = \frac{1}{\sqrt{2\pi}} \int_{k_{\min}}^{k_{\max}} dk e^{+ikL} \tilde{t}_{mn}^{\max}(L), \quad (9.2)$$

we get $t_{mn}^{\max}(k)$, which is a data set for the k -dependent transmission amplitudes, where all contributions from trajectories longer than $L = L_{\max}$ are filtered out. Taking the average value of this new data set at a fixed magnetic field B , allows us to study the dependence on the WL line shape on L_{\max} . For completeness we mention that the procedure for the reflection amplitudes $r_{mn}(k_F)$ is the same as shown here explicitly for the $t_{mn}(k_F)$.

The numerical results we obtained in this way are displayed by the dashed and dotted lines in Fig. 9.1. A transition from triangular to Lorentzian line shape is strikingly evident for decreasing L_{\max} . In Fig. 9.2 the two curves for total reflection with $L_{\max} = \infty$ and $L_{\max} = 25$ are directly compared with each other. Note also that the WL dip in the average of the total transmission shifts away from $B = 0$ (see the arrow in Fig. 9.1b). Since the WL peak in the total reflection keeps its maximum at $B = 0$, we have direct evidence for a B -dependent unitarity deficiency (see Fig. 9.1c). The total shift by which the WL peaks are vertically displaced in dependence of L_{\max} , originates in the values of $\tilde{t}_{mn}(L)$ which are set to zero in our procedure. Since their contribution is suppressed, also the average value of the back-transformed quantity $t_{mn}^{\max}(k)$ is lowered.

In the experiment [38] the lithographic dimension of the diameter of the circular dot is $1.08\mu m$. The coherence length at a temperature below $400mK$ is estimated to exceed $15\mu m$. With these estimates the electron can go about $15/1.08 \approx 14$ times back and forth in the circular dot before losing its coherence. We take this value as an order-of-magnitude estimate for the amount of phase coherence required to observe the triangular WL peak shape. In our calculations the circle diameter is $2 \times \sqrt{(4 + \pi)/\pi} \approx 3$. Considering Fig. 9.1a,b we note that the critical cut off length, where the WL peak shape changes from triangular to Lorentzian shape, lies approximately between 45 and 85, i.e. at about $L_{\max} \approx 60$. The number of bounces

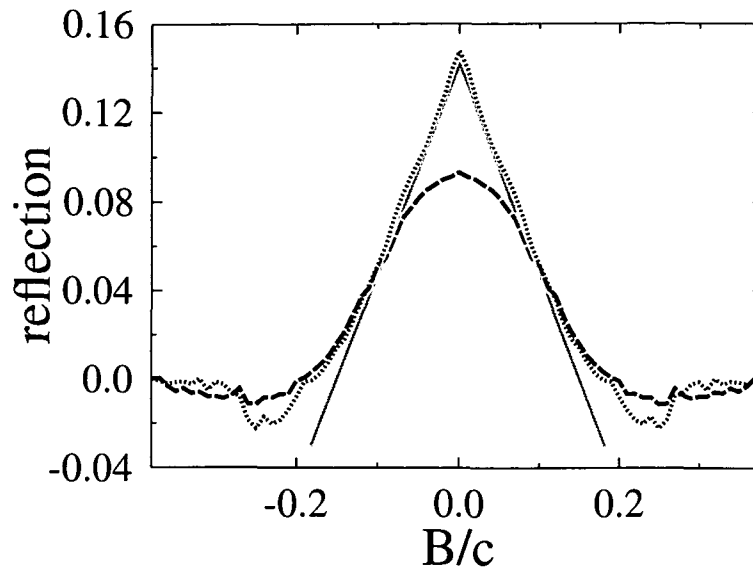


Figure 9.2: Weak localization peak in the total reflection probability of the circular dot with 90° lead orientation. The dotted curve contains no cut off length ($L_{\max} = \infty$) and reproduces the predicted linear decrease around $B = 0$ (see straight gray lines). The dashed curve was evaluated with a cut off at $L_{\max} = 25$ and shows a Lorentzian profile. The curves are the same as in Fig. 9.1, but are shifted to zero at $B/c = \pm 0.38$ for better comparison.

across the cavity in this regime is therefore approximately $60/3 \approx 20$. This estimate agrees quite well with the 14 bounces that were found in the experiment.

9.2 Future work

As the WL effect is often explained by the interference of trajectories with their time-reversed partner, one might think that the phenomenon of WL is well understood semiclassically. However, attempts to perform *ab initio* numerical simulations using standard semiclassical approaches failed to be in quantitative agreement with the quantum mechanical simulations [137, 138]. Within the framework of semiclassical approximations this long-standing problem was often addressed by the so-called *diagonal approximation*. This concept is based on the consideration that only pairs of paths, which are built up from orbits with identical incident and exit angle, contribute to the WL peak. However also other paths which are not included in this approximation play a non-negligible role (see e.g. [140]). Even when going beyond the diagonal approximation by numerically shooting a large number of different semiclassical trajectories, the strong unitarity deficiency of the standard semiclassical approximations hinders these theories to quantitatively account for the correct WL peaks [77, 141]. Recently, modifications to the standard semiclassical approaches have been proposed for which the fulfillment of the unitarity requirement is signif-

icantly improved [67, 74, 141, 142]. The challenge for these improved semiclassical approximations will be to represent the WL peaks accurately. Work along these lines is in progress.

Chapter 10

Summary

A new technique for calculating ballistic magnetotransport through open quantum dots was presented. The *Modular Recursive Green's Function Method* (MRGM) is an extension of the widely used standard recursive Green's function technique and is based on the decomposition of nonseparable scattering geometries into separable substructures (modules). Thereby an unprecedented energy and magnetic field range can be explored with high accuracy. This was demonstrated by the calculation of transport coefficients and scattering wavefunctions in the two extreme cases of high magnetic fields and short wavelengths. For very small cyclotron radii we found strictly periodic oscillations in the transmission spectrum and beating phenomena above well defined threshold values (as a function of B and k_F). These features were explained by the presence of edge states, travelling along the boundary of the cavity. For these states scattering only takes place at the lead junctions, whose sharp edges play a crucial role for the dynamics of the system. For a detailed analysis a multi-channel interference model was employed. This model allows to classify the observed transmission fluctuations within the framework of Fano resonances. Several surprising phenomena could thereby be explained. It is shown why transport through the circular dot is independent of the lead orientation above a well defined threshold value, given that the lead mouths are equal and separated from each other. Periodic transmission fluctuations are also observed for very high energies, where localization of the scattering wave functions along classical orbits takes place. Moreover, the MRGM has been applied to simulate basic phenomena in the field of ballistic transport theory. One of these are Fano resonances, a phenomenon which we discussed by comparing numerical data with the measured results of a microwave experiment. The design of the measurement was conceived such that Fano resonances arise in the transmission of microwaves through a metal cavity. We analyzed the resulting resonances and could thereby study the interplay between resonant and non-resonant transport in unprecedented detail. By controlled change of the cavity opening, tuning a Fano resonance from the Breit-Wigner limit to the window resonance limit has become possible. As was shown, Fano resonances can be used to accurately determine the degree of decoherence present in the scattering device. Non-monotonic behavior of resonance parameters can be related to avoided crossings between interacting resonances which can be unambiguously associated

with different resonant modes of the cavity.

We also employed the MRGM to simulate the integer quantum Hall effect. Calculations for the Hall voltage were performed by deriving its values from the scattering wave functions in the high magnetic field regime. The Hall voltage shows plateau values with steps at those magnetic field strengths, where a Landau level crosses the Fermi energy E_F of the scattering electron. By inclusion of a disorder potential we observe antiresonances superimposed on the quantum Hall plateaus, which originate from the eigenstates "living" in the disordered region. Most interestingly, the position of the steps and the values of the plateaus are not changed by the inclusion of the disorder potential provided that it is not too strong.

The de Haas-van Alphen (dHvA) effect was briefly discussed in this thesis. The magnetic field dependence of the energy eigenstates in a closed circular quantum dot gives rise to characteristic oscillations in the magnetization of this module. Among these we identify dHvA oscillations and Aharonov-Bohm oscillations, related to the flux enclosed by the edge states in the circle.

Another topic addressed in this thesis is the effect of "shot noise". We performed extensive calculations on transport through the rectangular, circular and stadium shaped billiards. One very surprising result we found is that the suppression of shot noise is only very slightly different for those quantum dots with underlying regular and chaotic classical dynamics respectively. We find results on the quantum-to-classical crossover of shot noise which are in very close agreement with recent experiments. To our knowledge, our simulation constitutes the first numerical realization of this crossover in transport through quantum dots.

Finally, an analysis of the weak localization (WL) effect in transport through the circular billiard was presented. By the numerical evaluation of a very large sample of data, we confirm the prediction of a triangular WL peak line shape in transport through the circle. By filtering out the long electron trajectories in the Fourier transform of the k -dependent transport coefficients, we demonstrate how this triangular shape is changed into a Lorentzian WL peak line shape. In such a way we can simulate effects of decoherence and their influence on the WL peak in the experiment.

Chapter 11

Outlook

In this last chapter we present possible future applications of the MRGM and discuss results which we expect to be attainable by our method. Work in two specific areas is presently in progress [63, 143] and some preliminary findings shall be summarized in the following.

In one of these two topics we are concerned with ballistic transport through quantum billiards with a mixed classical phase space. Since such billiards constitute the generic case of a dynamical system (as opposed to the fully regular or fully chaotic case), it is very interesting to study the quantum signatures of their mixed phase space. A convenient way to realize such systems is to choose the potential profiles of the billiard walls smooth¹ rather than discontinuous (see Fig. 11.1a). Only very recently it was shown [144] that the hierarchical phase space of these mixed systems gives rise to isolated resonances in the transport coefficients. These resonances arise from the coupling of the lead states to those cavity states which live behind partial transport barriers (“cantori”) and which can therefore only be accessed by tunneling through the barriers. For this reason the resonances in transmission are very sharp and occur very near to those energies where these eigenstates live. In Fig. 11.1c we show the scattering wavefunction which couples to such a state behind a partial transport barrier. Note the clearly visible localization around the corresponding classical periodic orbit. What happens classically, is that an incoming trajectory is “trapped” for very long times in the hierarchical phase space in the vicinity of the periodic orbit (see Fig. 11.1b). Accordingly, the calculations employing the MRGM for the scattering device shown in Fig. 11.1a clearly confirm the presence of the isolated transmission resonances in the high-energy regime [63]. Work on the evaluation of the resonance line shapes according to the Fano resonance parametrization Eq. (5.4) is in progress.

The phenomenon of trapped trajectories in a mixed phase space inspired the prediction of “fractal conductance fluctuations” [145], on which field considerable attention was focussed recently [146–149]. Although it was claimed that these fractal fluctuations were observed in transport experiments [147–149], present numerical techniques appear not to be efficient enough to reproduce this phenomenon [146].

¹As long as these smooth walls do not destroy the separability in a module, the MRGM is capable of incorporating such features.

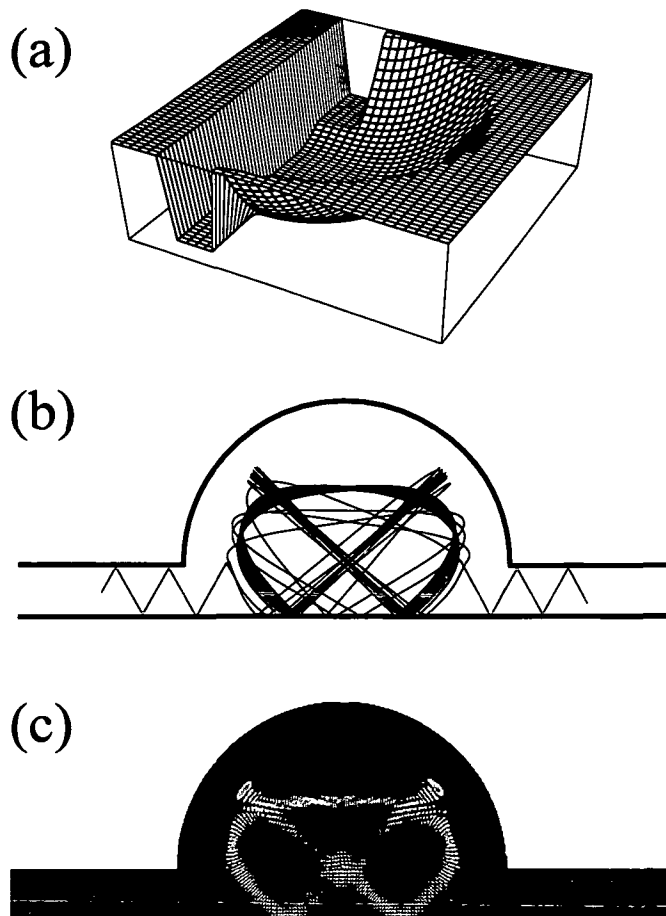


Figure 11.1: (a) Potential landscape for the softwall billiard which gives rise to a mixed classical phase space. As shown in (b), classical trajectories in this potential landscape can get trapped in the vicinity of periodic orbits. Solving the quantum transport problem for this geometry, we find a pronounced enhancement around such classical orbits. In (c) the MRGM-result for the absolute square of such a particular scattering wavefunction $|\psi(x, y)|^2$ is shown.

Although the MRGM reaches beyond techniques previously employed, it seems that fractal fluctuations are, if at all existent, beyond the energy which can currently be attained by the MRGM. This results again implies the intriguing question whether the measured fractality is indeed a signature of mixed classical dynamics or rather of some noise-like mechanism.

The second topic to which the MRGM is about to be applied, is the electron dynamics in billiards with a boundary that contains normal-conducting (N) and superconducting (S) walls. Such systems are referred to as “Andreev billiards” since the low-energy density of states $\rho(\varepsilon)$ with ε inside the gap Δ of the superconductor, $\varepsilon < \Delta$, is profoundly affected by retroreflections first analyzed by Andreev [150]. An electronic quasi-particle excitation with energy $\varepsilon = E - E_F$ just above the Fermi energy E_F approaching the $S - N$ interface is reflected as a hole with energy $-\varepsilon$

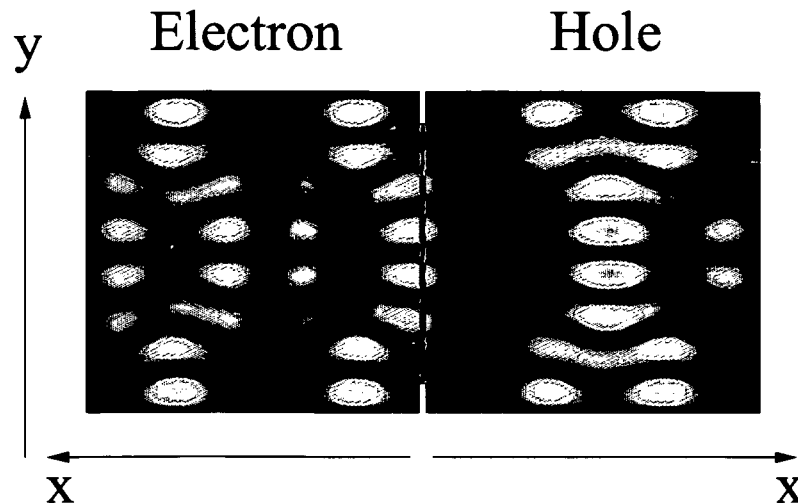


Figure 11.2: *Electron and hole density $|\psi(x,y)|^2$ in the N-region of a rectangular Andreev billiard at zero magnetic field B . The calculations were performed for an excitation gap $\Delta = 0.02 \times E_F$, an excitation energy $\varepsilon = 0.6478 \times \Delta$ and identical effective masses for the electron and the hole, both in the N- and the S-region. We display the electron density on the left and the hole density as a mirror image on the right half of the picture. The red strip in the center marks the position of the superconductor.*

and approximately the same momentum but opposite velocity. The trajectory thus retraces itself rather than being specularly reflected. Only in the limit $\varepsilon \rightarrow 0$ becomes the retroreflection exact. One consequence of retroreflections is the existence of a class of periodic orbits absent in N -quantum dots: any classical trajectory visiting the $S - N$ interface twice becomes periodic. As periodic orbits constitute the “skeleton” of semiclassical quantization [10], significant changes in the spectral properties of quantum dots are to be expected. The ensuing classical, semiclassical and quantum dynamics of Andreev billiards has become the topic of intense research [151–154]. Remarkably, there have been up to now only few fully quantum mechanical simulations of Andreev billiards. The present status of research in this field is succinctly summarized in a recent paper by Silvestrov *et al.* (March 2003) [154] “one important challenge for future research is the test of the adiabatic quantization of Andreev billiards numerically by solving the Bogolubov-De Gennes equation [for a chaotic billiard] on a computer”. By applying the MRGM to the solution of this problem considerable progress in this direction should become possible. In Fig. 11.2 we present a first example of an electron-hole wavefunction in a rectangular Andreev billiard at zero magnetic field and in the limiting case that the penetration depth into the S -junction is small compared to the wavelength λ of the quasi-particle [143]. The differences between the wavefunction for electrons and holes may be taken as an indication for contributions of non-retracing electron-hole trajectories.

A subject, on which we want focus closer attention in the near future, is the shot-noise suppression in billiards with regular, chaotic and mixed classical dynamics, respectively (see section 8.5). Also a quantitatively compatible simulation of the

WL peaks with the improved semiclassical techniques presented in Ref. [74] shall be further pursued. Other envisioned applications of the MRGM include the investigation of quantum Hamiltonian ratchets [155] and of the Hofstadter butterfly [8, 11, 56].

Bibliography

- [1] C. M. Marcus, A. J. Rimberg, R. M. Westervelt, P. F. Hopkins, and A. C. Gossard, *Phys. Rev. Lett.* **69**, 506 (1992).
- [2] C. M. Marcus, A. J. Rimberg, R. M. Westervelt, P. F. Hopkins, and A. C. Gossard, *Surf. Sci.* **305**, 480 (1994).
- [3] M. W. Keller, O. Millo, A. Mittal, D. E. Prober, and R. N. Sacks, *Surf. Sci.* **305**, 501 (1994).
- [4] D. Ferry, H. Grubin, C. Jacobini, and A.-P. Jauho, eds., *Quantum Transport in Ultrasmall Devices*, vol. 342 (NATO ASI Series B, New York, 1995).
- [5] M. A. Reed and W. P. Kirk, eds., *Nanostructure Physics and Fabrication* (Academic, New York, 1989).
- [6] E. Prange and S. M. Girvin, eds., *The Quantum Hall Effect* (Springer, New York, 1987).
- [7] N. W. Ashcroft and N. D. Mermin, *Solid State Physics* (Saunders College Publishing, 1976).
- [8] D. R. Hofstadter, *Phys. Rev. B* **14**, 2239 (1976).
- [9] Y. Aharonov and D. Bohm, *Phys. Rev.* **115**, 485 (1959).
- [10] M. C. Gutzwiller, *Chaos in Classical and Quantum Mechanics* (Springer, New York, 1991).
- [11] H. J. Stöckmann, *Quantum Chaos* (Cambridge University Press, 1999).
- [12] E. J. Heller, *Phys. Rev. Lett.* **53**, 1515 (1984).
- [13] X. Yang, H. Ishio, and J. Burgdörfer, *Phys. Rev. B* **52**, 8219 (1995).
- [14] A. MacKinnon and B. Kramer, *Z. Phys. B* **52**, 1 (1983).
- [15] A. MacKinnon, *Z. Phys. B* **59**, 385 (1985).
- [16] L. Schweitzer, B. Kramer, and A. MacKinnon, *Z. Phys. B* **59**, 379 (1985).
- [17] F. Sols, M. Macucci, U. Ravaioli, and K. Hess, *J. Appl. Phys.* **66**, 1892 (1989).

- [18] D. K. Ferry and S. M. Goodnick, *Transport in Nanostructures* (Cambridge University Press, 1997).
- [19] F. P. Simonotti, E. Vergini, and M. Saraceno, *Phys. Rev. E* **56**, 3859 (1997).
- [20] W. E. Bies, L. Kaplan, M. R. Haggerty, and E. J. Heller, *Phys. Rev. E* **63**, 066214 (2001).
- [21] R. Akis, D. K. Ferry, and J. P. Bird, *Phys. Rev. Lett.* **79**, 123 (1997).
- [22] I. V. Zozoulenko, F. A. Maaø, and E. H. Hauge, *Phys. Rev. B* **53**, 7975 (1996).
- [23] D. Mamaluy, M. Sabathil, and P. Vogl, *J. Appl. Phys.* **93**, 4628 (2003).
- [24] C. S. Lent, *Phys. Rev. B* **43**, 4179 (1991).
- [25] Z.-L. Ji and K.-F. Berggren, *Phys. Rev. B* **52**, 1745 (1995).
- [26] L. Christenson, H. Linke, P. Omling, P. Lindelof, I. V. Zozoulenko, and K.-F. Berggren, *Phys. Rev. B* **57**, 12306 (1998).
- [27] K. Hornberger and U. Smilansky, *Phys. Rev. Lett.* **88**, 024101 (2002).
- [28] K. Hornberger and U. Smilansky, *Phys. Rep.* **367**, 249 (2002).
- [29] T. Ueta, *J. Phys. Soc. Jpn.* **61**, 4314 (1992).
- [30] K. Nakamura and H. Ishio, *J. Phys. Soc. Jpn.* **61**, 3939 (1992).
- [31] K. Nakamura, K. Ita, and Y. Takane, *Phys. A* **27**, 5889 (1994).
- [32] Y. Wang, J. Wang, and H. Guo, *Phys. Rev. B* **49**, 1928 (1994).
- [33] R. G. Nazmitdinov, K. N. Pichugin, I. Rotter, and P. Šeba, *Phys. Rev. B* **66**, 85322 (2002).
- [34] U. Fano, *Phys. Rev.* **124**, 1866 (1961).
- [35] K. v. Klitzing, G. Dorda, and M. Pepper, *Phys. Rev. Lett.* **45**, 494 (1980).
- [36] C. Kittel, *Introduction to solid state physics* (J. Wiley & Sons, 1996), 7th ed.
- [37] Y. M. Blanter and M. Büttiker, *Phys. Rep.* **336**, 1 (2000).
- [38] A. M. Chang, H. U. Baranger, L. N. Pfeiffer, and K. W. West, *Phys. Rev. Lett.* **73**, 2111 (1994).
- [39] D.-H. Kim, H.-S. Sim, and K. Chang, *Phys. Rev. B* **64**, 115409 (2001).
- [40] D.-H. Kim, H.-S. Sim, and K. Chang, *Phys. Rev. B* **67**, 129903(E) (2003).
- [41] S. Rotter, F. Libisch, J. Burgdörfer, U. Kuhl, and H.-J. Stöckmann, *cond-mat/0312328* (2003).

- [42] M. Büttiker, Phys. Rev. B **38**, 9375 (1988).
- [43] C. W. J. Beenakker, private communication (2003).
- [44] H.-S. Sim and H. Schomerus, Phys. Rev. Lett. **89**, 66801 (2002).
- [45] S. Oberholzer, E. V. Sukhorukov, and C. Schönberger, Nature **415**, 765 (2002).
- [46] J. Tworzydło, A. Tajic, H. Schomerus, and C. W. J. Beenakker, Phys. Rev. B **68**, 115313 (2003).
- [47] F. M. Peeters, Phys. Rev. Lett. **61**, 589 (1988).
- [48] R. L. Schult, H. W. Wyld, and R. G. Ravenhall, Phys. Rev. B **41**, 12760 (1990).
- [49] E. N. Economou, *Green's Functions in Quantum Physics* (Springer, Berlin, 1979).
- [50] S. Rotter, Diploma thesis, Institute for Theoretical Physics, TU-Vienna (1999).
- [51] R. Landauer, IBM J. Res. Dev. **1**, 223 (1957).
- [52] J. V. José and E. J. Saletan, *Classical Dynamics* (Cambridge University Press, 1998).
- [53] S. E. Koonin and D. C. Meredith, *Computational Physics* (Addison Wesley, Massachusetts, 1990).
- [54] R. E. Peierls, Z. Phys. **80**, 763 (1933).
- [55] S. Rotter, J.-Z. Tang, L. Wirtz, J. Trost, and J. Burgdörfer, Phys. Rev. B **62**, 1950 (2000).
- [56] J. Skjånes, E. H. Hauge, and G. Schön, Phys. Rev. B **50**, 8636 (1994).
- [57] W. H. Press, S. A. Teukolsky, W. T. Vetterling, and B. P. Flannery, *Numerical Recipes in Fortran 77* (Cambridge University Press, 1986).
- [58] T. Ando, Phys. Rev. B **44**, 8017 (1991).
- [59] N. J. Higham and H.-M. Kim, IMA Journal of Numerical Analysis **20**, 499 (2000).
- [60] H. U. Baranger and A. D. Stone, Phys. Rev. B **40**, 8169 (1989).
- [61] H. U. Baranger, D. P. DiVincenzo, R. A. Jalabert, and A. D. Stone, Phys. Rev. B **44**, 10637 (1991).
- [62] H. Ishio and J. Burgdörfer, Phys. Rev. B **51**, 2013 (1995).

- [63] B. Weingartner, Diploma thesis (to be published), Institute for Theoretical Physics, TU-Vienna (2004).
- [64] B. Weingartner, Project report, Institute for Theoretical Physics, TU-Vienna (2003).
- [65] I. V. Zozoulenko and T. Lundberg, *Phys. Rev. Lett.* **81**, 1744 (1998).
- [66] R. Akis, D. K. Ferry, and J. P. Bird, *Phys. Rev. Lett.* **81**, 1745 (1998).
- [67] L. Wirtz, J.-Z. Tang, and J. Burgdörfer, *Phys. Rev. B* **56**, 7589 (1996).
- [68] Z.-L. Ji and K.-F. Berggren, *Phys. Rev. B* **52**, 1745 (1995).
- [69] M. Büttiker, in *Semiconductors and Semimetals*, edited by M. Reed (Academic Press, San Diego, 1992), vol. 35, p. 191.
- [70] J. H. Davies, *The Physics of Low-Dimensional Semiconductors* (Cambridge University Press, 1998).
- [71] S. Datta, *Electronic Transport in Mesoscopic Systems* (Cambridge University Press, 1995).
- [72] L. I. Glazman and M. Jonson, *Phys. Rev. B* **41**, 10686 (1990).
- [73] D.-H. Kim and K. Chang, *Phys. Rev. B* **66**, 155402 (2002).
- [74] L. Wirtz, C. Stampfer, S. Rotter, and J. Burgdörfer, *Phys. Rev. E* **67**, 16206 (2003).
- [75] U. Sivan, Y. Imry, and C. Hartzstein, *Phys. Rev. B* **39**, 1242 (1989).
- [76] B. J. van Wees, L. P. Kouwenhoven, C. J. P. M. Harmans, J. G. Williamson, C. E. Timmering, M. E. I. Broekaart, C. T. Foxon, and J. J. Harris, *Phys. Rev. Lett.* **62**, 2523 (1989).
- [77] L. Wirtz, J.-Z. Tang, and J. Burgdörfer, *Phys. Rev. B* **59**, 2956 (1999).
- [78] J. U. Nöckel and A. D. Stone, *Phys. Rev. B* **50**, 17415 (1994).
- [79] R. A. Webb, S. Washburn, C. P. Umbach, and R. B. Laibowitz, *Phys. Rev. Lett.* **54**, 2696 (1985).
- [80] S. Pedersen, A. E. Hansen, A. Kristensen, C. B. Sørensen, and P. E. Lindelof, *Phys. Rev. B* **61**, 5457 (2000).
- [81] K. N. Pichugin and A. F. Sadreev, *Phys. Rev. B* **56**, 9662 (1997).
- [82] T. Blomquist, H. Schanze, I. V. Zozoulenko, and H.-J. Stöckmann, *Phys. Rev. E* **66**, 026217 (2002).
- [83] H. Beutler, *Z. Phys.* **93**, 177 (1935).

- [84] U. Fano, *Nuovo Cimento* **12**, 156 (1935).
- [85] R. Adair, C. Bockelman, and R. E. Peterson, *Phys. Rev.* **76**, 308 (1949).
- [86] J. Simpson and U. Fano, *Phys. Rev. Lett.* **11**, 158 (1963).
- [87] F. Cerdeira, T. Fjeldly, and M. Carpona, *Phys. Rev. B* **8**, 4734 (1973).
- [88] J. Feist, F. Capasso, C. Sirtori, K. West, and L. Pfeiffer, *Nature* **390**, 589 (1997).
- [89] V. Madhavan, W. Chen, T. Jamneala, M. Crommie, and S. Wingreen, *Science* **280**, 567 (1998).
- [90] J. Göres, D. Goldhaber-Gordon, S. Heemeyer, M. A. Kastner, H. Shtrikman, D. Mahalu, and U. Meirav, *Phys. Rev. B* **62**, 2188 (2000).
- [91] S. Rotter, B. Weingartner, N. Rohringer, and J. Burgdörfer, *Phys. Rev. B* **68**, 165302 (2003).
- [92] K. Kobayashi, H. Aikawa, S. Katsumoto, and Y. Iye, *Phys. Rev. Lett.* **88**, 256806 (2002).
- [93] A. A. Clerk, X. Waintal, and P. W. Brouwer, *Phys. Rev. Lett.* **86**, 4636 (2001).
- [94] W. Heiss and A. Sannino, *Phys. Rev. A* **43**, 4159 (1991).
- [95] J. Burgdörfer, X. Yang, and J. Müller, *Chaos, Solitons and Fractals* **5**, 1235 (1995).
- [96] J. Okołowicz, M. Płoszajczak, and I. Rotter, *Phys. Rep.* **374**, 271 (2003).
- [97] E. Persson, I. Rotter, H.-J. Stöckmann, and M. Barth, *Phys. Rev. Lett.* **85**, 2478 (2000).
- [98] U. Eichmann, T. F. Gallagher, and R. Konik, *Phys. Rev. Lett.* **90**, 233004 (2003).
- [99] H. Friedrich, *Theoretical Atomic Physics* (Springer, Berlin, 1998).
- [100] A. Richter, in *IMA Vols. in Mathematics and its Applications*, edited by D. A. Hejhal, J. Friedman, M. C. Gutzwiller, and A. M. Odlyzko (Springer, New York, 1999), vol. 109, p. 479.
- [101] F. Libisch, Project report, Institute for Theoretical Physics, TU-Vienna (2003).
- [102] J. von Neumann and E. Wigner, *Phys. Z.* **30**, 467 (1989).
- [103] W. Porod, Z. Shao, and C. S. Lent, *Phys. Rev. B* **48**, R8495 (1993).
- [104] Z. Shao, W. Porod, and C. S. Lent, *Phys. Rev. B* **49**, 7453 (1994).

- [105] O. Entin-Wohlman, C. Hartzstein, and Y. Imry, *Phys. Rev. B* **34**, 921 (1986).
- [106] T. Koschny, H. Potempa, and L. Schweitzer, *Phys. Rev. Lett.* **86**, 3863 (2001).
- [107] Y. Takagaki and D. K. Ferry, *Phys. Rev. B* **47**, 9913 (1993).
- [108] Y. Takagaki and K. Ploog, *Phys. Rev. B* **51**, 7017 (1995).
- [109] Y. Meir, O. Entin-Wohlman, and Y. Gefen, *Phys. Rev. B* **42**, 8351 (1990).
- [110] E. N. Bogachek and U. Landman, *Phys. Rev. B* **52**, 14067 (1995).
- [111] W.-C. Tan and J. C. Inkson, *Phys. Rev. B* **60**, 5626 (1999).
- [112] U. Sivan and Y. Imry, *Phys. Rev. Lett.* **61**, 1001 (1988).
- [113] W. Schottky, *Ann. Phys. (Leipzig)* **57**, 541 (1918).
- [114] C. L. Kane and M. P. A. Fisher, *Phys. Rev. Lett.* **72**, 724 (1994).
- [115] R. B. Laughlin, *Phys. Rev. Lett.* **50**, 1395 (1983).
- [116] O. Agam, I. Aleiner, and A. Larkin, *Phys. Rev. Lett.* **85**, 3153 (2000).
- [117] S. Oberholzer, E. V. Sukhorukov, C. Strunk, C. Schönenberger, T. Heinzel, and M. Holland, *Phys. Rev. Lett.* **86**, 2114 (2001).
- [118] R. G. Nazmitdinov, H.-S. Sim, H. Schomerus, and I. Rotter, *Phys. Rev. B* **66**, 241302(R) (2002).
-
- [119] C. Beenakker and C. Schönenberger, *Physics Today* **56(5)**, 37 (2003).
- [120] V. A. Khlus, *Sov. Phys. JETP* **66**, 1243 (1987).
-
- [121] G. B. Lesovik, *Sov. Phys. JETP* **49**, 592 (1989).
- [122] M. Büttiker, *Phys. Rev. Lett.* **65**, 2901 (1990).
- [123] U. Fano, *Phys. Rev.* **72**, 26 (1947).
- [124] F. Aigner, Project report, Institute for Theoretical Physics, TU-Vienna (2003).
- [125] W. A. Lin, J. B. Delos, and R. V. Jensen, *Chaos* **3**, 655 (1993).
- [126] R. V. Jensen, *Chaos* **1**, 101 (1991).
- [127] G. Benettin and J.-M. Strelcyn, *Phys. Rev. A* **17**, 773 (1978).
- [128] S. Rotter, Project report, Institute for Theoretical Physics, TU-Vienna (1998).
- [129] G. Casati, G. Maspero, and D. L. Shepelyansky, *Phys. Rev. E* **56**, R6233 (1997).

- [130] I. V. Zozoulenko and T. Blomquist, *Phys. Rev. B* **67**, 85320 (2003).
- [131] P. W. Anderson, *Phys. Rev.* **109**, 1492 (1958).
- [132] M. Brack and R. K. Bhaduri, *Semiclassical Physics* (Addison-Wesley, 1997), 1st ed.
- [133] N. Giordano, *Phys. Rev. B* **22**, 5635 (1980).
- [134] M. B. Hastings, A. D. Stone, and H. U. Baranger, *Phys. Rev. B* **50**, 8230 (1994).
- [135] H. U. Baranger, R. A. Jalabert, and A. D. Stone, *Phys. Rev. Lett.* **70**, 3876 (1993).
- [136] K. Richter and M. Sieber, *Phys. Rev. Lett.* **89**, 206801 (2002).
- [137] R. A. Jalabert, H. U. Baranger, and A. D. Stone, *Phys. Rev. Lett.* **65**, 2442 (1990).
- [138] H. U. Baranger, R. A. Jalabert, and A. D. Stone, *Chaos* **3**, 665 (1993).
- [139] I. V. Zozoulenko and K.-F. Berggren, *Phys. Rev. B* **54**, 5823 (1996).
- [140] N. Argaman, *Phys. Rev. Lett.* **75**, 2750 (1995).
- [141] C. Stampfer, Diploma thesis, Institute for Theoretical Physics, TU-Vienna (2002).
- [142] C. Stampfer, L. Wirtz, S. Rotter, and J. Burgdörfer (2003), to be published.
- [143] F. Libisch, Diploma thesis (to be published), Institute for Theoretical Physics, TU-Vienna (2004).
- [144] A. Bäcker, A. Manze, B. Huckestein, and R. Ketzmerick, *Phys. Rev. E* **66**, 016211 (2002).
- [145] R. Ketzmerick, *Phys. Rev. B* **54**, 10841 (1996).
- [146] Y. Takagaki and K. H. Ploog, *Phys. Rev. B* **61**, 4457 (2000).
- [147] A. S. Sachrajda, R. Ketzmerick, C. Gould, Y. Feng, P. J. Kelly, A. Delage, and Z. Wasilewski, *Phys. Rev. Lett.* **80**, 1948 (1998).
- [148] A. P. Micolich, R. P. Taylor, A. G. Davies, J. P. Bird, R. Newbury, T. M. Fromhold, A. Ehlert, H. Linke, L. D. Macks, W. R. Tribe, et al., *Phys. Rev. Lett.* **87**, 36802 (2001).
- [149] R. Crook, C. G. Smith, A. C. Graham, I. Farrer, H. E. Beere, and D. A. Ritchie, *Phys. Rev. Lett.* **91**, 246803 (2003).
- [150] A. F. Andreev, *JETP Lett.* **19**, 1228 (1964).

- [151] J. Cserti, G. Vattay, J. Koltai, F. Taddei, and C. J. Lambert, Phys. Rev. Lett. **85**, 3704 (2000).
- [152] A. Kormányos, Z. Kaufmann, J. Cserti, and C. J. Lambert, Phys. Rev. B **67**, 172506 (2003).
- [153] J. Cserti, A. Kormányos, Z. Kaufmann, J. Koltai, and C. J. Lambert, Phys. Rev. Lett. **89**, 057001 (2002).
- [154] P. G. Silvestrov, M. C. Goorden, and C. W. J. Beenakker, Phys. Rev. Lett. **90**, 116801 (2003).
- [155] H. Schanz, M.-F. Otto, R. Ketzmerick, and T. Dittrich, Phys. Rev. Lett. **87**, 070601 (2001).

Acknowledgements

This work would not have seen the light of day without the help and support of many friends, my family, colleagues, and teachers. It is a great pleasure to list some of these people here to acknowledge their succour during the time I spent working on this thesis.

My special gratitude goes to my advisor, Prof. Joachim Burgdörfer, who woke my curiosity for the subject of ballistic transport and very much supported my work on this matter. His willingness to discuss physics - or any other question of interest - was one of the keystones for a very enjoyable time in his research group at the TU in Vienna.

Some of its members I would like to mention explicitly: Ludger Wirtz, who introduced me to the life of a scientist (including the work during the weekends) and to the TU orchestra. To Shuhei Yoshida I am not only indebted for the pleasant time we spent together in one office (listening to music), but also for his computer support and a lot of fun on joint trips to workshops and conferences. I owe many thanks to Bernhard Weingartner, Christoph Stampfer, Florian Libisch and Florian Aigner who contributed enormously to many of the subjects discussed in this thesis. It was and still is a great pleasure to collaborate with them.

I am also very grateful to the experimentalists in Marburg who performed the measurements on the microwave cavity: Ulrich Kuhl and Prof. Stöckmann. To witness the realization of our scattering device was indeed a gorgeous experience for me. Many thanks also for the kind invitation to visit the laboratory.

I am, moreover, indebted to Prof. Cserti, Andor Kormányos, and Karoly Tökési for their kind hospitality during my stay in Hungary. Also many thanks to Prof. Cserti for reading the manuscript and for his willingness to serve as examiner at the defense of this thesis.

For stimulating discussions my gratitude is due to: Diego Arbo, Andreas Buchleitner, Kostas Dimitriou, Wilfried Gansterer, Lars Hufnagel, Prof. Kasperkovitz, Prof. Ketzmerick, D.-H. Kim, Cord Müller, Prof. Langer, Emil Persson, Nina Rohringer, Prof. Rotter, Holger Schanz, Johannes Trost, Andreas Slateff, and Prof. Sols.

I would also like to acknowledge the support of Prof. Kummer, the head of our institute, and of Prof. Skalicky, the principal of the TU.

Mrs. Mössmer, Mrs. Unden, and Christoph Lemell deserve due credit for keeping the administration and the computers at the institute running.

Last, but definitely not least, I want to thank my family and friends, Laetitia, the fine people from the orchestra, and all those to whom I apologize for not having been able to mention them.

Curriculum vitae

Name: Stefan Rotter
Born: 12th of August 1975 in Vienna, Austria
Nationality: Austrian
Marital status: single

Present employment address

Institute for Theoretical Physics
Vienna University of Technology (TU-Vienna)
Wiedner Hauptstr. 8-10/136
A-1040 Vienna, Austria
Tel.: 01-58801-13618 Fax: 01-58801-13699
Email: rotter@concord.itp.tuwien.ac.at
Internet: <http://dollywood.itp.tuwien.ac.at/~rotter/>

Education and working experience

1981-1985 Primary school in Yspertal, Lower Austria
1985-1993 Grammar school in Wieselburg, Lower Austria
June-1993 Final exam-(with-distinction)
1993 Internship in the computing center of Raiffeisenbank,
Vienna (two months)
1993-1999 Physics student at the TU-Vienna
1996-1997 Erasmus exchange student at the Swiss Federal Institute of
Technology, Lausanne, Switzerland (10 months)
1998 Scientific stay at the University of Tennessee (one month)
1998-1999 Master thesis "*A modular recursive Green's function method
for quantum transport*", advisor: Prof. J. Burgdörfer
June 1999 Master degree (Dipl.-Ing.) at the TU-Vienna (with distinction)
1999-2000 Alternative work (instead of the compulsory military service)
at the International Department of the *Anne Frank Foundation*,
Amsterdam, the Netherlands (14 months)
since 2000 Ph.D. student in the group of Prof. J. Burgdörfer

- since 2001 University assistant at the Institute for Theoretical Physics,
TU-Vienna
- since 2001 Head of the committee of the TU symphony orchestra

Fields of research

Ballistic quantum transport, quantum chaos, Fano resonances, shot noise, integer quantum Hall effect, semiclassical approximations, Andreev billiards, quantum dynamics in a mixed phase space.

Teaching

- 1995-1999 Teaching assistant in Physics at the TU-Vienna
- 1996-1997 Teaching assistant in Mathematics at the Swiss Federal Institute of Technology, Lausanne, Switzerland
- since 1999 Co-advisor of four project works and two master theses
- 2002 Lecturer in the exercise classes *Quantum Theory* at the TU

Scholarships and grants

- 1996-1997 *Erasmus scholarship* of the European Union (exchange program)
- 1995-1999 *Achievement scholarship* of the TU-Vienna (three times)
- 1999 *Support scholarship* of the TU-Vienna
- 2000-2004 Ph.D. grant within the special research program *Advanced Light Sources* (ADLIS) of the Austrian Science Fund (FWF)
- 2002 *TOP scholarship* of the province of Lower Austria
- 2003 Travel grant of the bilateral Austrian-Hungarian Foundation
- 2003 Travel grant of the British Council

Languages

- German mother language
- English fluent
- French good in writing, reading, speaking and listening comprehension
- Dutch good in writing, reading, speaking and listening comprehension
- Russian basic knowledge

Extracurricular interests

Music, art, literature, travelling, languages, wining & dining.

List of publications

- [1] *Modular recursive Green's function method for ballistic quantum transport*
S. Rotter, J.-Z. Tang, L. Wirtz, J. Trost, and J. Burgdörfer
Phys. Rev. B **62** 1950 (2000).
- [2] *Semiclassical theory for transmission through open billiards: Convergence towards quantum transport*
L. Wirtz, C. Stampfer, S. Rotter, and J. Burgdörfer
Phys. Rev. E **67**, 016206 (2003).
- [3] *Ballistic quantum transport at high energies and high magnetic fields*
S. Rotter, B. Weingartner, N. Rohringer, and J. Burgdörfer
Phys. Rev. B **68**, 165302 (2003).
- [4] *Tunable Fano resonances in transport through microwave billiards*
S. Rotter, F. Libisch, J. Burgdörfer, U. Kuhl, and H.-J. Stöckmann
(cond-mat/0312328, submitted to Phys. Rev. E).

Talks and posters

- Seminar talks at the Max-Planck-Institute Göttingen, University of Bayreuth, Philipps University Marburg, Eötvös University Budapest and TU-Vienna.
- Talks at workshops in the Physikzentrum Bad Honnef, University of Regensburg, University of Palma de Mallorca and Atomki Debrecen.
- Talks and posters at conferences in Hamburg, Bad Honnef, Graz and Vienna.